Modeling and Measurement of Intermolecular Interaction Forces between Cartilage ECM Macromolecules

by

Delphine Marguerite Denise Dean

Submitted to the Department of Electrical Engineering and Computer Science
in partial fulfillment of the requirements for the degree of

Doctor of Philosophy in Electrical Engineering and Computer Science

at the

MASSACHUSETTS INSTITUTE OF TECHNOLOGY

February 2005

© Massachusetts Institute of Technology 2005. All rights reserved.

MASSACHUSETTS INSTITUTE OF TECHNOLOGY
MAR 14 2005
LIBRARIES

Author .....
Department of Electrical Engineering and Computer Science
January 31, 2005

Certified by .....
Alan J. Grodzinsky
Professor of Electrical, Mechanical, and Biological Engineering
Thesis Supervisor

Certified by .....
Christine Ortiz
Associate Professor of Materials Science and Engineering
Thesis Supervisor

Accepted by .....
Arthur C. Smith
Chairman, Department Committee on Graduate Students

BARKER

Modeling and Measurement of Intermolecular Interaction Forces between Cartilage ECM Macromolecules

by

Delphine Marguerite Denise Dean

Submitted to the Department of Electrical Engineering and Computer Science
on January 31, 2005, in partial fulfillment of the
requirements for the degree of
Doctor of Philosophy in Electrical Engineering and Computer Science

Abstract

The mechanical properties of cartilage tissue depend largely on the macromolecules that make up its extracellular matrix (ECM). Aggrecan is the most abundant proteoglycan in articular cartilage. It is composed of a core protein with highly charged, densely packed glycosaminoglycan (GAG) side chains, which are responsible for $\sim$ 50% of the equilibrium compressive stiffness of the tissue. Using atomic force microscopy (AFM) and high resolution force spectroscopy (HRFS), it is now possible to directly measure nanoscale interactions between ECM macromolecules in physiologically relevant aqueous solution conditions. In order to interpret these data and compare them to macroscopic tissue measurements, a combination of experiments and theoretical modeling must be used.

In this thesis, a new molecular-scale continuum Poisson-Boltzmann (PB)-based model was developed to predict the intermolecular interactions between GAG macromolecules by taking into account nanoscale space varying electric potential and fields between neighboring GAGs. A rod-like charge density distribution describing the time averaged space occupied by a single GAG chain was formulated. The spacing and size of the rods greatly influenced the calculated force even when the total charge was kept constant. The theoretical simulations described HRFS experimental data of the normal interaction force between two surfaces chemically end-grafted with an array of GAGs ("brushes") more accurately than simpler models which approximate the GAG charge as a homogeneous volume or planar surface charge. Taken together, these results highlight the importance of nonuniform molecular-level charge distribution on the measured GAG interaction forces.

Normal interaction forces between aggrecan macromolecules were measured using contact mode AFM imaging and by HRFS. The aggrecan molecules were end-grafted to gold-coated substrates and probe tips to achieve brush-like layers at physiologically relevant densities. Both colloidal probe tips ($2.5\mu m$ radius) and sharper probe tips ($\sim 25 - 50nm$ radius) were used. The measured normal forces were predominantly repulsive and showed a strong ionic strength dependence reflecting the importance of repulsive electrostatic interactions. These aggrecan-aggrecan forces were much larger

than those previously measured between brushes composed only of a single layer of GAG chains isolated from aggrecan molecules. The measured aggrecan normal force interactions were then compared to the predictions of the PB charged rod model for GAG electrostatic interactions and to measurements of the equilibrium compressive modulus of intact cartilage tissue. At near physiological bath conditions (0.1M NaCl), the PB electrostatic model closely predicted the values of the measured force for nanomechanical strains < 0.4, using model parameter values that were all fixed to their known values from the literature. At higher strains, the measured normal forces were higher than those predicted by the model, qualitatively consistent with the likelihood that other nonelectrostatic interactions were becoming more important. A compressive stiffness was also calculated from the measured aggrecan-aggrecan nanomechanical force data, and was found to be $\sim 50\%$ of the modulus of native intact cartilage. This is consistent with previous reports suggesting that aggrecan-associated electrostatic interactions account for approximately half of the tissue modulus.

Thesis Supervisor: Alan J. Grodzinsky
Title: Professor of Electrical, Mechanical, and Biological Engineering

Thesis Supervisor: Christine Ortiz
Title: Associate Professor of Materials Science and Engineering

Acknowledgments

A lot of people have helped me throughout my Ph.D. career (if I forgot someone, I'm sorry!).

I would first like to thank my advisors Professors Alan Grodzinsky and Christine Ortiz. They have given me a lot of guidance and they both have showed me what it's like to be a good researcher. Christine introduced me to a field that I had very little experience in. She kept me motivated and always encouraged a lot collaborations. It's amazing the problems we can solve when you bring people from lots of different fields together! Al is a great advisor and I should know since he was first my undergrad academic advisor, then M.Eng. advisor and then my Ph.D. advisor. It's really his fault I got a Ph.D. at MIT so blame him! No but seriously, thanks for making me apply my senior year. I had a blast and I'm glad I stuck with it! I would also like to thank Prof. Dennis Freeman who was on my thesis committee and also who taught 6.021J, a class that is partially responsible for me picking to do a UROP in this field in the beginning and which years later was a joy to help teach.

I would like to thank all the members of the nanocartilage subgroup. Joonil Seog started it off with the GAG measurements and without him I don't know how far I would have gotten (theory without experiments is pretty uninteresting to people!). Laurel Ng helped me a bunch when I made the switch back from theory to doing experiments on aggrecan plus she is a great sparring partner and baker (can't beat that combination! :) Lin Han figured out the micro-contact printing technique and he and I spend way too many hours in the AFM room poking and scanning those silly aggrecan (and he also makes the best killer spicy chinese food I've ever had!). I hope Bobae and our new UROPs, Jaqueline and Laura, have as much fun as I did working on nanocartilage :)

I want to thank everyone in the Ortiz group who always made Monday group meetings fun. I would especially like to thank Jae, the group photographer, who brought me coffee to cheer me up. Monica who taught me a lot about polymers, Kuangshin who always cheered on everyone in lab (even during conference talks :), and Jen, my sophomore year roommate, who helped organize lab socials and with whom I had fun avoiding the sleazy APS guys. Thanks to everyone at the Grodzinsky lab. That's lots of people but you all really made my grad school experience great so here goes (sorry if I miss anyone!): Diana always cheered me up when I was stressed out. Shuodan carries on the brave tradition of course sixers in the lab cuz someone's got to. Mike, my next door neighbor, always answered all my dumb questions including the latest "hey Mike? How long are acknowledgements supposed to be?" ;)- Jon F. helped me get good grades in those last two classes and get my minor requirement done ("Computational Funtional Systems Biological Genomics") Moonsoo helped me sort out some of the numerics early during my Master's thesis which really helped later down the road! John K., my other neighbor, was in the lab just as long as me and he always made group meeting fun with his lovely horse pictures. Jenny actually helped me understand what people meant when they say they use RT-PCR. Parth could always be counted on to be there late at night and chat with me to keep me

awake. Bernd, who squishes ankles like noone else, makes one crazy drink! Jon S. knows more about sports than I ever will. Anna always asked me great questions in group meeting (look! I graduated! you can do it too :) Cameron makes really yummy mint ice cream and plays volleyball better than anyone else in lab (yea the California team!). Nora kicks some serious butt (or I guess that should be "pokes some serious butt with a sharp stick") was one of the reasons I joined the lab and she really helped me feel like I was part of group very early on. Eliot was always willing to listen to my crazy theory ideas, really helped me debunk some of the equations I was working on several times, and is the only other person around our lab that seems to agree with me that writing my thesis in LaTeX was a good idea (it didn't crash once!). Han-Hwa Hung was the best office mate I could ever ask for; she sure knows her way around lab better than anyone and the cookies were a great perk :) Linda Bragman sent me great funny emails to brighten my day, dealt with the course 6 office for me on multiple occasions, and helped me remember that there is life outside MIT. Thanks for keeping me sane :)

I'd like to thank a bunch of friends who always kept me busy outside of lab. All the people at the Taekwondo club always were very supportive. I want to especially thank Radhika, my belt buddy, who is my hero for getting that board break, Grace who made sure that I thought about what I would do once I was done with MIT, Andrew who drove me home when it was late, and Conor who calmed me down when I got nervous way too many times, entertained me in lab with cool puzzles, and made me cookies when things got tough. The skating club always kept my early mornings busy. Diana dragged me to competitions and it was fun! Adriana took up the president job when I decided I should graduate. Zia was always cheerful and suprised me by coming to my thesis defense. Barb and Derek always helped me wake up way early in the morning, they listened to my whining, they came to my thesis defense, they kept me company when Brian was away, and they fed me! What more can you ask for :) Thanks to the old clams for always keeping me entertained with the "usual" MIT-type nerdiness ;)- Jacob is a great friend eventhough he looks better than me in a dress (unfair!). Vincent, the francophile, gave me hours and hours of french language entertainment and showed me that we all must eventual finish our theses. Ben always organized dam fabulous outings ;) and reminded me that you can get out of MIT if you try (although I still think he should have come back for the Ph.D.) Anne was always ready for some extra girly fun (Mr. Darcy rocks!). Raffi will always be the little bro I never had (told you I would get out before I spend a DECADE at MIT!)

I want to thank my family. My parents in law, Barbara and Rodney, were always very supportive and sent me lots of great articles from the ACS. Sarah and now Jake, my siblings in law, had a great wedding where I caught the thesis and which I am sure helped me graduated in a timely fashion (also, they sent me the best bouquet ever after my defense :) My mom and dad, Catherine and Christian, have inspired me more than I can say. I mean I want to be "just like them" when I grow up and I hope I'm getting there. My sister, Cécile, always cheered me up and gave me lots of encouragement when I was down in the dumps (plus when she leaved on campus she let me crash at her place on several occasions). Last but not least, I want to thank

my husband, Brian. He made sure I could get through this, he cooked me dinner, he held my hand, he sat through ~ 5 performances of my thesis defense talk, and he always told me everything was going to be ok and look... he was right! :)

This research was funded in part by Whitaker Foundation Graduate Fellowship.

Contents

List of Figures

List of Tables

Chapter 1

Introduction

1.1 Background

Articular cartilage is the load bearing connective tissue found on the surface of movable joints. It normally sustains high compressive loads, $10 - 20MPa$, without damage. The biomechanical properties of cartilage, such as its high compressive resistance, are directly related to the molecular structure of extracellular macromolecules. Using high resolution force spectroscopy, it is now possible to directly measure the molecular nanomechanical properties of cartilage matrix macromolecules. In order to properly interpret these data and to understand the origins of the properties measured, theoretical models which take into account some of the molecular level structure of the system need to be developed.

1.2 Objective

The motivation of this research is to determine the underlying molecular mechanisms responsible for the macroscopic compressive stiffness of cartilage tissue. It is believed that this compressive stiffness is largely due to large molecules called aggrecan found throughout cartilage tissue. Aggrecan is composed of a core protein to which are attached many highly charged glycosaminoglycan (GAG) chains. The nanomechanical properties of aggrecan, primarily electrostatic repulsion between its GAG chains,

are thought to be one of the major determinants of the high compressive stiffness of cartilage tissue. The goal of the thesis is a thorough study of the normal compressive interactions between aggrecan molecules. This research can contribute to a better understanding of the way cartilage works and of the factors that contribute to its degradation with age and disease. From a broad perspective, these studies consists of a set of experiments to measure the molecular-level interactions between aggrecan, the results of which will be compared to and used to develop better theoretical models of these interactions.

High resolution force spectroscopy (HRFS) instruments, like the atomic force microscope (AFM) and the molecular force probe (MFP), make it possible to not only image macromolecules such as aggrecan but also measure the small nano-Newton scale forces associated with their interactions in a variety of environmental conditions. However, in order to better understand the origin of these forces one must establish a connection between the experimental data and mathematical models based on polymer theory. The aggrecan compressive interactions between aggrecan layers were measured directly using both contact imaging and normal HRFS probing. Aggrecan was end-grafted to substrates and brushes in densities relevant to physiological conditions. The forces were measured as the tip and substrates were brought in contact (probing). To further characterize the behavior of these aggrecan "brushes" the height of the layer was measured under different normal loads used during contact imaging.

The measured aggrecan interaction forces were compared to continuum models. This required the development of models designed for the specific molecular-level geometry of our system. These models account for specific features of the molecular structure important for their function, and give good insight into some of the configuration of cartilage macromolecules under physiological conditions.

1.3 Overview

This thesis is structured as follows. Chapter 2 provides a brief overview of the cartilage extracellular matrix and aggrecan. A short background on the instruments used in this thesis, the AFM and the MFP, as well as the differences between the two machines is provided in Appendix A. The models used in this thesis are presented in Chapter 3, which published Langmuir in 2003,[24] with further discussion in Appendices B-E. Chapter 4 describes the height measurements on aggrecan brush layers. Chapter 5 contains the results of the normal force measurements between aggrecan brushes and compares these to the models and to whole tissue compressive stiffness measurements. Appendix F describes in details the issues with converting nanomechanical data to stress-strain. Appendix G contains the specific on end-grafting of aggrecan to gold. Appendices H and I provide further experiments on the behavior of aggrecan during compression.

Chapter 2

Background

Articular cartilage is the load bearing connective tissue found on the surface of movable joints. It normally sustains high compressive loads, $10 - 20MPa$, without damage. The biomechanical properties of cartilage, such as its high compressive resistance, are directly related to the molecular structure of extracellular macromolecules.

2.1 Cartilage and its extracellular matrix (ECM)

Cartilage is a very complex avascular and alymphatic tissue (Figure 2-1). Articular cartilage tissue is composed of 70-80% water by weight and contains only $20 - 40$ thousand cells, called chondrocytes, per cubic millimeter [63, 64]. However, this low density of cells maintains the extracellular matrix (ECM) under normal conditions. The ECM is produced and maintained by the chondrocytes. While it is composed mostly of water, it is surprisingly strong mechanically. The different macromolecular structures of the ECM account for different mechanical properties. The collagen molecules contribute to the tissues' shear and tensile strength, while the highly charged proteoglycan molecules provide most of the compressive strength.[11, 63]

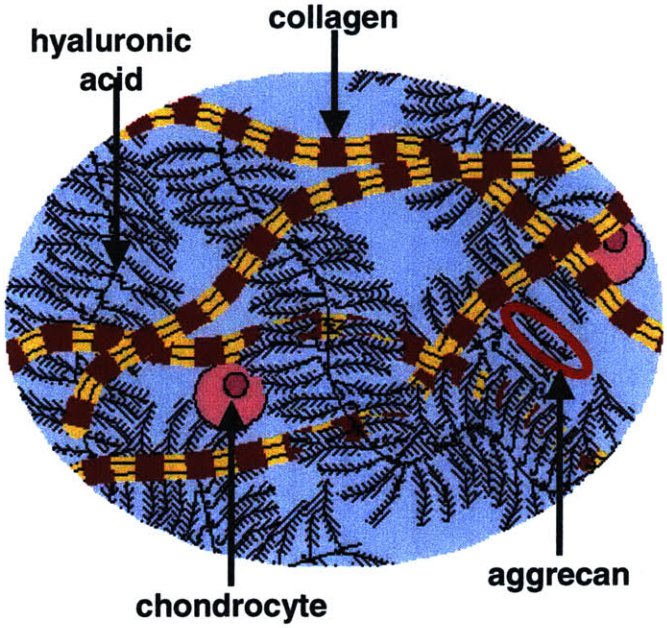

Figure 2-1: The structure of cartilage (not drawn to scale).

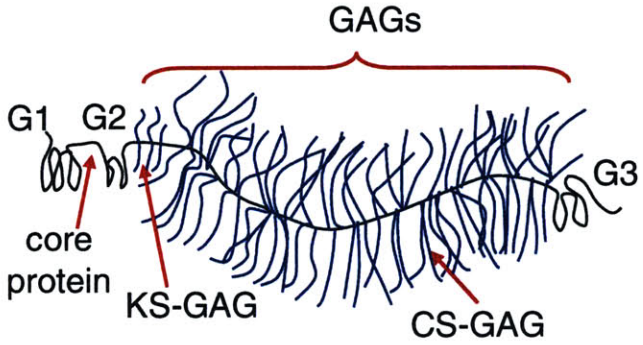

Figure 2-2: Schematic drawing of aggrecan, a proteoglycan. CS-GAG = chondroitin sulfate, KS-GAG = keratan sulfate and GAG = glycosaminoglycan.

2.2 Aggrecan

Proteoglycans make up 5-10% of the cartilage wet weight (35% by dry weight).[64] In articular cartilage, aggrecan is the most abundant proteoglycan (Figure 2-2). It is composed of a long core protein (225-250 kDa[47] and several hundred nanometers long[68]) to which glycosaminoglycan (GAG) chains are covalently bound. The core protein of aggrecan contains three globular domains (see Appendix G Figure G-5 for the whole amino acid sequence). The first, G1, is found near the amino-terminal and uses a link protein to attach to the binding region of hyaluronan, a glycosaminoglycan consisting of several thousand repeating disaccharide units. The second globular domain, G2, is found further down on the core protein and the third globular domain, G3, is found near the carboxyl-terminal of the core protein. Between G2 and G3 is a highly charged glycosaminoglycan rich region and most of the mass of aggrecan is GAGs. Of the GAGs, most of them are chondroitin sulfate although there is some keratan sulfate.[47] Proteoglycans, such as aggrecans, form large aggregates with hyaluronan (Figure 2-1).

It is known that certain structural changes in aggrecan occur with age, disease, and species.[76, 77] The length and sulfation pattern of the GAG chains and the proportion of the long chondroitin sulfate (CS) to the shorter keratan sulfate (KS) GAG will change. It is known that the ratio of 6-sulfated to 4-sulfated CS goes from < 1 in the fetal and newborn infant to > 20 in adult tissue.[77] The proteoglycans from deeper tissue (tissue nearer to the bone-cartilage interface) have been shown to have smaller CS-rich region than those nearer to the surface.[38] Also with age and disease, enzymes (aggrecanases) cut the core protein of aggrecan at known cites that start on the C-terminus of the protein.[9, 10, 29, 34, 73, 86]

In this thesis, most of the experiments were done with aggrecan extract from bovine fetal epiphyseal cartilage. Ng et al. reported some of the structural parameters for this type of aggrecan as measured with tapping-mode atomic force microscopy (AFM) in air (Figure 2-3) and these are summarized here.[68] The core protein contour length (the full length) was $398 \pm 57nm$ and its persistence length was $\sim 110nm$. The

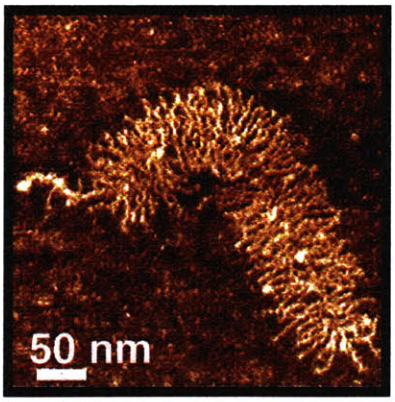

Figure 2-3: Tapping-mode AFM image in air of an aggrecan molecule from bovine fetal epiphyseal cartilage courtesy of Laurel Ng.[68]

GAG chains had a contour length of $42 \pm 7nm$, a persistence length of $21nm$, and they were $\sim 3.2 \pm 0.8nm$ apart along the core protein. The chondroitin sulfate (CS) GAGs were found to have 50 disaccharides per chain.

2.2.1 Glycosaminoglycan

Aggrecan contains three major types of glycosaminoglycans (GAG): chondroitin-6-sulfate, chondroitin-4-sulfate, and keratan-sulfate. The keratan-sulfate chains, which are $\sim$ 5kDa, are the shortest consisting of about 10 repeating disaccharides. These chains are located mainly near the G2 region of the core protein.[48] The chondroitin-sulfate (CS) chains occupy most of remaining GAG-rich region of aggrecan and comprise 95% of the molecular weight of the entire proteoglycan molecule (Figure 2-4).

In general, the chondroitin-sulfate chains are $30 - 40nm$ long and are spaced approximately $2 - 4nm$ apart on the core protein. One end of the CS is covalently linked to the core protein on Ser-Gly residues[48, 47] while the reducing end points into the intra-tissue space (Figure 2-4a). The CS-GAG chain is composed of alternating glucuronic acid and N-acetyl-6(or 4)-sulfate galactosamine (Figure 2-4b). Under normal physiological conditions, the carboxylic acid and the sulfate groups are negatively charged.

It has been found that the sulfation of GAG chain is decreased in cartilage disease,

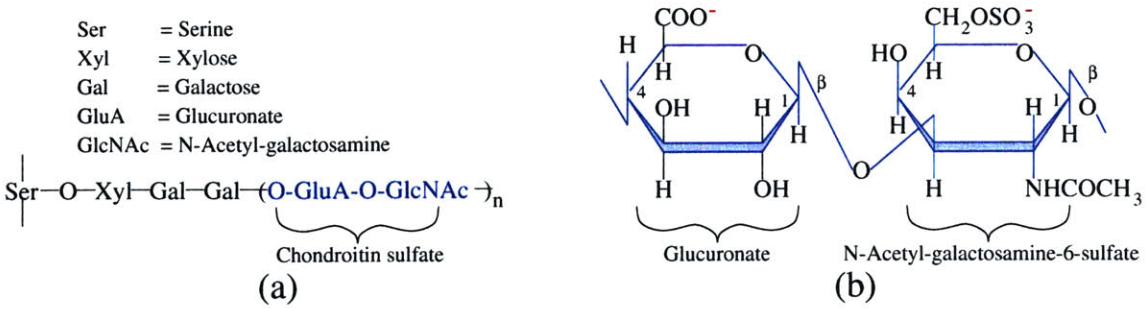

Figure 2-4: (a) The structure of GAG; (b) Molecular structure of Chondroitin-6-sulfate.

such as osteoarthritis. [75] Also, studies have shown that with age, the amount of CS decreases compared to the amount of KS and that the CS and to a lesser degree the KS chains become shorter with age.[95, 68] Studies have shown with macroscopic measurements [11] that the high negative charge of the GAG molecules is the major determinant of cartilage compressive loading properties, responsible for 50-75% of the equilibrium modulus in compression.

Chapter 3

Modeling of Polyelectrolyte Brushes

This chapter was published as a paper in Langmuir in 2003.[24] Further details and applications of the models presented here are also provided in Appendix B to D.

3.1 Introduction

Polyelectrolyte brush systems are important in many areas of polymer physics, surfactant science, biophysics, cell biology, and physiology and have technological applications in colloid stabilization, surface lubrication, stimulus-responsive surfaces, and optoelectronics. Tethered polyelectrolyte brushes also occur as natural components of biological tissues and on cell surfaces and play a significant role in their mechanical, chemical, and hydrodynamic properties.[3, 20] In this paper, we set forth a general theoretical framework to predict the nanoelectromechanical behavior of polyelectrolyte brushes and then apply it to a model system consisting of negatively charged biological macromolecules known as chondroitin sulfate glycosaminoglycans (CS-GAGs).[11, 30] CS-GAGs have been studied extensively, as their intermolecular electrostatic repulsive forces are responsible for $> 50\%$ of the equilibrium compressive modulus of the articular cartilage.[11] CS-GAGs have a contour length of $\sim 35nm$ and in cartilaginous tissues most CS-GAGs are covalently bound $2-4nm$ apart along

a core protein to form the brush-like proteoglycan, aggrecan.[66] We have recently reported direct molecular-level measurements of the repulsive interactions of an end-grafted CS-GAG brush layer using the technique of high-resolution force spectroscopy (HRFS) in aqueous solution.[89] The CS-GAG model system provides a wide variety of experimental conditions with which to rigorously test theoretical predictions, including ionic strength, pH, and grafting density.

There have been several different approaches used in the literature for modeling polyelectrolyte brush interactions. Molecular dynamic simulations of individual polyelectrolyte macromolecules have provided information on chain conformation and supramolecular structure. However, since brush layers involve the interactions between many molecules (e.g. polymer chains, ions, and water molecules), this technique is computationally intensive and currently has limited application for predicting brush interaction forces at physiological conditions.[19] Scaling theory is another method used to characterize polyelectrolyte brush interactions,[74, 80, 102] and provides straightforward analytical solutions.[74] However, each scaling law can only be applied to certain distinct sets of experimental conditions (e.g. solution ionic strength, pH, polymer density, chain length).[102] Continuum theory, e.g., Poisson Boltzmann (PB) - based models,[33, 71, 96] is applicable to a wide range of experimental conditions while still remaining computationally tractable and allows direct quantitative comparison with experimental data. However, the PB approach does not account for structure and interactions at the atomic level.

The objective of this study was to use a continuum approach to model the electrostatic component of interactions between polyelectrolyte molecules in a brush layer, to calculate the nanoscale electrostatic interaction forces, and to better understand how molecular level changes in the fixed charge distribution affect these interaction forces. The applicability and accuracy of three increasingly refined theoretical models (Fig. 3-1) based on the PB equation were examined via a rigorous quantitative comparison with high resolution force spectroscopy (HRFS) experimental data on a model CS-GAG brush system.[89] The PB approach predicts the electrostatic double layer force between charged surfaces due to electrical and osmotic interactions associ-

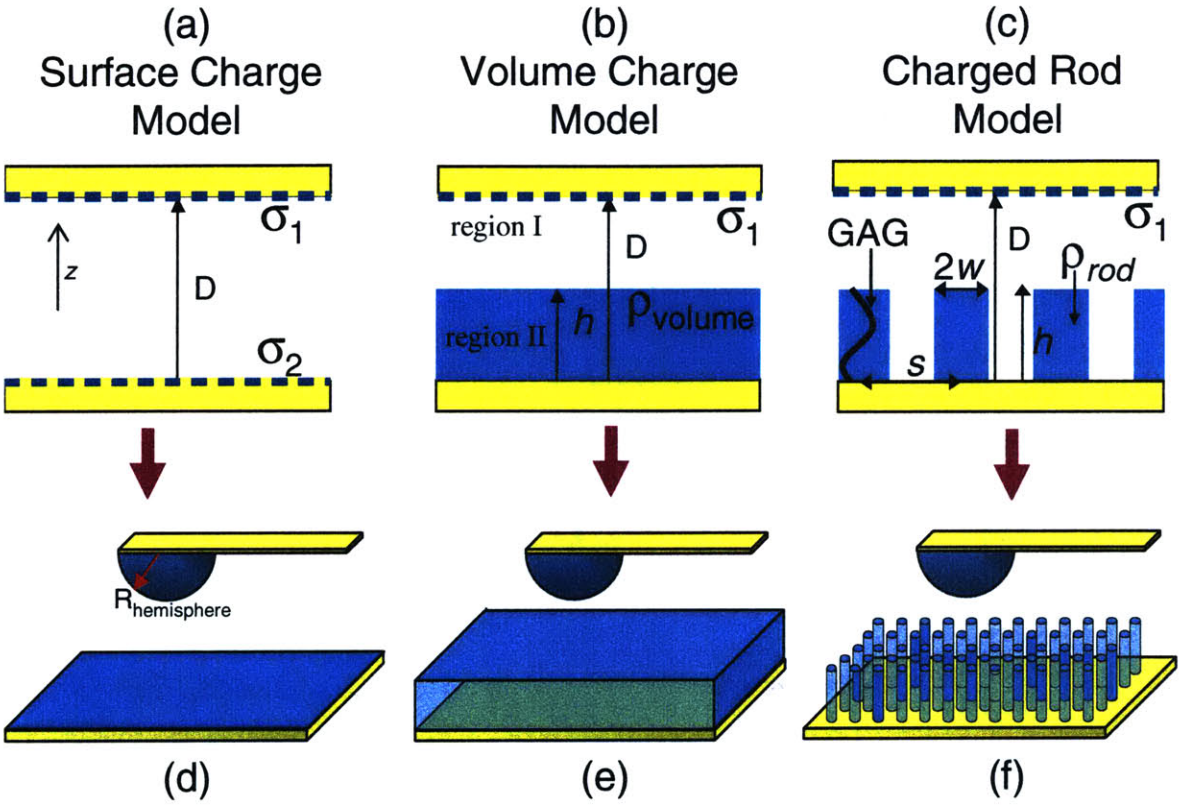

Figure 3-1: Schematic of the three different models discussed: (a) constant surface charge model, (b) constant volume charge model, and (c) charged rod model. The probe tip geometry is approximated as a hemisphere in (d)-(f)

ated with polyelectrolyte fixed charge and the mobile ions in solution. The first two models have been reported previously in the literature[12, 71] and the third newly developed model is reported here for the first time. Each of the three models employs increasingly more geometrically-specific representations of the polyelectrolyte macromolecular fixed charge.

In the first model (Fig. 3-1a), a polyelectrolyte brush layer is represented as a uniform, flat constant surface charge density.[12] The second model (Fig. 3-1b) approximates the polyelectrolyte brush as a uniform volume charge density.[71] Even though this model takes into account the height of the brush, the molecular shape and charge distribution along the polyelectrolyte chain backbone are not included. The third model (Fig. 3-1c) represents the time average space occupied by the individual polyelectrolyte macromolecules in the brush as cylindrical rods of uniform volume charge density and finite height. This approach attempts to account for additional aspects of polymer molecular geometry and nonuniform molecular charge distribution inside the brush. It should be noted that this model is different from the "unit cell" model[58] where each polyelectrolyte macromolecule is represented as an infinitely long cylinder having a fixed surface charge. First, the electrical potential and the spatial distribution of ions were computed in the region between a planar brush layer and a charged planar surface situated above the brush as a function of separation distance D, shown in Fig. 3-1a-c. Then, the electrostatic forces between the brush and the charged planar surface predicted by each of these 3 models were compared to each other using a range of model parameters and bath ionic strengths. The models were then adapted to the experimental configuration[5] of Fig. 3-2, incorporating the geometry of a hemispherical probe tip with known surface charge density situated above the brush (Fig. 3-1d-f) instead of the charged planar surface. Model predictions were then compared to HRFS measurements of the total repulsive force reported in the literature by us.[89] Because the equations relating the electrostatic force to the known system parameters (e.g., GAG charge density and bath ionic strength) are nonlinear and are difficult to solve analytically, finite difference methods (FDM) were used to obtain numerical solutions of the models.

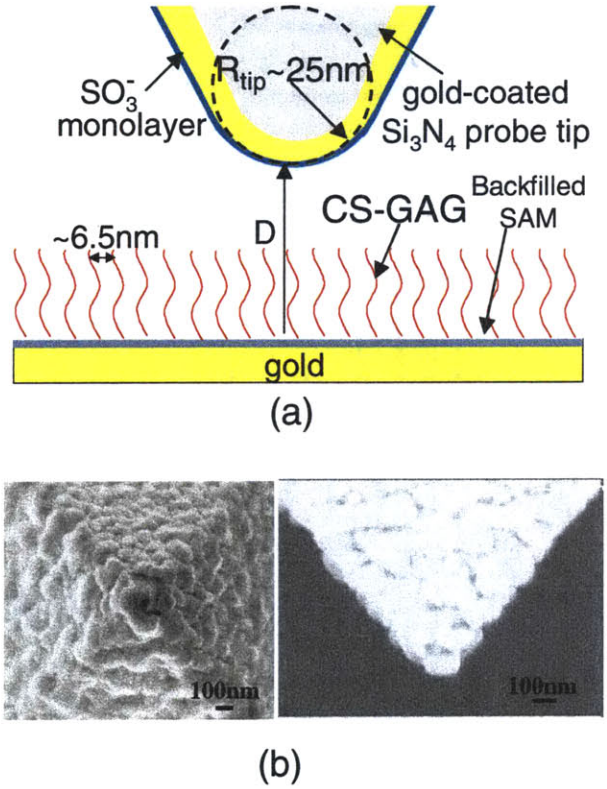

Figure 3-2: (a) Schematic diagram of high-resolution force spectroscopy experiment (HRFS) of sulfate functionalized probe tip versus end-grafted CS-GAG polymer brush. (b) SEM pictures of the probe tip.

3.2 General Theoretical Methods

The Poisson-Boltzmann (PB) equation relates the spatial distribution of the electrical potential, Φ, in an electrolyte solution[26, 101] to the concentration of fixed and mobile charges within the electrolyte and at the boundaries of the solution phase, i.e., the charges that are the source of the electric field and potential. The resulting Φ obtained from solution of the PB equation can can then be used to compute forces of electrical origin on charged species or structures (e.g., a hemispherical probe tip) within the region of interest. The PB equation is base on several simplifying assumptions[101, 50] including: (a) the permittivity, ϵ, is everywhere the same as that of the bulk solution, $\epsilon_w = 6.92 \cdot 10^{-10} C/Nm^2$, and is independent of any electric field, (b) time varying magnetic fields are negligible (i.e., the system is electroquasistatic), (c) the ions in solution are treated as point charges and therefore take up no volume, and (d) the system is assumed to be in thermodynamic equilibrium.

From assumption (a) above, the electric field, $\mathbf{E}$, can be related to the total volume space charge density, ρ_{total}, using Gauss's law:

$$\nabla \cdot \epsilon \mathbf{E} = \nabla \cdot \epsilon_w \mathbf{E} = \rho_{total} \tag{3.1}$$

In general, $\mathbf{E}$ is related to the time varying magnetic field, $\mathbf{H}$, using Faraday's law:

$$\nabla \times \mathbf{E} = -\frac{\partial}{\partial t}(\mu \mathbf{H}) \tag{3.2}$$

When the time rates of change in 3.2 are small enough, or the magnetic field is negligibly small, the right hand side of 3.2 tends to zero (assumption (b) above) and we can then define a scalar potential, Φ, related to the quasistatic $\mathbf{E}$ field by:

$$\mathbf{E} = -\nabla \Phi \tag{3.3}$$

which automatically satisfies the quasistatic form of 3.2. From 3.1 and 3.3, the po-

tential and space charge distribution are then related by Poisson's equation:

$$\nabla^2\Phi = -\frac{\rho_{total}}{\epsilon_w}. \tag{3.4}$$

In our system, the total space charge, ρ_{total}, is the sum of that due to the mobile ions in solution, ρ_{mobile}, and any fixed charges present, ρ_{fix}:

$$\nabla^2\Phi = -\frac{\rho_{mobile} + \rho_{fix}}{\epsilon_w} \tag{3.5}$$

The ion distributions in solution are assumed to obey Boltzmann statistics in thermodynamic equilibrium and, therefore, the i^{th} mobile ion concentration, c_i, is related to the potential by:

$$c_i = c_{io}e^{-\frac{z_iF}{RT}\Phi} \tag{3.6}$$

where z_i is the valence of species i, F is the Faraday constant ($= 96500C/mole$), R is the universal gas constant ($= 8.314J/mole \cdot K$), and the reference potential $\Phi = 0$ is taken to be the potential of the bath where $c_i = c_{io}$. In 3.6, the potential of the average force on the ions is assumed to be the electrical potential of the mean field in Poisson's equation (3.4).[33] From equation 3.6, the total charge density can be expressed as:

$$\rho_{total} = \sum_i z_iFc_{io}e^{-\frac{z_iF}{RT}\Phi} + \rho_{fix} \tag{3.7}$$

Poisson's equation (3.4) then takes the general form of the Poisson-Boltzmann equation:

$$\nabla^2\Phi = -\left(\frac{\sum_i z_iFc_{io}e^{-\frac{z_iF}{RT}\Phi} + \rho_{fix}}{\epsilon_w}\right) \tag{3.8}$$

For an electrolyte bath containing a monovalent salt (such as NaCl) having bath concentration C_0, and assuming that C_0 is significantly greater than the concentration of protons coming from dissociation of fixed charge groups (e.g., the concentration of protons coming from dissociation of GAG carboxylate and sulfate fixed charge groups is small compared to bath NaCl), then equation 3.8 reduces to the familiar 1:1 electrolyte form of the the Poisson-Boltzmann equation[26, 87] with an added fixed

salt concentration	Approximate κ^{-1}
0.0001M NaCl	$30nm$
0.001M NaCl	$10nm$
0.01M NaCl	$3nm$
0.1M NaCl	$1nm$
1M NaCl	$0.3nm$

Table 3.1: Values of the Debye length, κ^{-1}, at the different salt concentrations used in the experiments.

charge term:

$$\nabla^2\Phi = \frac{2FC_0}{\epsilon_w}\sinh\left(\frac{F\Phi}{RT}\right) - \frac{\rho_{fix}}{\epsilon_w} \tag{3.9}$$

To uniquely determine the potential from equations 3.8 and 3.9, two boundary conditions on either the potential or its derivative (the electric field) are required. In this study, constant charge boundary conditions on both bounding surfaces are employed because in the experiments,[89] neither the probe tip nor the substrate is electrically connected to any source that would maintain them at a constant potential. In addition, the surface charge of the tip and the GAG charge on the substrate are initially known, and they are essentially constant within the range of bath pH and ionic strength conditions used (see Appendix B).[17] For example, if the charge on the tip is defined as σ_1 and the charge on the substrate surface is σ_2 in Fig. 3-1a then from Gauss's law with the z-direction defined as show in Figure 3-1a, the boundary conditions at those surfaces will be: $\frac{\partial\Phi}{\partial z} = \frac{\sigma_1}{\epsilon_w}$ and $\frac{\partial\Phi}{\partial z} = -\frac{\sigma_2}{\epsilon_w}$, respectively. The length scale over which the electrostatic potential decays is known as the Debye length, κ^{-1}, which comes from the solution of the linearized PB equation (3.9) and takes the form with valence $z_i = 1$:

$$\kappa^{-1} = \sqrt{\frac{\epsilon_w RT}{2F^2C_0}} \tag{3.10}$$

From 3.6, the counter-ion and co-ion concentrations in the fluid phase in thermody-

namic equilibrium are related to the potential as:

$$c_+ = C_0 e^{-\frac{F}{RT}\Phi} \tag{3.11}$$

$$c_- = C_0 e^{+\frac{F}{RT}\Phi} \tag{3.12}$$

Once the potential, Φ, has been determined from the solution of the PB equation, the electrostatic free energy can be calculated from the spatial distribution of the potential:[91, 92]

$$W_e(z,q) = \int_{\text{surface}} \sigma\Phi dS + \int_{\text{volume}} \rho_{fix}\Phi dV - \int_{\text{volume}} \left(2RTC_o(\cosh\left(\frac{F\Phi}{RT}\right) - 1) + \frac{\epsilon_w}{2}(\nabla\Phi)^2\right) dV \tag{3.13}$$

The total electrostatic free energy in equation 3.13 is the sum of terms associated with (a) fixed charge groups on surfaces or in the volume (i.e., the 1st and 2nd terms on the right hand side), and (b) mobile ionic charges (e.g. Na^+, and Cl^-) in solution, which give rise to local osmotic and electric field stresses (i.e., the 3rd and 4th terms of 3.13, respectively).[91]

Finally, the z component of the force of electrical origin acting in the z-direction on the upper surface of the system of Figure 3-1 can be calculated from the z-derivative of the free energy while keeping the charge constant:

$$\mathrm{F}_z = \left(-\frac{\partial W_e}{\partial z}\right)\Big|_{q \text{ constant}} \tag{3.14}$$

This force is equal and opposite to that acting on the lower surface containing the brush layer. The PB equation is generally nonlinear and is therefore difficult to solve analytically except for cases in which the boundary conditions have a simple geometric structure. Therefore, numerical techniques are used to solve the models below.

Parameters	Surface Model	Volume Model	Rod Model
σ_1 (C/m^2)	-0.015	-0.015	-0.015
Q (C)	-8.00×10^{-18}	-8.00×10^{-18}	-8.00×10^{-18}
s (nm)	6.5	6.5	6.5
h (nm)	(NA)	Variable	Variable
w (nm)	(NA)	(NA)	Variable
$\sigma_2 = Q/s^2$ (C/m^2)	-0.19	(NA)	(NA)
$\rho_{volume} = Q/(s^2h)$ (C/m^3)	(NA)	$-0.19/h$	(NA)
$\rho_{rod} = Q/(\pi w^2 h)$ (C/m^3)	(NA)	(NA)	$-8.00 \cdot 10^{-18}/(\pi w^2 h)$

Table 3.2: Model parameters used to compare th surface, volume, and rod model predictions to HRFS experimental data. The parameters denoted as variable (h and w) were adjusted to fit the data using the method of least squares.

3.3 Models of Electrostatic Free Energy and Force

3.3.1 Constant Surface Charge Model

The first model[12, 72] (Figure 3-1a) has been used in the literature[2, 1, 106] to approximate the electrostatic force caused by deformation of a polyelectrolyte brush. All fixed charges on the polyelectrolytes are represented as a constant charge density that is collapsed on a surface, and there is no bulk fixed charge density away from the surface ($\rho_{fix} = 0$). In this case, the Poisson-Boltzmann equation (3.9) reduces to:

$$\nabla^2\Phi = \frac{2FC_0}{\epsilon_w}\sinh\left(\frac{F\Phi}{RT}\right) \tag{3.15}$$

When the separation distance, D, between the two charged planes is large compared to the Debye length ($\kappa D >> 1$), an analytical solution[41, 16] for the potential can be obtained from the nonlinear PB equation. However, as the two charged planes are brought closer together, this analytical solution is no longer valid and to obtain the force as a function of surface separation distance a Newton-Raphson method on

finite differences[36, 81] was used to solve the nonlinear PB equation subject to one boundary condition at each surface (see Appendix B). The force between two charged planes of infinite extent (Fig. 3-1a) was first obtained. Then, to compare to the experimental HRFS data, this force per unit area was numerically integrated to give the total force between a hemispherical tip and planar substrate of infinite extent (Fig. 3-1d). Since this problem is one dimensional, the potential in space can be represented as a one-dimensional matrix or vector in which each entry is the potential at N evenly spaced points along the z-direction. The derivatives in the z-direction can be calculated as differences between neighboring points. The PB equation for each discrete entry plus the boundary conditions give a set of N nonlinear equations all satisfied if the potential at each point is correct. If a close enough initial guess for the value of the potential at all points is given, then that guess can be refined using a Taylor series expansion. This is repeated iteratively until the change in potential at each step is smaller than an error threshold. This algorithm is known as a Newton-Raphson method for solving multidimensional systems. The geometry at the end of the blunted square pyramidal probe tip (Fig. 3-2b) was modeled as a hemisphere whose radius, $R_{hemisphere}$, is equal to the radius of curvature of the probe tip, R_{tip} (Fig. 3-1d). This hemispherical geometry is approximated by using the calculated force between the flat surfaces and summing up the force on appropriately sized concentric cylinders. This method, based on the original formulation of Derjaguin[25] and sometimes known as Surface Element Integration (SEI),[5] is the numerical version of the integral of a uniform normal stress or pressure over the surface of the hemisphere tip (see Appendix C). When comparing model predictions to experimental data, no fitting parameters were employed since the charge density due to the sulfate monolayer on the tip, $\sigma_{tip} = \sigma_1$, and the effective charge density due to the GAG brush on the substrate, $\sigma_{GAG} = \sigma_2$, are both known (see Table 3.3).

3.3.2 Volume Charge Model

The length of polyelectrolyte macromolecules in a brush layer are often much longer than κ^{-1}; for example, in the model system of interest the GAG contour length is

$\sim 35nm$ and $\kappa^{-1} \sim 1nm$ at physiological IS. Under these conditions, the brush can be modeled as a region of uniform fixed volume charge density, volume, using the approach of Ohshima[71] (Fig. 3-1b). As with the planar surface charge model, the force is first calculated numerically using infinite plate geometry (Fig. 3-1b) and then, to compare to experimental data, converted to a hemispherical geometry (Fig. 3-1e).

In the electrolyte region I above the fixed volume charge (Fig. 3-1b), the PB equation has the form of equation 3.15. In region II inside the fixed volume charge, the PB equation has a term accounting for the polyelectrolyte brush fixed volume density, volume:

$$\nabla^2\Phi = \frac{2FC_0}{\epsilon_w}\sinh\left(\frac{F\Phi}{RT}\right) - \frac{\rho_{volume}}{\epsilon_w} \tag{3.16}$$

Since this is a two-region problem, the solutions to equation 3.15 in region I and equation 3.16 in region II are subject to boundary conditions at the tip and substrate surfaces and at the interface between the volume charge and the electrolyte bath (Fig. 3-1). At the surfaces, the boundary conditions from Gauss' Law have the same form as before: at the tip, the derivative of the potential is proportional to the tip surface charge density ($\frac{\partial\Phi}{\partial z} = \frac{\sigma_1}{\epsilon_w}$); at the substrate surface, however, there is no longer a surface monolayer of charge and, therefore, $\frac{\partial\Phi}{\partial z} = -\frac{\sigma_2}{\epsilon_w} = 0$. In practice, there may be some induced surface charge on the substrate but that charge can be shown to be negligible compared to the volume charge density associated with the polyelectrolyte brush. At the interface between the polyelectrolyte volume charge density and the electrolyte bath, the potential and its derivative (the electric field) must be continuous. Having obtained solutions for the potential from equations 3.15 and 3.16, the electrostatic free energy can now be computed as before. The fixed volume charge term in the free energy calculation of equation 3.13 is now specified as that associated with the brush volume:[91]

$$\begin{aligned} W_e(z,q) &= \int_{\text{surface}} \sigma\Phi dS + \int_{\text{volume of brush}} \rho_{volume}\Phi dV \\ &\quad - \int_{\text{volume}} \left(2RTC_o(\cosh\left(\frac{F\Phi}{RT}\right) - 1) + \frac{\epsilon_w}{2}(\nabla\Phi)^2\right) dV \end{aligned} \tag{3.17}$$

When the distance between the surfaces, D, is less than the initial height of the volume charge, h, (i.e., the initial brush height), the model reduces to that of a single region containing a volume fixed charge density. The PB equation in this case has the form: polyelectrolyte brush fixed volume density, volume:

$$\nabla^2\Phi = \frac{2FC_0}{\epsilon_w}\sinh\left(\frac{F\Phi}{RT}\right) - \frac{\rho'_{volume}}{\epsilon_w} \tag{3.18}$$

where $\rho'_{volume} = \rho_{volume}(\frac{h}{D})$ While the PB equation is nonlinear, the problem is still one-dimensional due to symmetry and thus can be solved numerically using a method similar to that described for the surface model above. To compare this model to the data, there is one fitting parameter, h, since the brush height of the GAG on the substrate may differ from the GAG contour length and is therefore unknown. The volume charge density in the brush, ρ_{volume}, depends on the brush height, $\frac{\sigma_{GAG}}{h} = -\frac{0.19}{h}\ C/m^3$, and the other parameters are fixed to their known values (Table 3.3).

3.3.3 Charged Rod Model

When polyelectrolyte macromolecules in a brush (Fig. 3-1c) are separated by lateral distances, s, greater than κ^{-1}, there is a nonuniform distribution of charge inside the brush layer which will affect the force in a manner not predicted by the smooth uniform volume or surface charge models described above. For example, in our experiment, the end-grafted GAG polyelectrolyte macromolecules are $\sim$ 6.5 nm apart while $\kappa^{-1} \sim 1$ nm at physiological IS. We have therefore developed a more refined "charged rod" model in which a rod-shaped circular cylinder having radius, w, finite height, h, and fixed uniform volume charge density, ρ_{rod}, represents the time-averaged space occupied by an individual polyelectrolyte chain and its fixed charge groups (Fig. 3-1c). The charged rods are separated by regions of zero fixed charge. When $w = \sqrt{\frac{s^2}{\pi}}$, the charged rod model becomes equivalent to the volume charge model described above. Upon conversion of the planar geometry, the probe tip is represented as a hemisphere with constant surface charge density, σ_1, and the planar substrate-polyelectrolyte brush becomes a field of rods, each with volume charge density, ρ_{rod} (Fig. 3-1f). In

the fluid region between or above the rods, the PB equation has the form of equation 3.15. Inside the rods, the PB equation has an additional term accounting for the fixed volume charge density, rod:

$$\nabla^2\Phi = \frac{2FC_0}{\epsilon_w}\sinh\left(\frac{F\Phi}{RT}\right) - \frac{\rho_{rod}}{\epsilon_w} \tag{3.19}$$

The free energy calculation is also modified slightly from the volume charge model equation:

$$\begin{aligned} W_e(z,q) \;=\; & \int_{\text{tip surface}} \sigma\Phi dS + \int_{\text{volume of rod}} \rho_{brush}\Phi dV \\ & - \int_{\text{volume}} \left(2RTC_o(\cosh\left(\frac{F\Phi}{RT}\right) - 1) + \frac{\epsilon_w}{2}(\nabla\Phi)^2\right) dV \end{aligned} \tag{3.20}$$

The configuration of Fig. 3-1c is also a two-region problem, and boundary conditions are applied at the tip and substrate surfaces and at the peripheral edge surrounding each rod (Fig. 3-1c). At the tip and substrate surfaces, the boundary conditions are the same as in the volume model above. Along the interface between the rod-shaped volume charge density and the electrolyte phase, the potential and the electric field must be continuous. When $D < h$, the rod height is set to be D and the radius of the rod is expanded to keep the total rod volume and therefore ρ_{rod} constant. When $w = \sqrt{\frac{s^2}{\pi}}$, the rod model is equivalent to the volume charge model of Fig. 3-1b, and ρ_{rod} is scaled appropriately with D. To solve for the potential in space, the rod model was first subdivided into a single rectangular repeat unit containing one rod (repeat unit size: $s \times s \times D$, see Fig. 3-6). Since this unit has no further symmetry, the potential everywhere in space surrounding and within the single repeat unit was solved numerically using Newton-Raphson method with an inequivalent Jacobian on a 3D finite difference grid.[81] To compare this model to the HRFS experimental data, there were two fitting parameters, h and w, since both the brush height and the space occupied by one polyelectrolyte chain on the substrate are unknown. The volume charge density in the brush, rod, was $(\frac{-8.0\cdot10^{-18}}{\pi hw^2})$ C/m^3 (i.e., the known fixed

charge per GAG chain divided by the known volume it occupies[89]), and the other parameters (s, σ_1, and C_0) were fixed to their known values (Table 3.3).

3.4 Experimental Measurements

The force between a chemically end-grafted CS-GAG brush layer and a sulfate-functionalized probe tip (negatively charged at the solution C_0 and pH used, $pK_a = 2$) was measured in the configuration of Fig. 3-2 using a cantilever-based instrument, the molecular force probe (MFP, Asylum Res.). CS-GAG molecules were prepared from aggrecan proteoglycans that were synthesized by rat chondrosarcoma cells and metabolically radiolabeled in culture (see Seog et al.[89] for details). The GAG contour length was calculated to be $35nm$, which includes a $3nm$ linkage region containing carbohydrate and amino acid moieties. The CS-GAG chains were end-grafted onto $1cm \times 1cm$ gold-coated silicon substrates using methods previously described.[89] GAG grafting density on the wafer was calculated to be $\sim (6.5nm \times 6.5nm)$-area per chain. Based on the known charge distribution along CS-GAG chains, this grafting density corresponds to a brush layer volume fixed charge density of $\rho_{volume} \approx -10^7$ C/m^3 (Table 3.3) or, equivalently, a molar fixed charge density of $|(\frac{\rho_{volume}}{F})| \approx 0.1M$. Repulsive forces between the CS-GAG chains and a chemically modified gold-coated Si_3N_4 tip ($R_{tip} = 25nm$) functionalized with a sulfate monolayer ($\sigma_1 = -0.015$ C/m^2) were then measured in NaCl solutions in the concentration range of $C_0 = 0.01M - 1.0M$ at pH 5.6. Thus, C_0 was varied over the range of 0.1 to 10 times the molar volume fixed charge density of the brush layer ($\frac{\rho_{volume}}{F}$).

3.5 Model Predictions of Electrical Potential and Ion Concentration Profiles

We first compare and contrast the three model predictions of the electrical potential, Φ, and ion concentration profiles, c_- and c_+, in the planar configurations as a function of the inter-surface separation distance, D, the position within the inter-surface gap,

z, the bulk NaCl salt concentration (C_0), the volume charge height, h, and charged rod radius, w. (Figs. 3-3-3-6). These results will aid in the visualization of the spatial distribution of counter-ions and co-ion, the subsequent comparison of electrostatic interaction forces predicted by the models, and the comparison of model predictions with experimental data.

3.5.1 Constant Surface Charge Model

$\Phi(z)$ predicted by the surface charge model for two planar charged surfaces is shown in Fig. 3-1a for $1nm$ increments of D and a physiologically relevant $C_0 = 0.1M$ ($\kappa^{-1} = 1nm$). The values of the surface charge densities determined by previous experiments (σ_1 and σ_2 Table 3.3) are assumed to remain constant as D varies (constant charge boundary conditions, Appendix B). It is first important to note that the reference zero potential is that in the bath solution in all three models. When the surfaces are far apart compared to $\kappa^{-1} = 1nm$ (i.e. $\kappa D > 5$, or $D > 5nm$ in Fig. 3-3a), there is minimal interaction between the two surfaces, and the potential profile has a maximum value very close to zero. Therefore, the counter-ion (Na^+) and co-ion (Cl^-) concentrations between the two surfaces (Fig. 3-3b) are equal to C_0 when $D > 5$ at positions, z, a few away from either surface. When $\kappa D < 5$, the potentials at each surface begin to interact strongly, and the maximum potential between the surfaces is less than zero and therefore, the counter-ion concentration becomes higher and the co-ion concentration lower than C_0.

3.5.2 Volume Charge Model

$\Phi(z)$, predicted by the volume charge model is shown in Fig. 3-4a for $1nm$ increments of D, $C_0 = 0.1M$ ($\kappa^{-1} = 1nm$) using values for the volume and surface charge density and brush height relevant to our previous HRFS GAG experiments (Table 3.3, $\sigma_1 = -0.015\ C/m^2$, $\rho_{volume} = -9.44 \cdot 10^6\ C/m^3$, $h = 20nm$) When the surfaces are far apart (i.e., $D > 25nm$), the potential is uniform throughout most of the brush region, and is negative compared to the zero-reference potential in the bath

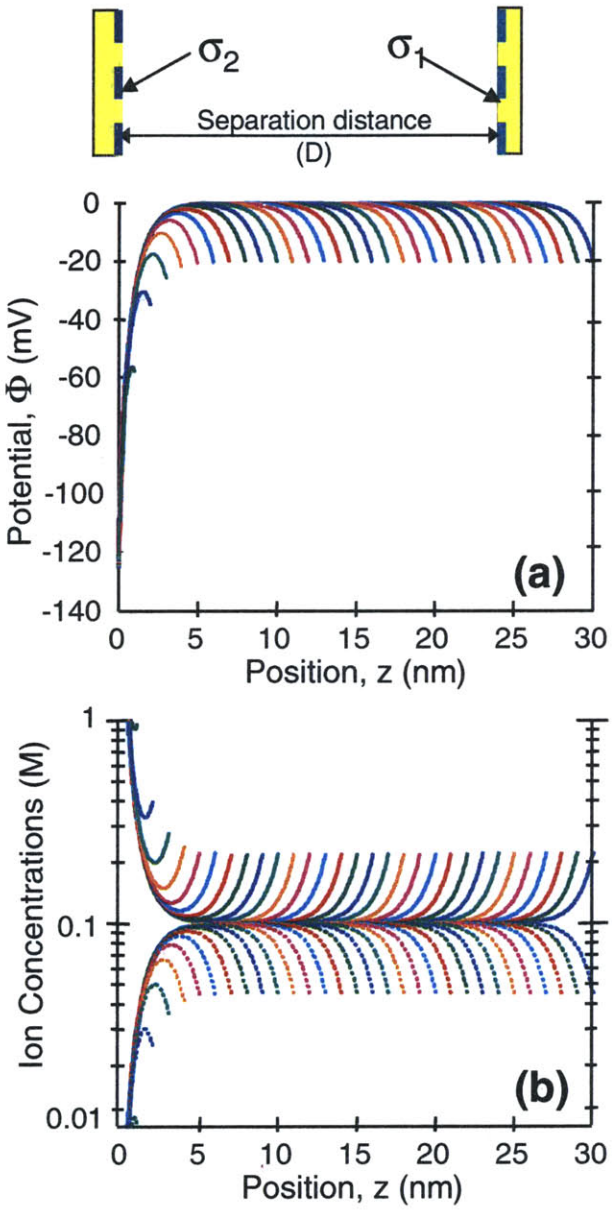

Figure 3-3: Plots of the potential and ion concentration profiles of the surface charge model as a function of separation distance. (a) Potential profile and (b) counter-ion (solid line) and co-ion (dotted line) concentration profiles are plotted at $1nm$ increments of separation distance with $\sigma_1 = -0.015\frac{C}{m^2}$ and $\sigma_2 = -0.19\frac{C}{m^2}$.

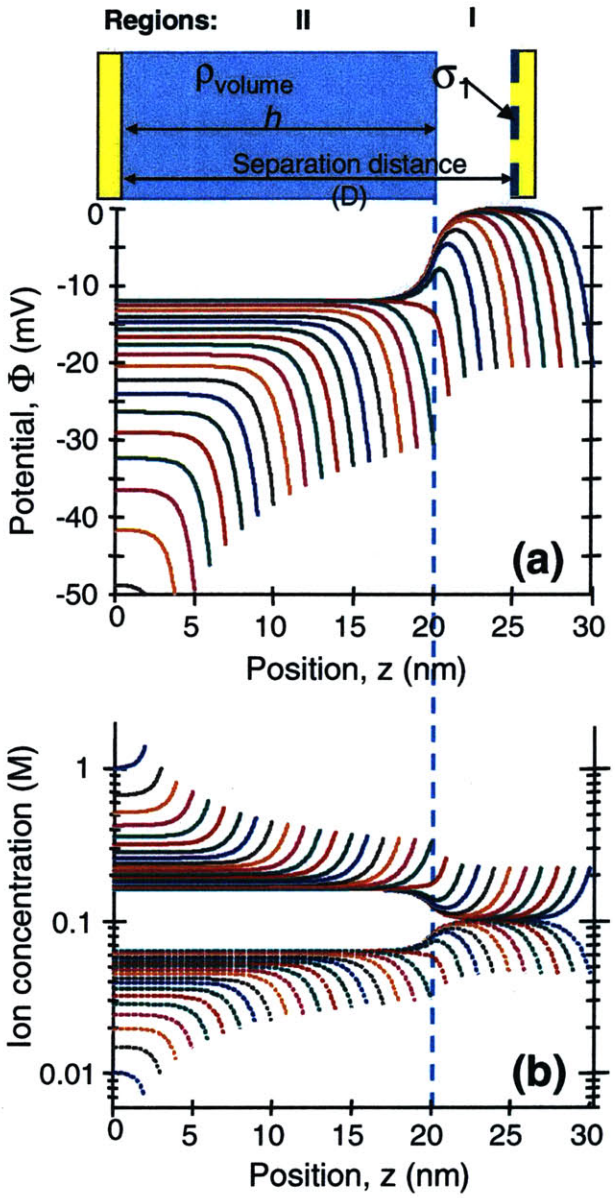

Figure 3-4: Plots of the potential and ion concentration profiles of the volume charge model as a function of separation distance. (a) Potential profile and (b) counter-ion (solid line) and codon (dotted line) concentration profiles are plotted at $1nm$ increments of separation distance with $\sigma_1 = -0.015\frac{C}{m^2}$, $h = 20nm$, and $\rho_{volume} = -9.44 \times 10^6 \frac{C}{m^3} \approx 0.0978M$.

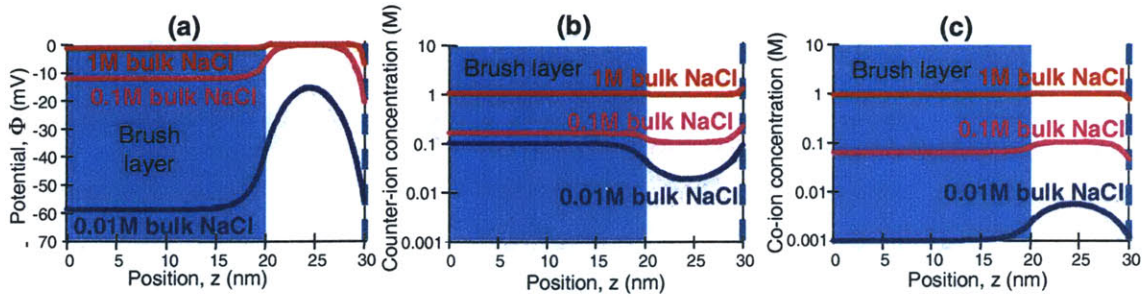

Figure 3-5: Plots of the potential and ion concentration profiles of the surface charge model as a function of separation distance. (a) Potential profile and (b) counter-ion (solid line) and co-ion (dotted line) concentration profiles are plotted at $1nm$ increments of separation distance with $\sigma_1 = -0.015\frac{C}{m^2}$ and $\sigma_2 = -0.19\frac{C}{m^2}$.

because of the uniform, negative fixed charge density of the brush. The potential then increases to zero over a transition zone of approximately $3 - 5\kappa^{-1}$ at the brush-bath interface, is uniform within the bath, and then transitions to a negative value at the right-hand negatively charged surface, consistent with the fixed surface charge boundary condition there. As D decreases to be within a few of h (i.e., $D < 25nm$), the potentials due to the negative volume and surface charges interact strongly, and the net resulting potential is always negative (below the zero reference state). For D ¡ h, the potential is uniform within the uniformly compressed brush region up to 3-5 from the surface, and is increasingly negative as further compression (i.e. decreases in D) increases the negative volume charge density. The potential then transitions to a more negative value within a few Debye lengths of the surface charge σ_1. Noting that $C_0 = 0.1M$ is approximately equal to $(\frac{\rho_{volume}}{F})$, the counter- and co-ion concentrations within the brush layer (Fig. 3-4b), calculated from the potential using equations 3.11 and 3.12, are never equal to $C_0 = 0.1M$. In this region, the fixed volume charge density of the brush causes an increase in counter-ion (c_+) concentration and a decrease in co-ion (c_-) concentration, which is consistent with the macroscopic Donnan equilibrium ion partitioning that would be expected within the bulk of a uniform volume charge density in equilibrium with an electrolyte bath.[28, 49] Fig. 3-4 highlights the effect of separation distance D on the potential and ion concentration profiles at $C_0 = 0.1M$. In contrast, Fig. 3-5 shows the effect of varying C_0 on Φ, c_-

and c_+, plotted as a function of position z between and normal to the surfaces for $D = 30nm$. When ($|\frac{\rho_{volume}}{F}| << C0$), e.g., the case of $C_0 = 1.0M$ in Fig. 3-5, the fixed charge groups in the brush are effectively screened by the abundant counter-ion concentration. Therefore, Φ in the brush layer is nearly equal to the zero bath reference potential, and the counter and co-ion concentrations in the brush are nearly equal to $C0 = 1M$. In this case, ρ_{volume} has a negligible effect on ion partitioning. In the opposite limit, when $|\frac{\rho_{volume}}{F}| >> C_0$ (e.g., $0.01M$ when the volume charge density in the brush layer is much greater than the bath NaCl concentration), Φ is substantially more negative in the negatively charged brush layer (Fig. 3-5a), the counter-ion (Na^+) concentration is approximately equal to $|\frac{\rho_{volume}}{F}|$ ($0.1M$, Fig. 3-5b), and the co-ions are largely excluded from the brush, consistent with Donnan exclusion of co-ions (Fig. 3-5c, $[Cl^-] \approx 0.001M \approx (|\frac{\rho_{volume}}{F}|^2/[Na^+])$. While the counter-ion concentration is much higher within the brush than in the bath, long-range electrostatic forces beyond the brush (between the brush and tip) will still exist as long as there is some degree of interaction (overlap) between the tails of the potential profile between tip and brush. The potential profile $0.01M$ bath NaCl (Fig. 3-5a) shows that there is a significant interaction overlap even at $D = 30nm$ (i.e., the potential never decays to the zero reference value between $z = 20nm$ and $z = 30nm$), which results in a long-range repulsive force.

3.5.3 Charged Rod Model

The potential above, between, and within the cylindrical rods of finite height having fixed uniform volume charge density is shown in two dimensional cross-section in Fig. 3-6 for varying rod radii, w, in the range $1nm$ to $3.67nm$, and varying bath NaCl concentrations in the range 0.01 to $1M$. All other parameters representing the polyelectrolyte brush molecules and upper surface charge density are kept constant ($h = 25nm$, total rod charge $Q = -8.00 * 10^{-18}\ C$, and $\sigma_1 = -0.015\ C/m^2$). The variation of the potential profile for these conditions demonstrates how the nonuniform distribution of charge in the brush layer may affect both intra- and inter-rod electrostatic interactions. At a rod radius of $1nm$ (Fig. 3-6a), ($1nm$ at $0.1M$ NaCl) is

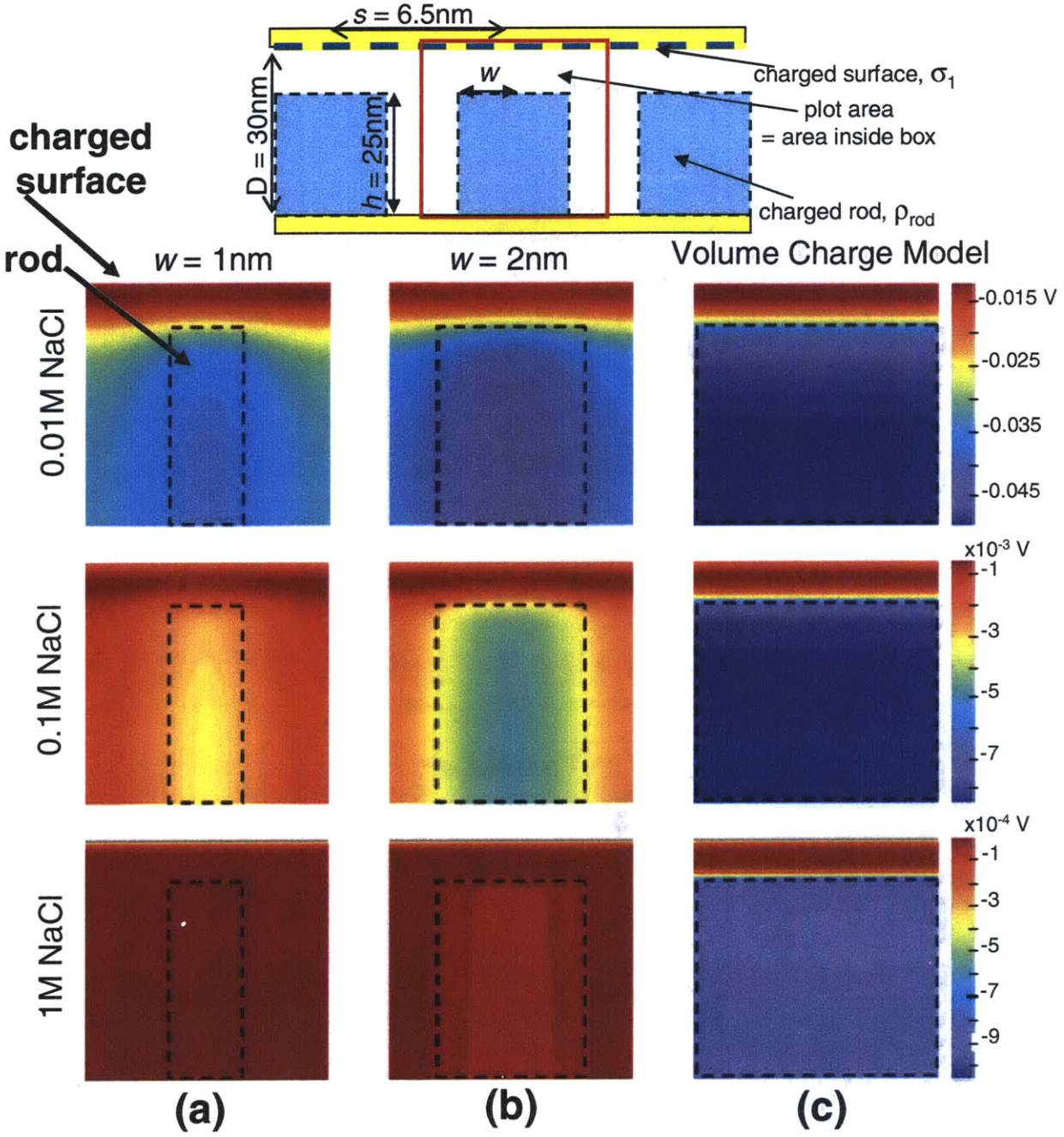

Figure 3-6: 2D potential distribution maps at a separation distance of $30nm$ at different ionic strengths for a brush height, $h = 25nm$, and various rod radii, w. The spacing between rods, s, was $6.5nm$, $\sigma_1 = -0.015\frac{C}{m^2}$ and the total charge of the rod was constant $Q_{rod} = -8 \times 10^{-18}C$.

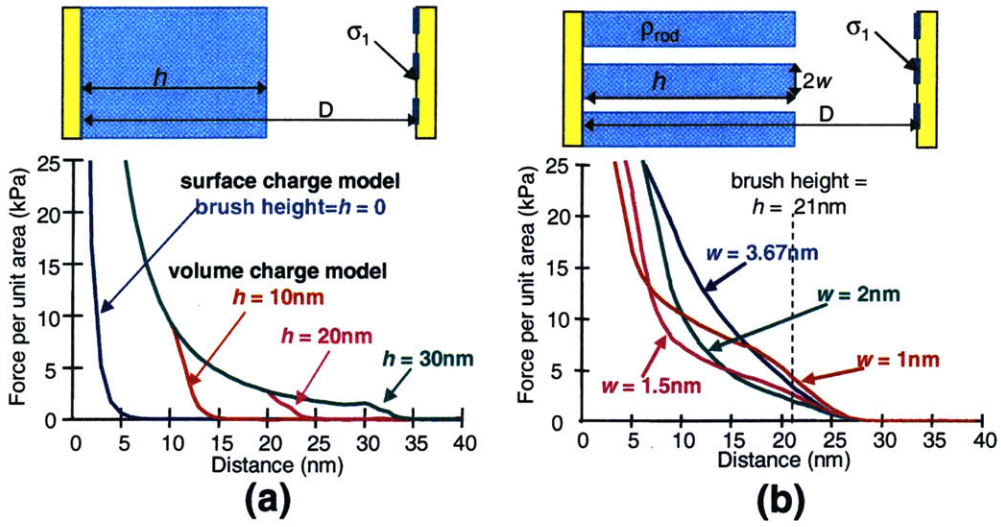

Figure 3-7: Simulation results of force per unit area (kPa) versus distance (nm) showing the effect of varying model parameters at 0.1M NaCl: (a) Effect of varying the brush height, h, at constant radius, $w = 3.67nm$ (volume charge model) and (b) Effect of varying rod radius, w, at constant height, $h = 21nm$.

smaller than the spacing between the edges of two adjacent rods ($5.5nm$). Therefore, the potential distributions of two such adjacent rods will not significantly overlap (i.e., the potential between rods approaches the zero reference potential) and there will be little electrostatic repulsion interaction between rods. In contrast, at rod radii of $2 - 3nm$ ($0.1M$ NaCl), or at $0.01M$ NaCl even for thinner rod radii, there is significant interaction of the potential tails, and a significant repulsion force can be expected. At a rod radius greater than $3.67nm$, which is the limit of the volume charge model, the magnitude of the potential is larger everywhere and is uniform. However, the volume charge density is smaller and, therefore, the total force may be equal or less than that predicted using thinner rods (see Fig. 3-7). Thus, the various ionic strength and rod radii in Fig. 3-6 exhibit a range of force interactions that will be compared with the predictions of the surface and volume charge models below.

3.6 Comparison of Model Predictions of Electrostatic Force between Surfaces

From equations 3.13 and 3.14 above, the potential profile can be used to calculate the electrostatic repulsion force between the surfaces for each of the three models of Fig. 3-1a-f. Model predictions are compared with each other in Fig. 3-7. A noticeable discontinuity in the slope of the force versus distance curves occurs when the charged tip encounters the top of the brush volume charge (Fig. 3-7a). This is an intrinsic property of the volume charge model and was described previously by Ohshima.[71] For the parallel plate geometry of the volume charge model (Fig. 3-7a), the force at any separation distance smaller than h is independent of h since model geometry and fixed charge density, ρ'_{volume}, are independent of h in this regime ($\rho'_{volume} = \frac{\rho_{volume}}{D} = \frac{\sigma_{GAG}}{D}$). While keeping all other parameters constant, an increase in the initial brush height, h, will always increase the electrostatic force at separation distances greater than h (Fig. 3-7a) since, as the brush height increases, fixed charges from the volume will be closer to the charged tip. Not surprisingly, the flat surface charge model (a volume charge in the limit $h \rightarrow 0$) will always predict a smaller electrostatic force than volume or rod models that account in some way for the height of the polyelectrolyte brush (Fig. 3-7).

The discontinuity in the force versus distance curve of Fig. 3-7a is much less apparent in the rod model at $D = h$ (Fig. 3-7b), but does occur for smaller values of D when initially thin rods are forced to expand laterally by compression. When keeping the brush height constant, increasing the rod radius changes the shape of the force curve (Fig. 3-7b). As shown in Fig. 3-6, increases in rod radius will increase inter-rod electrostatic interactions; however, intra-rod interactions will decrease because the volume charge density decreases with increasing rod volume. In contrast, if the rod radius is small, the force due to intra-rod repulsion will be high because the charge density inside the rod is very high, but inter-rod repulsion will be small since the edges of the rods are further apart.

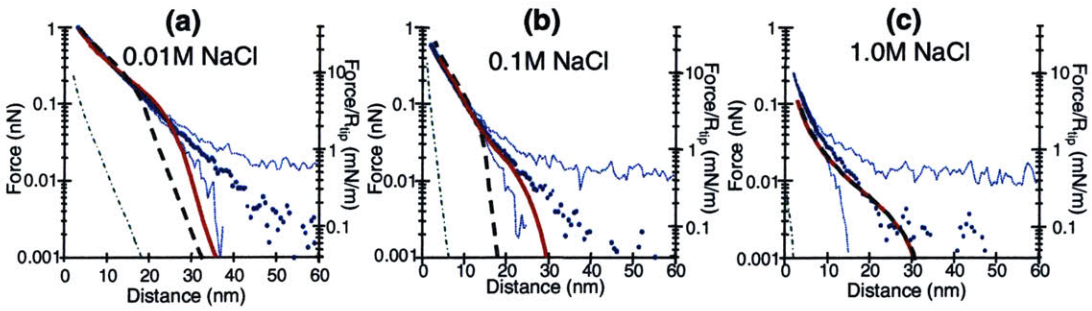

Figure 3-8: Comparison of best-fit charged rod (solid red line), volume (dashed black line), and surface charge models (dotted and dashed green line) to high-resolution force spectroscopy experimental data (blue dots, standard deviation = dotted blue line) of a sulfate functionalized probe tip versus end-grafted CS-GAG polymer brush at (a) IS = 0.01M NaCl: best-fit rod model parameters: $h = 25nm$, $w = 2nm$ and best-fit volume model parameter: $h = 18nm$, (b) IS = 0.1M NaCl: best-fit rod model parameters: $h = 25nm$, $w = 2nm$ and best-fit volume model parameter: $h = 14nm$, and (c) IS = 1M NaCl: best-fit rod model parameters: $h = 32nm$, $w = 3.67nm$ and best-fit volume model parameter: $h = 32nm$ (note: best-fit rod model = volume model). All other parameters were fixed: $s = 6.5nm$, $\rho_{volume}h = \sigma_2 = -0.19\frac{C}{m^2}$, $\sigma_1 = -0.015\frac{C}{m^2}$, and $R_{tip} = 25nm$.

3.7 Comparison of Model Predictions of Electrostatic Force to GAG Repulsive Force Data

To compare model force predictions to experimental data, the planar model geometry (Fig. 3-1a-c) was converted to a hemispherical tip geometry (Fig. 3-1d-f, see Appendix C). The best-fit model parameters are summarized in Table 3.7, and the

Models	Volume Charge Model	Charged Rod Model	
Parameters	volume height, h	rod height, h	rod radius, w
0.01M NaCl	$18nm$	$25nm$	$2nm$
0.1M NaCl	$14nm$	$25nm$	$2nm$
1.0M NaCl	$32nm$	$32nm$	$3.67nm$

Table 3.3: Best-fit values of model parameters at different bath ionic strengths.

surface charge model and best-fit curves for the volume and rod models are compared to data at different ionic strengths in Fig. 3-8. All three models predict a decrease in repulsive force with increasing ionic strength. As expected and previously discussed,[89] the flat surface charge model greatly underestimates the force. While the rod and volume charge models both predict a transition in the force versus distance curve at the top of the brush, a sharp transition was not observed in the data, although it has been reported[1] to varying degrees with other polyelectrolyte systems. This may be due to the relatively low grafting density of GAGs (0.024 chains/nm^2) compared to other systems in the literature (e.g. $0.13 - 0.41$ chains/nm^2[1]).

The brush height can be estimated from the experimental data (Fig. 3-8), since the electrostatic force begins at $D \sim 5\times$ from the top of the brush. At a bath NaCl concentration of $0.01M$, κ^{-1} is $\sim 3nm$. Therefore, since the measured experimental force starts at a tip substrate separation distance of $\sim 40nm$, the brush height should be $\sim 25nm$. Similarly, $\sim 1nm$ at $0.1M$ NaCl, and the measured force begins at $\sim 30nm$, so the brush height at $0.1M$ is also expected to be $\sim 25nm$. At $1.0M$ NaCl, $\sim 0.3nm$, and the measured force begins to increase at $\sim 20nm$; therefore, the estimated brush height at that ionic strength is $\sim 19nm$.

At $0.1M$ and $0.01M$ NaCl, the volume charge model predicts a much closer fit to the data than the surface charge model. However, the best-fit value of the brush height (the one adjustable parameter) is $14nm$ at $0.1M$ and $18nm$ at $0.01M$ (Table 3.7), which is $\sim$ 2-fold smaller than the known extended GAG length. These values do not appear to be well predicted by the volume charge model since they are small compared to the value of the brush height estimated from the force curves. However, this result may be expected since the GAG chains are about $6.5nm$ apart and the volume charge model assumes a uniform volume charge density. In distinct contrast, the rod model predicted a much better agreement with the force data for reasonable best-fit values of the brush height and rod radius at both $0.01M$ and $0.1MNaCl$ (Fig. 3-8a and b). The values for the brush height are consistent with the estimate from inspection of the force curve. This best-fit height suggests that the molecules are neither fully extended nor fully collapsed onto the surface. The best fit rod radius is

about four times larger than the known radius of the CS-GAG molecule.[63] However, the rods in the model represent the time average space occupied by the molecule and not the molecule itself and there are no previous measurements of this parameter for CS-GAG molecules in a brush. The best-fit value of w suggests that the CS-GAG molecules are not rigid but are undergoing random thermal motion within their tethered constraint.

The models presented here include only electrostatic (and not steric) forces. When electrostatic forces dominate (i.e., for ionic strengths = $0.1M$), the model is able to predict values for the brush height that are not significantly affected by the presence of steric forces, consistent with the assumptions of the models. However, at $1M$ salt concentration ($\kappa^{-1} \sim 0.3nm$), electrostatic forces are only on the order of steric interactions at tip-substrate separation distances smaller than the brush height. Therefore, by fitting the brush height of any purely electrostatic model to the total measured force in this high salt regime, the brush height is overestimated in order to compensate.

3.8 Extensions of the Charged Rod Model to Polyelectrolyte Brush-Brush Interactions

Experiments are currently underway to measure the force between two adjacent GAG brush layers[89] which is more representative of native cartilage. Fig. 3-9 shows two different extensions of the rod model to describe such brush-brush electrostatic interactions, one in which the brush layers exclude each and the other in which the brushes can interdigitate. There are differences in the predicted force between these two models, even though the total brush fixed charge is constrained to be the same in each. The compressed, non-interdigitating model predicts a force that is essentially a doubling of the force arising from a single brush. In contrast, the interdigitating model inherently incorporates more brush-brush repulsive forces since the rods from the two opposing brushes are interspersed 3-dimensionally and therefore exhibit

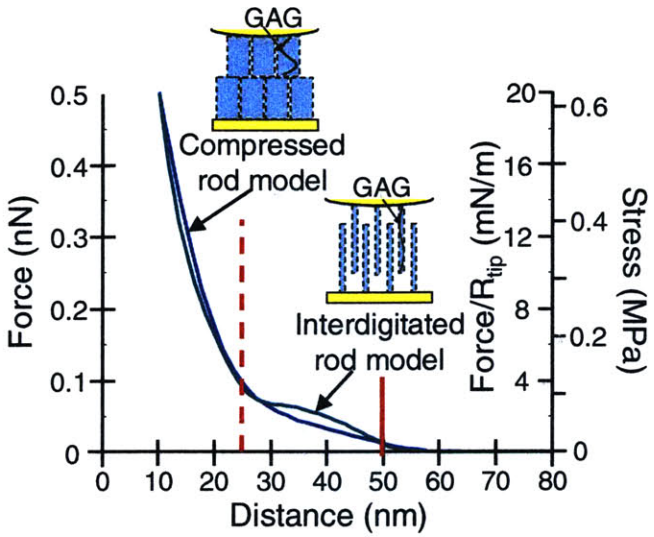

Figure 3-9: Comparison of two different models for polyelectrolyte brush-brush electrostatic force at 0.1M NaCl for an initial brush height, h, of $25nm$ and rod radius, w, of 2nm with a tip radius of $25nm$. In one model, the brush layers are allowed to interdigitate (green line) while in the the other the two brushes exclude each other (blue line). The read line indicates the distance ($50nm$) at which the two brushes just touch and the dashed red line indicates h (25nm).

increased electrostatic repulsive interactions in certain distance regimes. These differences in brush-brush electrostatic interactions can only be incorporated into models that include aspects of molecular-level structure (e.g., the volume and rod models). Currently, no theoretical model exists to describe the steric interactions between interdigitating surfaces of end-grafted rods. It is not currently known whether GAG molecules interdigitate within native cartilage tissue. Hopefully, a combination of HRFS measurements, AFM visualization, and theoretical modeling can help to determine how these molecules are arranged in tissues.

3.9 Relevance to Modeling Native Cartilage under Physiological Conditions

3.9.1 Steric Forces

In native cartilage (IS$\sim 0.15M$, synovial fluid pH~ 7.4, intra-cartilage pH$\sim 6.5-7$), aggrecan molecules are precompressed to occupy only $\sim$ 20% of the volume taken up under dilute solution conditions. Further compaction of aggrecan is caused by compressive strains as high as $15-30\%$ that may result from static joint loading under normal physiological conditions. As a result, the average separation distance between GAG chains in the tissue is $\sim 2-5nm$[11] and, hence, values of D in our HRFS experiments in the range $< 10nm$ are most relevant to modeling native cartilage. Given this dense packing, macromolecular steric repulsive forces between GAGs, $\mathrm{F}_{steric}(D)$, might also contribute to the total net osmotic swelling stress and compressive stiffness of cartilage. Steric forces may include configurational[65], mixing, and translational entropies, as well as enthalpic disruption of supramolecular structure (e.g., due to GAG-water hydrogen bonding).[70] The magnitude and range of steric forces depends on the conformation of the constituent GAG chains within tissue which is unknown (i.e., rigid rod versus random coil), their equilibrium position in space (i.e., in HRFS experiments, standing up versus lying down), and their molecular configuration during deformation (i.e., interdigitation versus compression).

In relating the present model to cartilage, additivity of steric and electrostatic forces may be assumed to a first approximation,[59, 65] knowing that both these components are dependent on solution environmental conditions (IS, pH) and, hence, interrelated to each other. Kovach[59] recently estimated the contributions of the configurational and mixing entropies of aggrecan-associated CS-GAGs to the equilibrium elasticity of cartilage and to the elasticity of solutions of aggrecan. These results were compared measurements of the corresponding macroscopic properties of aggrecan and cartilage. Kovach demonstrated that in $1.5M$ salt, the conformational contribution to the swelling pressure of CS-GAGs was $\sim 30\%$, but at physiologic IS,

the contribution was only $\sim$ 10%. He thus concluded that the electrostatic repulsive contribution was the predominant factor in determining the equilibrium swelling pressure of cartilage under physiological conditions. Theoretical work on the translational entropy component of the steric interaction of an incoming particle with surface grafted rods[65] suggests that the repulsive force has a nonlinear form with decreasing D, and becomes significant for $D <$ brush height. To model this component of the force in HRFS experiments rigorously, one would need an independent experimental measurement of the brush height, for example by ellipsometry or neutron reflectivity. Currently, no theoretical model exists to describe the interaction between end-grafted interdigitating rods.

3.9.2 Hard-Wall Substrate in HRFS

In relating the configurations of Fig. 3-1 to the modeling cartilage, there is no equivalent in the tissue of the "hard wall" planar substrate. Hence, even though this model may be appropriate for HRFS, further extensions are needed for application to the deformation of native cartilage. However, changes in force due to changes in D (i.e., the derivative of the force versus D curve) may be a good predictor of the electrostatic contribution to cartilage elastic modulus; ongoing studies are aimed at testing this hypothesis.

3.9.3 Divalent Ions

In addition, cartilage interstitial fluid in vivo contains a small proportion of the divalent ion, calcium ($<$ 5%),[63] which can easily be incorporated into the model via equation 3.8 and will only cause a small decrease in the predicted electrostatic force ($\sim$ 1%) using the PB formulation. While the presence of multivalent counter-ions has been reported to induce attractive interactions between like-charged polyelectrolyte chains such as DNA under specialized conditions,[43] this has not been observed for cartilage under physiological buffer conditions.

3.9.4 Charge Sequence Along GAG Backbone

GAGs are known to have charge heterogeneity in type of functional group and local charge density[75] that may affect both steric and electrostatic interactions at the atomic level. While this is not taken into account directly in our models, molecular dynamics models at the atomic level may be able to determine the importance of this phenomenon.[4]

3.10 Conclusions

We have compared three models for the electrostatic interaction forces within a polyelectrolyte brush layer. The rod model has been shown to be a feasible alternative to the simpler models previously discussed in the literature. Although the total polyelectrolyte charge was the same in all three models, both the rod and volume charge models, which accounted for the height of brush, predicted much higher forces than the surface charge model at any given separation distance. The comparison between measured and theoretically predicted forces in Fig. 3-8 shows that rod model gives better agreement with the force data over the widest range of separation distance D and for reasonable best-fit values of the brush height and rod radius. Changes in the rod radius led to changes in the shape of the predicted force profile. Therefore, in the framework of the PB theory, it appears that molecular level changes in the charge distribution inside polyelectrolyte brush layers as manifested in the rod model can significantly change the magnitude and the shape of the resulting force profile. Although the rod model is more general, it is also significantly more computationally intensive than the other two models. In certain experimental regimes, the volume charge model may be sufficient (e.g., for example, when the polyelectrolyte molecules are less than κ^{-1} apart). Future work includes comparing the predictions of these models to more complex experimental systems (such as the ongoing GAG brush-brush interaction experiments described above) and to the predictions of atomic level models of GAGs and GAG-GAG interactions.[4]

Chapter 4

Measurement of Conformation of an Aggrecan Brush Layer

This chapter was submitted as Communication to Macromolecules in the fall of 2004.[22]

4.1 Introduction

The nanomechanical behavior of cartilage matrix macromolecules has received increasing attention[61, 88, 93, 94] since matrix degradation causes loss of tissue and joint function with age and arthritis. For example, loss of aggrecan and its highly charged glycosaminoglycan (GAG) polymer chains (Figure 4.2) significantly reduces cartilage's compressive stiffness. The nanoscale force between opposing GAG brushes (a system that mimics local molecular responses to tissue deformations) has been measured over a broad range of pH and ionic strength (IS) solution conditions[88] and was well described by a Poisson-Boltzmann-based, electrostatic double layer (EDL) "charged rod" model[24] (see Chapter 3). *In vivo*, however, GAGs are covalently linked to a core protein of *aggrecan* in a very dense "bottle-brush" morphology, motivating the need to study the stiffness of native aggrecan in a closer-to-physiological model system. Here, we probe the conformation and compressibility of an aggrecan-functionalized surface as a function of aqueous bath conditions and normal compres-

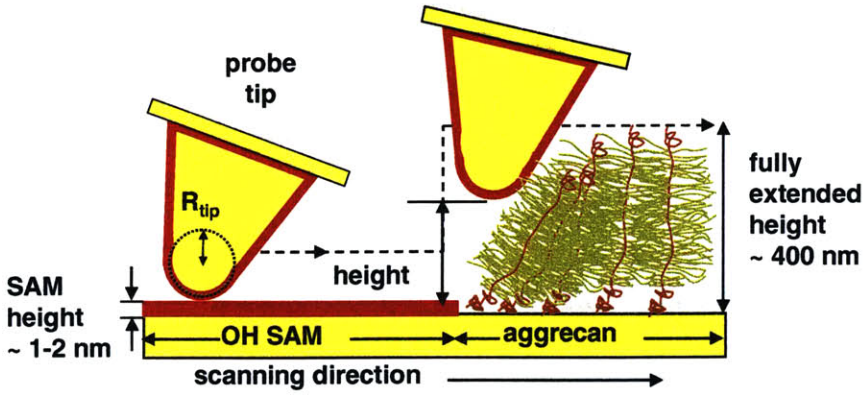

Figure 4-1: Illustration of AFM contact mode imaging on aggrecan and hydroxyl-terminated SAM patterned surface ($R_{tip} \sim 50nm$, aggrecan monomers $\sim 19nm$ apart, contour length $\sim 400nm$, side chain (mostly CS-GAG) contour length $\sim 40nm$, side chains $\sim 2 - 4nm$ apart).

sive load by combining the techniques of micro-contact printing (μCP[103, 7]) and atomic force microscopy (AFM) in fluid (Figure 4.2). μCP enabled the creation of a patterned surface with densely packed, chemically end-grafted aggrecan confined to well-defined micrometer-sized areas and a hydroxyl-terminated self-assembling monolayer (OH-SAM) confined to the rest of the area. Using contact-mode AFM imaging over boundaries between aggrecan and OH-SAM regions, the height and, hence, the deformation of the aggrecan was directly measured as a function of applied compressive load, IS, and pH.

4.2 Experimental Section

Fetal bovine aggrecan[68] ($0.5mg/ml$) was solubilized in de-ionized (DI) water with 1μM dithiobis(sulfosuccinimidyl propionate) (DTSSP, Pierce #21578). DTSSP reacts with the amines at the N-terminal and lysines of the core protein to form disulfide bonds. Lysines are mostly found at the ends of the core protein (see Appendix G) of the core protein. These disulfides were reduced to thiols by reacting with dithiothreitol (DTT, Pierce #150460) in 0.1mM aqueous solution for 1 hour. Excess reactants were removed by spinning at 3500 rpm overnight with a centrifugal filter (Centricon, Millipore, 10 kDa cutoff). OH-aggrecan patterned substrates were made by

μCP[103] of 4mM 11-mercaptoundecanol, $HS(CH_2)_{11}OH$, (Aldrich) in ethanol on a freshly cleaned $1cm \times 1cm$ gold-coated substrate[89] for 30 seconds using a hexagonal patterned polydimethylsiloxane (PDMS) stamp (hexagon side length = $15\mu m$ and spacing = $15\mu m$) followed by incubation in $50\mu L$ of $1mg/ml$ thiol-terminated aggrecan solution for 48 hours. Hence, the aggrecan was located within the hexagons and the OH-SAM outside the hexagons. OH-functionalized AFM gold coated probe tips (Digital Instruments, $k \sim 0.06N/m$, tip radius $\sim 50nm$) were prepared by immersion in 4mM 11-mercaptoundecanol for 48 hours to minimize electrostatic interactions between the probe tip and aggrecan layer.

Aggrecan height in aqueous solution was measured as the relative height between the OH-SAM (negligible thickness $\sim 1-2nm$) and aggrecan (Figure 4.2) regions under different compressive normal forces using a Multimode Nanoscope IV AFM (Digital Instruments) in contact mode in fluid at a scanning frequency of 1Hz. Solutions were: 0.001M-1M NaCl in MilliQ water (pH $\sim$ 5.6) and 0.01M phosphate buffered saline (PBS) at pH = 3, 7, and 10, and 0.154M PBS at pH = 7.4. After AFM experiments were completed, aggrecan grafting density on the surface was assessed by removal of the aggrecan via boiling the substrate in DI water for 60 min. The residual solution was lyophilized and re-dissolved in $50\mu l$ DI water. A dimethylmethylene blue (DMMB) dye binding assay[32] yielded a total aggrecan density equivalent to $\sim 2,590 \pm 90$ aggrecan molecules per $1\mu m \times 1\mu m$ surface area, or one aggrecan molecule per $\sim 19nm \times 19nm$. The CS-GAGs from this fetal bovine aggrecan have contour lengths of $\sim 40nm$;[68] therefore, GAGs from adjacent aggrecans will likely interpenetrate at these high grafting densities and bath conditions.

4.3 Results and Discussion

Aggrecan height was found to be non-hysteretic (independent of loading history) and decreased markedly with increasing IS from 0.001M-1M at constant force (Figure 4.3), and with increasing normal force at constant IS (Figure 4.3). The maximum height, $\sim 310nm$ in 0.001M NaCl and $\sim 0nN$ normal force, was $\sim$ 78% of the known contour

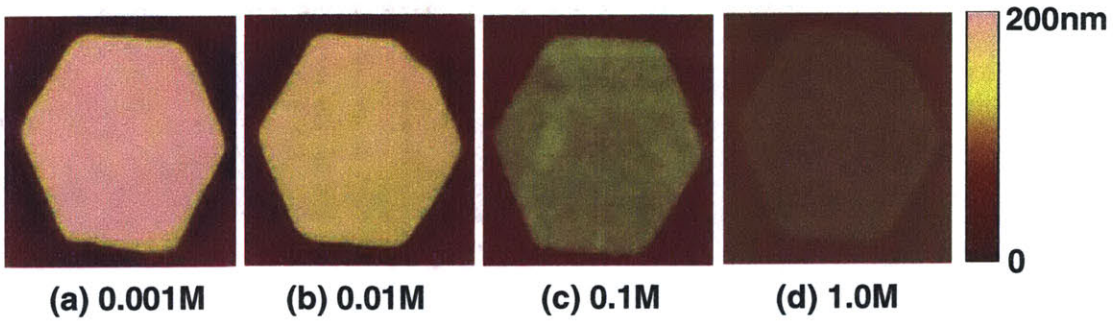

Figure 4-2: AFM contact mode height images of μCP surfaces with aggrecan inside and a hydroxyl-terminated SAM outside the hexagons ($20\mu m$ scan; $3nN$ applied normal force) at different ionic strengths (0.001M-1M NaCl).

length of the aggrecan used ($400nm \pm 60nm$).[68] The strong dependence of aggrecan height on IS indicates that electrostatic interactions are a critical determinant of the nanomechanical behavior of aggrecan. The carboxyl and sulfate groups on the CS-GAG are ionized at all bath pH and IS of Figure 4.3.[89] The electrostatic interaction distance in monovalent electrolyte solutions is determined by Debye length, $\kappa^{-1} = \sqrt{\frac{\epsilon_w RT}{2F^2 C_0}}$ (where ϵ_w is the permittivity ($6.92 \cdot 10^{-10} C/Nm^2$), F the Faraday constant ($96,500 C/mole$), R the universal gas constant, T the absolute temperature (298K), and C_0 the bath IS). At low IS ($<$ 0.1M NaCl), κ^{-1} is greater than the spacing between GAG chains on aggrecan ($\sim 2-4nm$), resulting in large electrostatic repulsion forces between neighboring and adjacent GAG chains. These forces facilitate extension of the aggrecan monomers from the gold substrate, giving an uncompressed aggrecan height that is close to the contour length of aggrecan. As the IS is increased, electrostatic repulsion forces are shielded and the height of the aggrecan decreases. At 1M NaCl, κ^{-1} ($\sim 0.3nm$) is roughly 1/10 the distance between CS-GAG chains and, therefore, much of the inter-chain electrostatic repulsion has been screened. The resulting uncompressed height of the aggrecan brush ($\sim 100nm$) is determined mostly by steric effects from the close packing of the aggrecan monomers, as well as some intra-chain electrostatic repulsion along the CS-GAGs (with κ^{-1} about $2\times$ the spacing between charge groups along the chain). For all bath IS, there was an initial steep decrease in height with increasing normal force followed by a plateauing

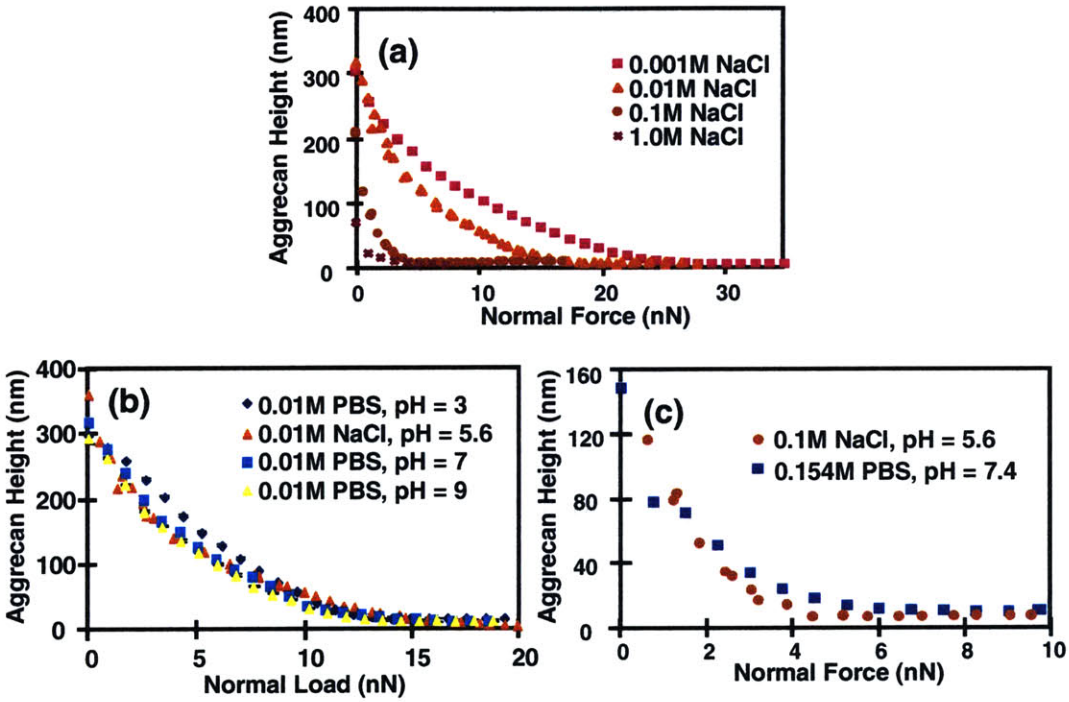

Figure 4-3: Aggrecan height as a function of normal force and ionic strengths: (a) 0.001M-1.0M NaCl, pH = 5.6, (b) 0.01M NaCl, pH = 5.6 and 0.01M phosphate buffered saline (PBS, pH = 3, 7, and 10, and (c) 0.154M, PBS, pH = 7.4 and 0.1M NaCl, pH = 5.6 (standard deviations were smaller than the size of data points).

of height at higher forces, corresponding to an "incompressible height." With decreasing IS, greater normal force was needed to this incompressible height. Although the initial height of the brush at $\sim$ 0 nN force changed greatly with ionic strength, the incompressible height at high normal force (> 30 nN) was $\sim 5nm$ for all IS conditions (Figure 4.3a). In 0.001M NaCl, the aggrecan brush appeared stiffest (i.e., the height versus normal force curve had the smallest slope) due to high electrostatic repulsion forces. Although aggrecan height at $\sim$ 0 nN was similar in 0.01M and 0.001M NaCl, the brush height decayed more steeply with increasing normal force in 0.01M NaCl. For IS > 0.01M, the brush became softer with increasing IS. By 1.0M NaCl, when the inter-GAG chain electrostatic interactions are almost completely shielded and non-electrostatic effects dominate, the brush height decayed rapidly with normal force, reaching its incompressible height at the relatively low force of $\sim$ 5nN. In this regime (0nN force at 1M NaCl), the height was difficult to measure, as small changes in the force used in the AFM imaging produce marked differences in the measured height.

Aggrecan height measured in 0.01M PBS at pH = 3, 7, and 10 was not significantly different from the height in 0.01M NaCl at pH= 5.6 for all normal forces used (Figure 4.3b). Furthermore, aggrecan height in physiological conditions (0.154M PBS at pH = 7.4) was not significantly different from the height in 0.1M NaCl at pH= 5.6 (Figure 4.3c). Although the degree of protonation of carboxyl groups at pH 3 is different from that at pH 7,[39] the sulfate groups would not be significantly affected.[60] Even at pH =3, when the total aggrecan fixed charge is about half that at pH 7, there are still very strong GAG-GAG electrostatic repulsion forces at 0.01M IS from the sulfate groups alone that cause the brush to have the same height. This is consistent with the observation that $\kappa^{-1}(0.01M) \sim 3nm$ is on the order of the inter-GAG chain spacing along densely core proteins of the densely populated aggrecan brush. In contrast, the height of a sparsely populated CS-GAG brush (measured by ellipsometry)[88] was found previously to decrease from pH=5 to 3 at 0.01M IS. However, the GAG-GAG in that system ($6.5nm$) was $\sim 3-4\times$ greater than that within the aggrecan brush used here. Finally, the aggrecan height versus normal force behavior at 0.1M NaCl, pH 5.4 (Figure 4.3c) was similar to that under the physiologic buffer conditions

(IS=0.154M, pH 7.4). Importantly, in this experiment at $\sim$ 0nN force (Figure 4.3c), the measured density of aggrecan on the surface corresponds to $\sim 55mg/ml$, which is within the known range of aggrecan concentrations in normal articular cartilage under free swelling conditions $(20 - 80mg/ml)$.

The μCP-AFM method does have some limitations when used for measuring polymer brush heights at equilibrium or under zero normal force. First, since a small tare force of $\sim$ 200pN must be applied to the AFM tip when imaging, it can be difficult to measure the uncompressed height of extremely soft polymers by AFM at 0 nN normal force. Small changes in normal force used in imaging could produce significant differences in the measured height. Secondly, the resolution of this technique depends on the surface roughness of the substrate. For thinner (¡5nm) polymer layers, the gold substrate used here may be replaced by mica to achieve better resolution of small height differences between the inside and the outside of the patterned region. At the same time, this μCP-AFM method has several advantages for the measurement of polymer thicknesses compared to other approaches such as the "scratch method,"[105] ellipsometry,[98] neutron reflectivity,[98] etc. The μCP-AFM method offers a more defined chemical system and better resolution ($\sim nm$) than the often-used "scratch method,"[105] and provides a means to directly measure the polymer height in a variety of solvent conditions and under a range of normal forces. This is not possible with more conventional techniques such as ellipsometry.[6] By measuring the height under different applied normal forces, additional information can be gathered about the nanomechanical properties of the polymer layer.

In this study, the brush layer height and compressibility of aggrecan were observed simultaneously, which enables a direct estimate of the stiffness of the layer. Additionally, other mechanical properties can be investigated via μCP. By using a colloidal tip having a radius on the micrometer scale, the polymer layer can be sandwiched between surfaces with a much larger radius of curvature, resulting in a simpler boundary condition for measurement of mechanical moduli than that of a sharp pyramidal tip. Measurement of polymer height versus normal force can be also be combined with force-deflection curves obtained via using high resolution force spectroscopy, giving

a more complete description of the mechanical behavior of the layer at both small and large loads. Using lateral force microscopy, the shear behavior of polymer layers can be also be studied with brush height obtained simultaneously; chemically grafting of the polymer may offer advantages over physical attachment for investigating nanomechanical behavior.[82]

Chapter 5

Measurement and Modeling of Normal Interaction Forces between Opposing Aggrecan Brush Layers

5.1 Introduction

Aggrecan is the most abundant proteoglycan in the cartilage extracellular matrix. It is a large macromolecule (contour length, $L_c \sim 400nm$) composed of $\sim$ 100 glycosaminoglycan (GAG) side chains ($L_c \sim 40nm$) that are attached covalently to a core protein ($\sim 300kDa$) in a cylindrical "brush"-like configuration. These GAG chains are highly charged due to the sulfate and carboxyl groups that are ionized under physiological conditions. The aggrecan molecules self-assemble non-covalently with their end domains attached along hyaluronan backbone thus forming large "brush"-like aggregates ($> 200MDa$).[63] From macroscopic tissue level experiment, it is thought that this high charge and packing is responsible for $50 - 75\%$ of the equilibrium elastic modulus of cartilage in compression.[63, 11] However, it is not yet well understood how structural changes (such as those due to age and disease) directly effect the nanomechanical properties of the molecules themselves or how the changes in molecular mechanics effect the bulk cartilage tissue mechanical properties.

Recently, we measured forces between end-grafted chondroitin sulfate GAG brushes.[88] These were compared to a Poisson-Boltzmann theoretical model that describes normal electrostatic double layer interaction forces between two opposing surfaces of end-grafted cylindrical rods.[24] This model was then used to theoretically increase the density of GAGs to that found in tissue. This resulting theoretical GAG brush stiffness was compared with ankle cartilage in uniaxial compression and was found to be $\sim 50\%$ of the tissue modulus. We also measured the height of and end-grafted aggrecan "brush"-like layer on gold using contact mode atomic force microscopy (AFM) on micro-patterned substrates as a function of solvent conditions (ionic strength 0.001M-1M NaCl and pH $\sim 3-7$) and normal compressive force applied during imaging ($\sim 0-40nN$) (see Chapter 4).[22] We found that that the height of the aggrecan height at near $0nN$ decreased with increasing ionic strength and that the force needed to reach an incompressible height decreased with increasing ionic strength ($\sim 30nN$ at 0.001M to $\sim 3nN$ at 1M NaCl). This indicated that the aggrecan layer was softer at higher ionic strengths and that electrostatic forces are important not only to GAG brush interaction forces but also to whole aggrecan interactions.

The goal of this project was first to quantify directly the molecular interaction forces between whole aggrecan macromolecules in compression at near physiological conditions and then to assess the role of these interactions in whole cartilage tissue. Aggrecan molecules purified from fetal bovine epiphyseal cartilage were chemically end-grafted at physiologically relevant densities ($\sim 55mg/ml$) to substrates, standard AFM nano-sized probe tips, and large micron-sized colloidal probe tips using the method described in Chapter 4.[22] Then, the nanoscale normal forces were measured as a function of separation distance in various ionic strength aqueous solutions (pH ~ 5.6). These forces and distance ranges measured between the aggrecan brush layer on the substrate and the aggrecan on the standard AFM nano-sized probe tip ($\sim 2-4$ aggrecan on the tip interact with the substrate) were found to be significantly larger ($\sim 50\times$ larger force and $\sim 6\times$ larger distance range at 0.1M NaCl) than those previously measured between opposing GAG-only brush coated on substrates and similar sized tips.[88] The force-distance data between two interacting aggrecan

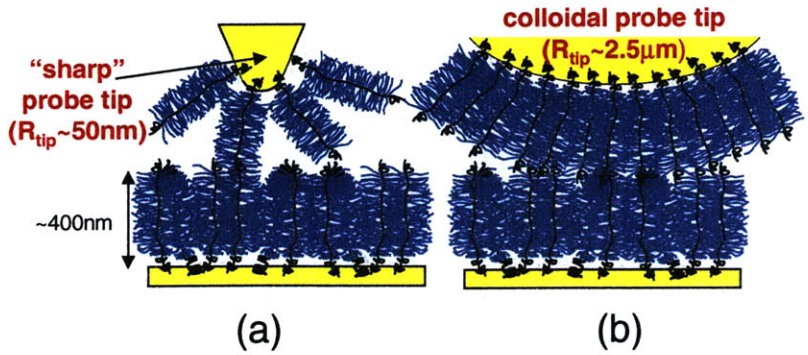

Figure 5-1: (a) Nano-sized ($R_{tip} \sim 50nm$) (b) Micron-sized ($R_{tip} = 2.5\mu m$) probe tips with end-grafted aggrecan brush layers (core protein $\sim 19nm$ apart, contour length $\sim 400nm$, side chain (mostly CS-GAG) contour length $\sim 40nm$, side chains $\sim 2-4nm$ apart).

brushes measured a substrate and large colloidal tip coated with aggrecan (since $R_{tip} = 2.5\mu m$, $\sim$ 1000s of aggrecan on the tip and substrate interact in this geometry) were then converted to nanoscale stress-strain curves and an effective stiffness of the aggrecan brushes was calculated. These values were compared to 3 different Poisson-Boltzmann based models of electrostatics: the smooth volume of charge,[71, 28, 62] the unit cell that models the GAG and its surrounding mobile ions as a cylindrical unit cell,[62, 58, 11] and the charged rod model that models the time-averaged space occupied by a GAG chain as a cylindrical volume charge density.[24] The rod model[24] was found to represent the data closely over a large strain range (0–0.4) although none of the models were able to predict the stress at high strains. The aggrecan nano-scale stress-strain curve was also found to match well with previously reported macroscopic measurements[8, 85] from tissues similar to bovine epiphyseal cartilage from which this aggrecan was purified.

5.2 Experimental Methods

Purified fetal bovine epiphyseal aggrecan[68] was end grafted (Figure 5-1) to gold coated nano-sized AFM probe tips ("sharp probe tip", Digital Instruments, $k \sim 0.06N/m$, tip radius $R_{tip} \sim 50nm$), gold coated micron-sized silica colloidal probe tips

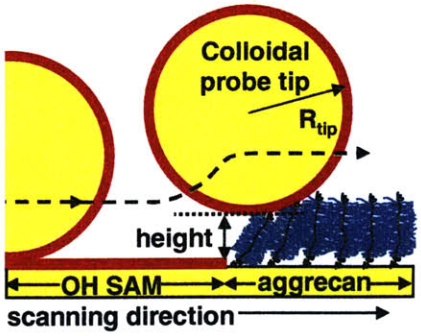

Figure 5-2: Schematic of the colloidal tip ($R_{tip} = 2.5\mu m$) imaging the height of an aggrecan brush layer on the substrate (not drawn to scale).

("colloidal tip", BioForce Nanosciences, $k \sim 0.12N/m$, $R_{tip} = 2.5\mu m$), and $1cm \times 1cm$ gold-coated substrates[89] (Figure 5-1) as described previously (see Chapter 4).[22] Since the colloidal tip is much larger ($R_{tip} = 2.5\mu m$) than spacing between individual aggrecan molecules ($\sim 20nm$), the larger colloidal probe tip was used in order to measure the forces between two approaching aggrecan brush layers. For control OH-functionalized substrates and probe tips were prepared by immersion in 4mM 11-mercaptoundecanol (Aldrich) in ethanol for 48 hours.[22]

In order to properly offset the x-axis of the force-distance curves by the incompressible layer,[22] the height of the aggrecan layer was measured using the same probe tips used for the nanomechanical measurements (see Figure 5-2) following the protocol described in Chapter 4. Aggrecan was patterned onto substrates such that aggrecan was inside a hexagonal pattern and an OH self assembled monolayer (OH-SAM) was on the outside using the technique of micro-contact printing (see Figure 5-5).

The normal force between the functionalized probe tips and surfaces were measured using a 1D Molecular Force Probe (MFP, Asylum Research) for the "sharp" tip and a Multimode Nanoscope IV AFM (Digital Instruments, Veeco) for the "colloidal" tip in aqueous solution at a z-piezo rate of $1\mu m/sec$ (surface dwell time = $0sec$). Solutions were 0.001M-1M NaCl in MilliQ water (pH $\sim$ 5.6). After nanomechanical experiments were completed, aggrecan grafting density on the surface was assessed by removal of the aggrecan via boiling the substrate in dionized (DI) water

for 60 min. The residual solution was lyophilized and re-dissolved in $50\mu l$ DI water. A dimethylmethylene blue (DMMB) dye binding assay[32] yielded a total aggrecan density equivalent to $\sim 2,590 \pm 90$ aggrecan molecules per $1\mu m \times 1\mu m$ surface area, or one aggrecan molecule per $\sim 19nm \times 19nm$ (see Appendix G for more details).

In order to compare nanomechanical data to whole tissue measurements, the average force versus distance curve and the brush height versus normal force from the aggrecan-functionalized colloidal probe tip (Figure 5-1b) versus the aggrecan substrate at 0.1M NaCl (near physiological conditions) were combined to form a composite curve and this was then converted to stress versus strain using the following equations:

$$\text{Stress} = \frac{\text{Force}}{\text{Tip-substrate interaction area}} \tag{5.1}$$

$$\text{Strain} = 1 - \frac{\text{Distance}}{\text{Uncompressed brush height}} \tag{5.2}$$

For more details of how the tip-substrate interaction area was calculated, see Appendix F.[84]

5.3 Results

5.3.1 Interaction forces between standard "sharp" probe tips and aggrecan brush substrates

The height of the aggrecan layer decreased with increasing bath ionic strength and normal force used during the constant normal force applied during contact mode imaging as previously reported (see Chapter 4).[22] The normal forces between the functionalized nano-sized probe tips and the aggrecan brush substrate decreased with increasing ionic strength (Figure 5-3). The height of the layer measured using the "sharp" aggrecan probe was not significantly different from that measured using the "sharp" control OH-SAM probe (see Chapter 4).[22] The forces measured with the "sharp" aggrecan probe tip (Figure 5-3b) were also larger in magnitude and range

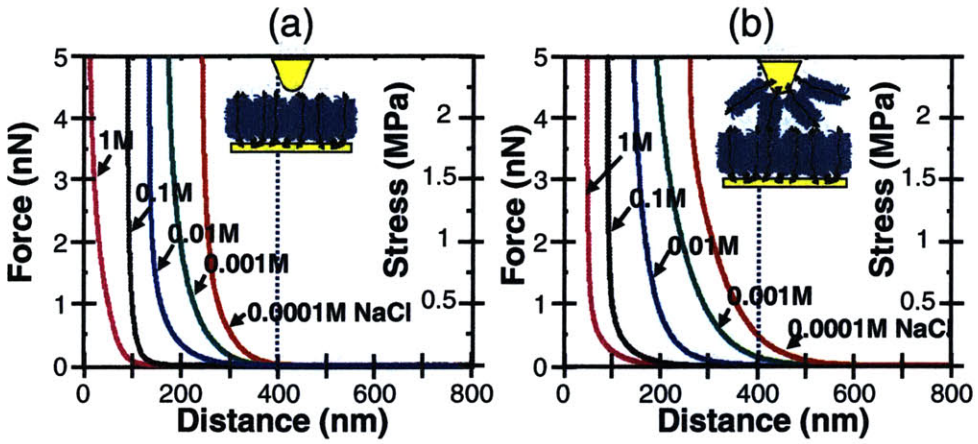

Figure 5-3: Normal force and stress between (a) a neutral OH-SAM functionalized "sharp" probe tip ($R_{tip} \sim 50nm$) and (b) an aggrecan-functionalized "sharp" probe tip ($R_{tip} \sim 50nm$) and an aggrecan brush on a planar substrate at different bath salt concentrations (0.0001M-1M NaCl, $pH \sim 5.6$) as a function of separation distance between the tip and substrate. The vertical blue dotted line represents the aggrecan contour length $\sim 400nm$. Standard deviations are smaller than the thickness of the curves.

than those measured with the "sharp" neutral OH-SAM coated tip (Figure 5-3a). This difference was especially noticeable at the lower ionic strengths (0.001M and 0.01M NaCl) and decreased with increasing ionic strength. Since the radius of the "sharp" probe tip is $\sim 50nm$ and the spacing between aggrecan molecules is $\sim 20nm$, only a few aggrecan molecules on the tip can interact with the aggrecan brush on the substrate (see Figure 5-4 black line and dashed grey line).

The normal forces between the neutral probe tip and the aggrecan brush layer were $\sim 10\times$ larger than those measured between a similar tip and an aggrecan monolayer covalently attached to an amine surface (see Appendix H)[23] and $\sim 50\times$ larger than those previously measured between a similar tip and a GAG end-grafted brush (Figure 5-4).[90] The forces between aggrecan brushes were even larger and longer ranged than the forces between two end-grafted GAG brushes.[88]

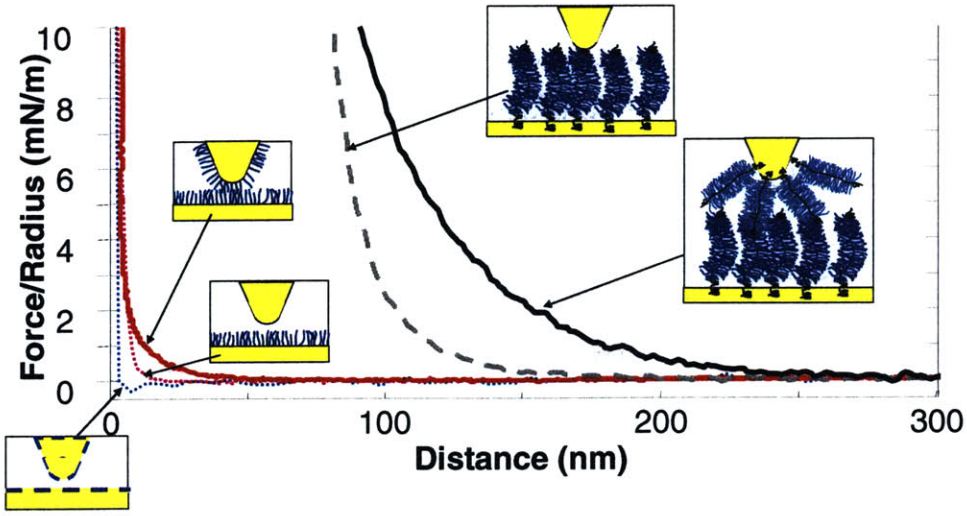

Figure 5-4: Comparison of force normalized by probe tip radius between an aggrecan-coated "sharp" probe tip ($R_{tip} \sim 50nm$) and the aggrecan brush substrate (solid black line), a neutral OH-SAM coated "sharp" probe tip ($R_{tip} \sim 50nm$) and an aggrecan brush substrate (grey dashed line), a glycosaminoglycan (GAG) brush coated probe tip ($R_{tip} \sim 48.5nm$) and a GAG brush substrate (solid red line),[88] a neutral OH-SAM probe tip ($R_{tip} \sim 127nm$) and a glycosaminoglycan brush substrate (magenta squares),[90] and a negatively charged sulfate-functionalized monolayer coated tip and surface (blue dotted line)[89] at 0.1M NaCl (pH$\sim$ 5.6). Standard deviation was $\sim 0.06mN/m$.

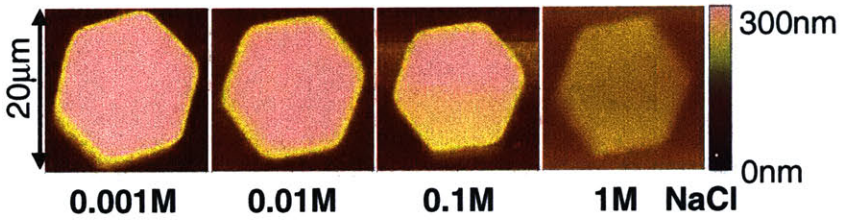

Figure 5-5: Height images of the aggrecan "brush" inside the hexagonal pattern measured with the neutral OH SAM-functionalized colloidal tip in different ionic strengths (0.001M-1M NaCl, $pH \sim 5.6$) at 3nN normal force.

5.3.2 Aggrecan brush height measured with colloidal probe tips

The aggrecan brush height measured with the functionalized micron-sized colloidal probe tips decreased with increasing ionic strength (Figure 5-5) and normal force (Figure 5-6). The height was observed to decrease much more slowly with normal force than when measured with the standard "sharp" probe tip (see Chapter 4 Figure 4.3a).[22] This is not unexpected as the applied force per unit area (stress) is much larger ($\sim$ 3000$\times$) with the sharper tip than with the large colloid. The measured height of the aggrecan brush layer was smaller when it was measured with a colloidal tip coated with aggrecan (Figure 5-6b) than when it was measured with a neutral OH-SAM coated colloid (Figure 5-6a). The measured height from the images (Figure 5-5) is the height of the inside of the pattern minus the height outside pattern. So in the case when the aggrecan coated colloidal tip is used for imaging (Figure 5-6b), the measured height of the pattern in the image (see schematic in Figure 5-6b) is the height of 2 aggrecan layers (one on the tip and one on the substrate) minus the height of 1 aggrecan layer (one on the tip since the substrate outside the pattern has no aggrecan). Therefore, in the aggrecan coated tip experiment, the real distance between the tip surface and the substrate surface (see schematic inset in Figure 5-7) is the sum of the height measured by the neutral colloid tip (Figure 5-6a) and the measured image height by the aggrecan colloid (Figure 5-6b) if we assume that the aggrecan on the tip against the OH-SAM on the substrate compresses similarly to the aggrecan on the substrate against the OH-SAM coated neutral tip. From this, we can get the true thickness of the two brushes as they interact (see Figure 5-7). The actual height of two compressed aggrecan layers (Figure 5-7) is smaller than twice the height of one aggrecan layer (Figure 5-6a) compressed with the same amount of normal force for all ionic strength although it is only slightly smaller at 1M NaCl.

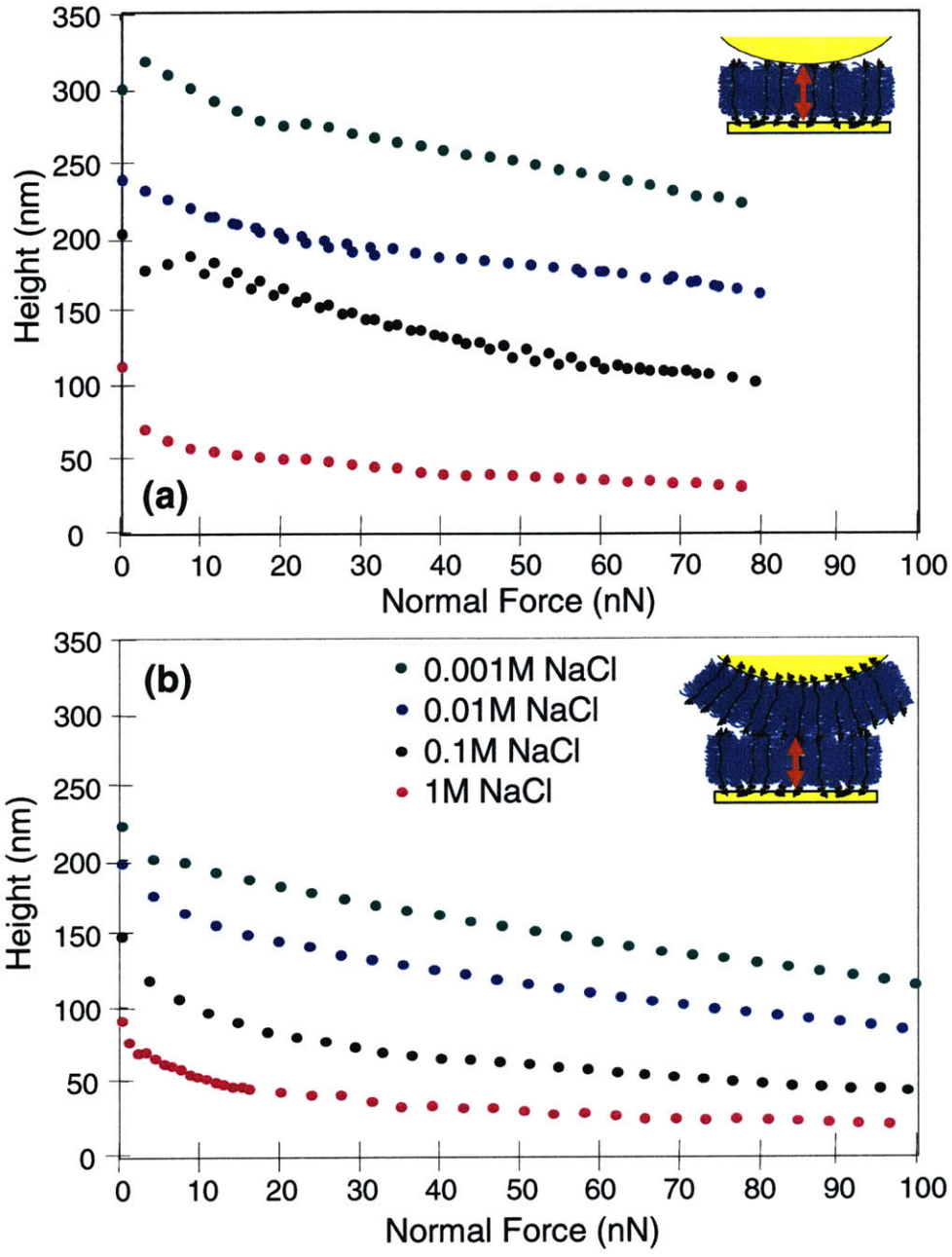

Figure 5-6: Height of the aggrecan brush as measured with contact mode AFM using (a) a neutral OH-SAM colloidal tip ($R_{tip} = 2.5\mu m$) and (b) an aggrecan coated colloidal tip ($R_{tip} = 2.5\mu m$) at different bath ionic strengths (0.001M-1M NaCl, $pH \sim 5.6$) and different normal forced used during imaging. Standard deviations are smaller than the data points. Schematic inset indicate which brush height is being measured.

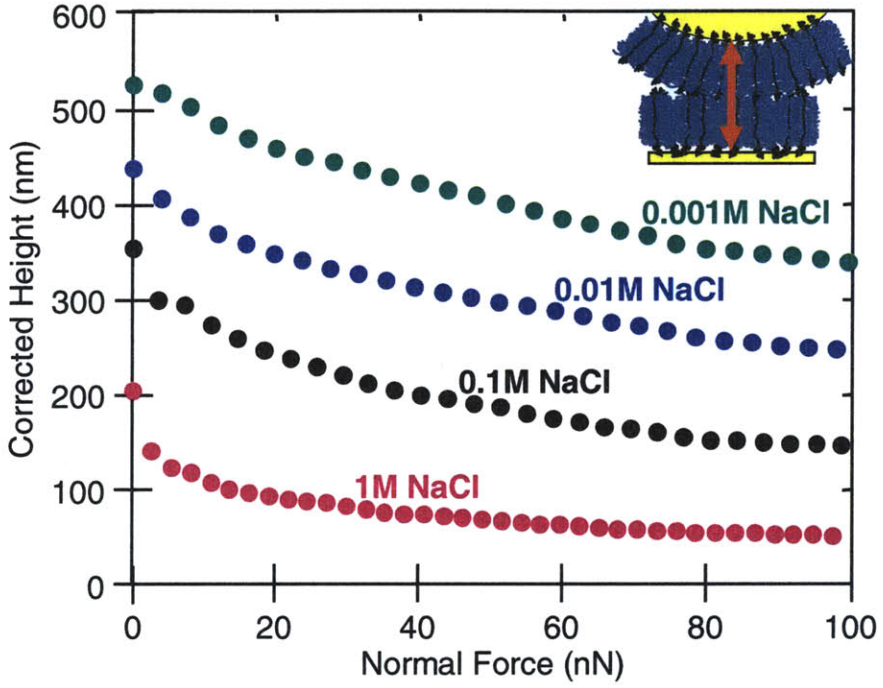

Figure 5-7: Total height difference between the aggrecan colloidal tip and the aggrecan pattern as shown in the schematic at different ionic strengths (0.001M-1M NaCl, $pH \sim 5.6$) and normal forces used during imaging. This is a composite of figures 5-6a and b. Standard deviations are smaller than the data points.

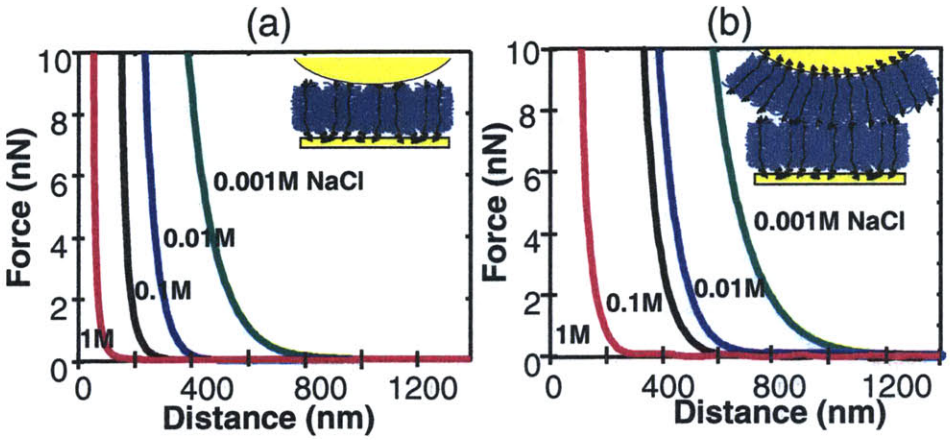

Figure 5-8: Average force between a) OH-SAM coated colloidal tip and b) aggrecan coated colloidal tip and an aggrecan substrate on approach in different bath ionic strengths (0.0001M-1M NaCl, $pH \sim 5.6$, $R_{tip} = 2.5\mu m$). Standard deviation is smaller than the thickness of the curves.

5.3.3 Forces between colloidal probe tips and aggrecan brush substrates

The normal forces with the micron-sized colloidal tip (Figure 5-8) show the same strong dependence on ionic strength as those measured with the "sharp" probe tip (Figure 5-3). Although the measured forces decay significantly with increasing ionic strength, long range forces are still observed at 1M NaCl. Since the tip radius in this experiment is much larger than the spacing between aggrecan monomers, there are $\sim 10,000$ aggrecan molecules on the aggrecan-coated tip that can interact with the aggrecans on the substrate. Therefore, this is measuring the forces between two approaching aggrecan brush layers. The forces measured between the aggrecan-coated tip and a OH-SAM coated control substrate were similar to those measured between the OH-SAM coated tip and the aggrecan brush sample.

Similar to the results when aggrecan was attached to the "sharp" tip, the measured force between the aggrecan coated colloidal tip and aggrecan substrate (Figure 5-8b) was larger in magnitude and started at significantly longer distances than for the neutral colloidal tip (Figure 5-8a). The increase in magnitude and range with the addition of aggrecan on the colloidal tip ($\sim 1.5\times$) was much larger that what was

observed with the sharp tip. It is interesting to note, however, that the force increased by less than a factor of 2, which would be expected if the brush on the tip and substrate behaved the same when compressed against each other as when they are compressed separately.

The measurement of the height of the aggrecan brush using contact mode AFM imaging at constant normal load and the standard nanomechanical approach curve both probe normal nanomechanics of the aggrecan brush. The normal force on approach from Figure 5-8 and the total height curve from Figure 5-7 were very comparable although they measured slightly different ranges of the compression (Figure 5-9). During the height measurements, the tip was able to compress the aggrecan layer to higher loads. There were some differences at long range distances and low normal forces. This might be due to two reasons: 1. the height measurement is less accurate at very low normal force (see Chapter 4) and 2. the height measurement both compresses and shears the aggrecan as the tip is scanning. The first point is a minor one and can only really be used to explain the discrepancies between height measured by scanning at $\sim 0nN$ and the force measured at that separation distance by probing. The second point, however, is important. As the tip scans the sample relatively quickly ($\sim 60\mu m/sec$) in the height measurement, the aggrecan brushes are laterally sheared and may not compress in the same way as when the tip comes down directly on top of them. This might explain the small deviation between the two data sets at low normal force and long separation distance. This difference should get smaller with more normal force in scanning and smaller separation distances in probing as the aggrecan is more compressed. This also explains while although differences were observed in the normal force measurement between the neutral OH-functionalized and the aggrecan-functionalized "sharp" tips, there was very little difference between the height measurements made using those tips since the differences in the force curves were observed in the range of where the height measurement deviates from the normal force curve data.

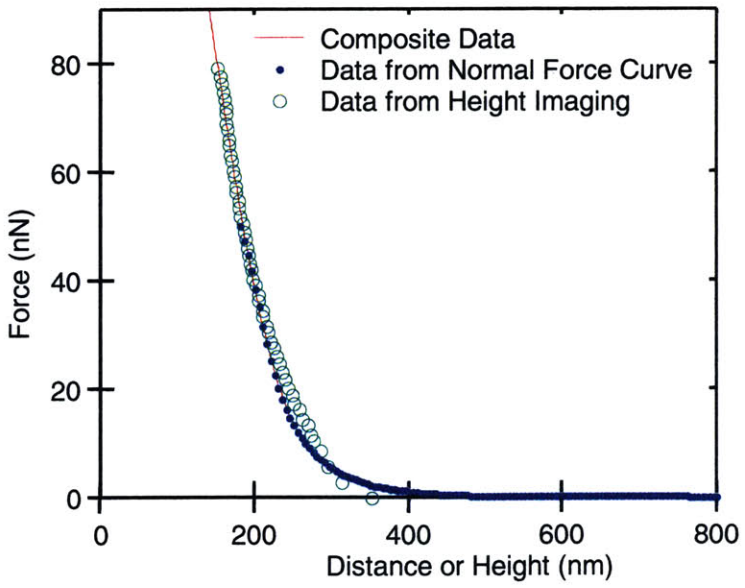

Figure 5-9: Comparison of force-distance curve from normal force measurement on approach (blue dots) and measurement of height of the aggrecan brush using contact mode AFM imaging (green circles) using the aggrecan functionalized colloidal probe tip ($R_{tip} = 2.5\mu m$) at 0.1M NaCl ($pH \sim 5.6$).

5.4 Theoretical Methods

The stress-strain curve from the aggrecan colloid tip versus the aggrecan substrate data was compared to three different electrostatic models (Figure 5-10). Although all three models use the Poisson-Boltzmann equation (Equation 5.3) to calculate the stress from the electrostatic potential distribution at a given strain, they differ in the geometric arrangement of the fixed charges (Figure 5-10) and how these change with the strain (see Figure 5-10 lower diagrams). The Poisson-Boltzmann equation relates the electrostatic potential in space to the free and fixed charges:

$$\nabla^2\Phi = \frac{2FC_0}{\epsilon_w}\sinh\left(\frac{F\Phi}{RT}\right) - \frac{\rho_{fix}}{\epsilon_w} \tag{5.3}$$

where Φ is electrostatic potential, F is the Faraday constant, C_0 is the NaCl concentration, ϵ_w is the permittivity of water, R is the ideal gas constant, T is the temperature in K, and ρ_{fix} is the volumetric fixed charge density in space. This equation can be solved subject to 2 boundary conditions. In this study, constant

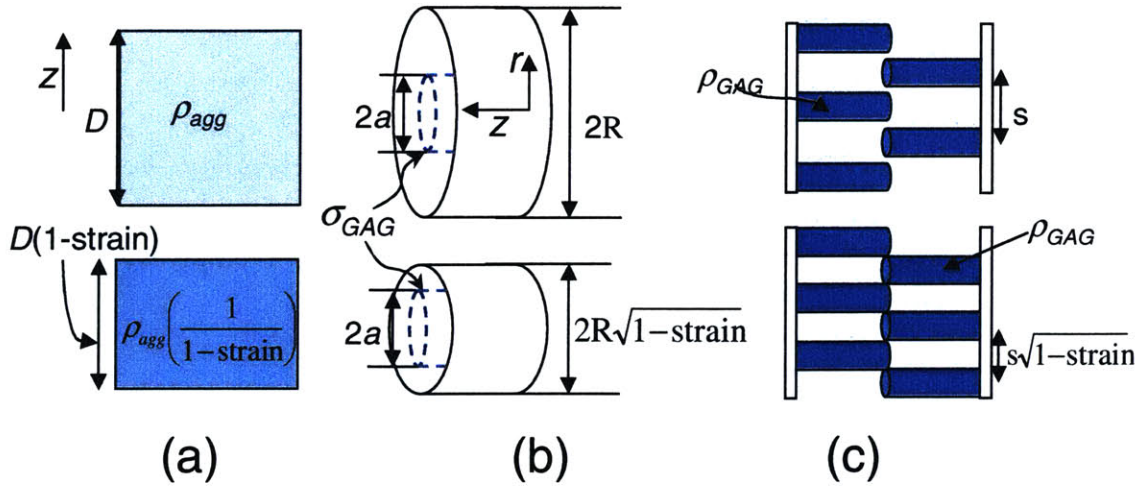

Figure 5-10: Three models for the electrostatic component of the stress between compressing aggrecan brushes. a) Smooth Volume of Charge, b) Unit Cell, and c) Rod models. The schematics on the second row represent how the models change with changes in strain.

charge boundary conditions were used since neither the tip nor the substrate is electrically connected to a source which would maintain their potentials (see Chapter 3 and Appendix B).[24] The total electrostatic energy is calculated from the electrostatic potential (see Chapter 3) and its derivative with respect to z is the stress.[24] The characteristic length over which electrostatic potentials decay is known as the Debye length:$\kappa^{-1} = \sqrt{\frac{\epsilon_w RT}{2F^2 C_0}}$. This is also therefore the length scale for electrostatic forces and it is useful to keep in mind while analyzing the data (see Table 3.2 for values).

5.4.1 Smooth Volume of Charge Model

The first model represents the aggrecan brush region as a smooth volume of charge (see Chapter 3 and Figure 5-10a). The initial volume charge density of the aggrecan brush, $\rho_{fix} = \rho_{agg}$, is fixed as calculated from the measured aggrecan density on the surface and from the charge per aggrecan molecule and the initial separation between the surfaces, $\sim -\frac{2}{D} C/m^3$. The initial separation distance, D, is the full uncompressed height of the aggrecan brush as estimated from the height data as measured by contact

mode AFM (Figure 5-6a&b) and from the point of initial force increase on the force curve (Figure 5-8).[88] The strain is $1 - \frac{\text{separation distance}}{D}$ (at a separation distance of D the strain is 0). As the volume of charge is compressed, the initial separation distance between the two neutral surfaces, D, is decreased and therefore the volume charge density is increased (see Figure 5-10a lower diagram). The Poisson-Boltzmann equation is solved using a Newton method on a finite difference grid (see Chapter 3) to obtain the electrostatic potential everywhere in space, Φ, as a function of separation distance.

5.4.2 Unit Cell Model

The second model, commonly referred to as a "unit cell", has been discussed in detail in the literature.[62, 11] The unit cell (Figure 5-10b) represents a disaccharide unit of a charged glycosaminoglycan, GAG, molecule and its surrounding mobile ions. The unit cell model is cylindrically symmetric and therefore it can be solved in much the same way as the smooth volume charge model above. In this case, the fixed charge due to the GAG chains is represented as a charge density, σ_{GAG}, on the surface of a cylinder with radius, a. The fixed charge density is 0 everywhere except on this surface such that $\rho_{fix} = 0$ in Equation 5.3. The model requires several parameters which were fixed to the values obtained from the literature: the radius of the GAG chain, $a = 0.55nm$,[11] the surface charge density on that surface, $\sigma_{GAG} = \frac{1 \text{ charge}}{0.64nm \times (2\pi a)} = -0.072C/m^2$,[11] and R_u, the radius of the representative cell. The initial R_u can be calculated from the effective volumetric charge density (see the previous section and Appendix G) due to the aggrecan brush: $R_u = 3.07nm$.[11] Since the model is cylindrically symmetric the strain is a second order function of the radius of the unit cell (Figure 5-10). This model represents the nonuniform fields due to a concentrated collection of GAG chains which are in random orientations. It has been shown to model the swelling pressure of GAG solutions very well.[11] The Poisson-Boltzmann equation was solved numerically using a Newton method similar to the previous model.[24]

5.4.3 Charged Rod Model

The rod model describes the time average space taken up by GAG chains in a brush (see Chapter 3 and for further details Appendices B-D).[21, 24] In this model, the fixed charge density ρ_{fix} of Equation 5.3 is equal to ρ_{GAG} inside the cylindrical rods and it is 0 everywhere else. This model requires several parameters (Figure 5-10) which were fixed to the values obtain from the literature. The length of the rods ($h = 41nm$) and the initial spacing between them ($s = 3.2nm$) were fixed to the values measured with AFM imaging by Ng et al.[68] The radius of each cylinder was fixed to the best-fit value from previous experiments with GAG-only brushes ($w = 2nm$, see Chapter 3)[24] and volumetric charge density, $\rho_{GAG} = -31 \times 10^6 C/m^3$, was calculated from the known number of disaccharides per chain (50 from Ng et. al.)[68] and from the volume of each cylinder.

Since this model lacks the one-dimensional symmetry of the previous two, the Poisson-Boltzmann was solved using a slightly more complex Newton method with inequivalent Jacobian on a three dimensional finite difference grid to obtain the potential everywhere in space as a function of decreasing spacing between the rods, s (see Figure 5-10c). This was then converted into an electrostatic energy and stress as a function of separation distance as describe in Chapter 3.[21, 24] The strain is a second order function of the GAG spacing, s, (strain is 0 at the initial spacing $s = 3.2nm$) as shown in Figure 5-10.

5.5 Comparison to Models

The composite curve of Figure 5-9 was converted from force versus distance to stress versus strain (red points in Figure 5-11) as described in the methods. The volume charge model (orange dashed line) overestimates the aggrecan data by a factor of 2-3. The unit cell model (purple dashed line in Figure 5-11) while in good agreement with the data for very low strains (< 0.2), underestimates the data at higher strain. The rod model (solid black line in Figure 5-11) follows the data most closely although it also underestimates the data at large strains (> 0.4).

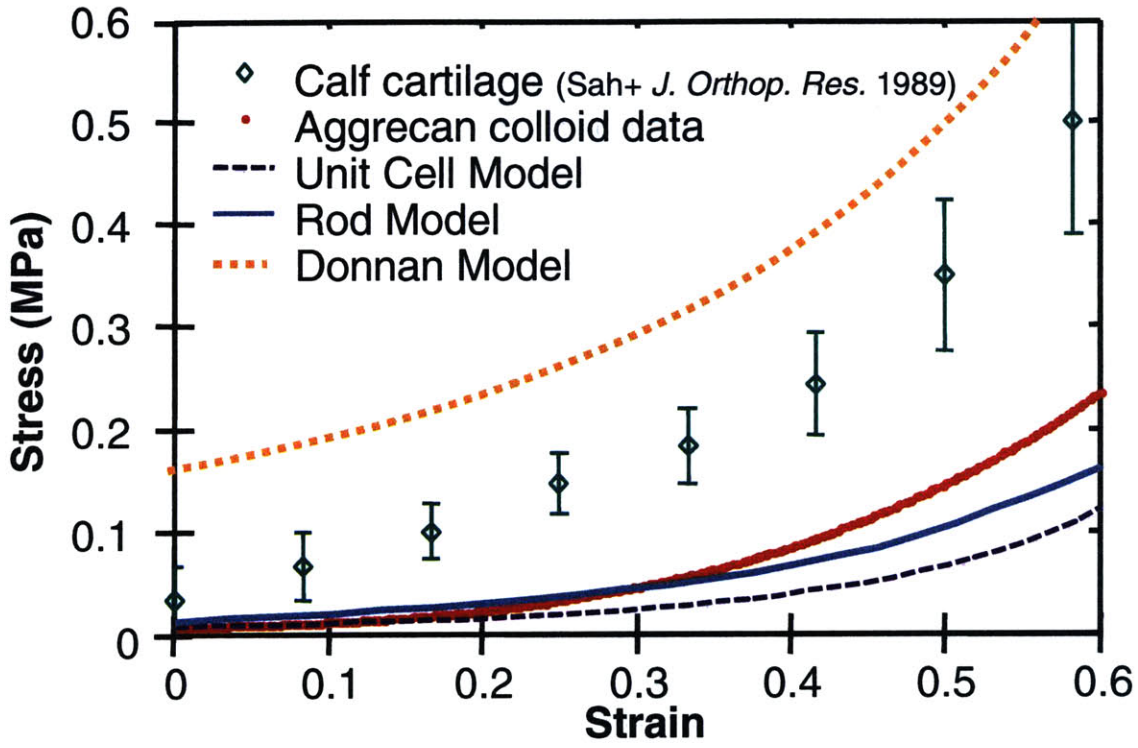

Figure 5-11: The aggrecan brush nanomechanical data converted to stress-strain (red dots) compared to the rod model (black line), the unit cell model (purple dashed line), the volume charge model (orange dashed line) and to data from whole calf cartilage in unconfined compression[85] (green diamonds with standard deviation bars).

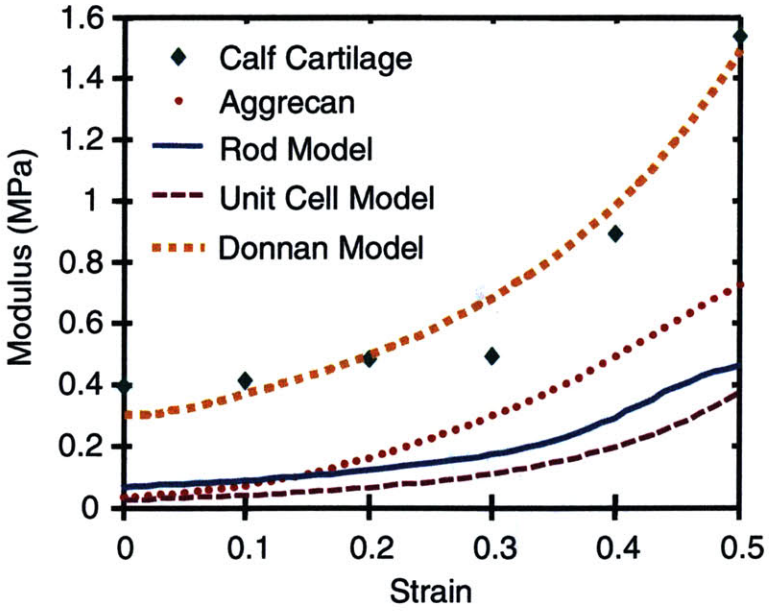

Figure 5-12: The aggrecan brush nanomechanical data converted to modulus versus strain (red dots) compared to the rod model (dark blue line), the unit cell model (purple dashed line), the volume charge model (dashed orange line), and to data from whole calf cartilage in unconfined compression[85] (green diamonds). This graph is the derivative of the curves in Figure 5-11.

The modulus was calculated from the slope of the curves in Figure 5-11 and the results are shown in Figure 5-12. It should be noted that the aggrecan brush data was smoothed out such that the curve in Figure 5-12 represents the average slope of the data. The modulus calculated from the unit cell model was smaller than the aggrecan brush data for all strains. The modulus calculated from the rod model had the same range as the aggrecan brush data $\sim 0.1 - 0.4MPa$). However, the shape of the curve was different: at strains < 0.4, the modulus increased more slowly while at high strains (> 0.4), the modulus increased much more steeply than the experimental data.

The aggrecan brush data converted to stress-strain compares well to the stress-strain data on calf cartilage from Sah et al. in 1989[85] (Figure 5-11). The slope of the stress-strain curve gives a $\sim 0.1 - 0.4MPa$ stiffness for the aggrecan brush layer (Figure 5-12). This is $\sim 50 - 70\%$ of the compressive modulus of calf cartilage ($0.5MPa$)[85] and $\sim$ 50% of the compressive modulus of fetal human epiphyseal

cartilage ($0.7 \pm 0.35 MPa$).[8]

5.6 Discussion

5.6.1 Interaction force between aggrecan molecules as measured with a sharp and colloidal tip results

Although there were only a few aggrecan molecules on the sharp $R_{tip} \sim 50nm$ aggrecan coated tip that could interact with the substrate, a large increase in the magnitude and range of the interaction force between the tip and substrate were measured (Figure 5-3). The marked increase force suggests that even a few individual aggrecan molecules have a significant stiffness associated with them. This individual molecular stiffness seems to be largely dependent on ionic strength (the increase in force with the sharp aggrecan tip decreased with increasing ionic strength) which indicates the importance of electrostatic interactions. This importance of electrostatics is due in large part to the close brush-like packing of the constituent GAG chains along the protein backbone of the individual aggrecan monomers.[63, 68, 88] However, the interaction force measured with the sharp $R_{tip} \sim 50nm$ aggrecan coated tip was much larger than that previously measured between GAG-only brushes using a similar sized tip[88] (Figure 5-4). This is mostly because of the increase in GAG density in the aggrecan brush system but also because of the increase in nonelectrostatic force. In the GAG measurements,[88] there were only very small forces measured at 1M NaCl were a large portion of the electrostatic force is shielded. However, in the aggrecan system, large long-range forces are measured even at 1M NaCl indicating nonelectrostatic forces play a larger role in the interactions between whole aggrecan molecules than between GAG chains only.

The forces between the colloidal tips and the aggrecan substrate were much larger and had a much longer range of interaction. The difference in magnitude between the force measurements using the sharp and colloidal tips was mostly due to the large change in the radius of the tips; the stresses recorded (force normalized by tip

interaction area) were very similar. The large increase in the range of the interaction force is due to the presence of thousands of aggrecan on the colloidal tip that can interact with the aggrecans on the substrate. They are therefore more constrained and are probably in a more brush-like configuration away from the surface of the tip (Figure 5-1). The nonelectrostatic component of this brush-brush interaction force is important as shown by the large long-range forces measured at 1M NaCl when most of the electrostatic interactions should be shielded. However, it is interesting to note that there is a much larger difference between the forces measured in 0.1M NaCl (near physiological conditions) and those measured at 1M NaCl for the aggrecan colloid versus the aggrecan substrate. This is also seen in the significant changed in the brush height between 0.1 and 1M NaCl (Figure 5-6 and see Chapter 4). While the Debye length at 1M NaCl ($\kappa^{-1} \sim 0.3nm$) is much smaller than the spacing between charges along and between GAG chains (on the order of a couple of nm) in the aggrecan brush, it is on the same order at 0.1M NaCl ($\kappa^{-1} \sim 1nm$).

The force (Figure 5-8b) and height (Figure 5-7) did not double when the aggrecan colloidal tip was used as compared to the neutral control tip (Figures 5-8a and 5-6). This indicates that the aggrecan molecules on the tip are interacting with those on the substrate. It is unlikely that the brush layers are compressing independently (i.e. that they exclude each other) but that rather the brushes are interpenetrating. Attractive forces were seen on retraction when nonzero surface delay times were used (see Appendix I) further implying the interpenetration of the brush layer on the tip with that on the substrate.

5.6.2 Comparison of Aggrecan Brush Interaction Forces to Theory

The smooth volume of charge model predicts a stress that is much larger than the measured aggrecan interaction for all strain $0-0.6$. This has previously been reported in the literature[11] and is due to the lack of molecular level nonuniformities in the fixed charge density and therefore in the potential in the model which are present

in the experiment. The spacing between charge groups ($\sim 2-4nm$) inside the aggrecan brush is on the order of the Debye length ($\kappa^{-1} \sim 1nm$) at near physiological conditions (0.1M NaCl). Therefore, the electrostatic potential inside the brush is highly nonuniform as it decays significantly between the charged GAG chains. However, at low ionic strengths (when $\kappa^{-1} > 10nm$), the potential becomes more uniform (since the spacing between charges is negligible compared to κ^{-1}) and all three models behave similarly.[11]

The "unit cell" model fits the data well at low strain. However, at strains higher than 0.2, it underestimates the data because it assumes that the GAG chains are homogeneously distributed (as they would be in a solution). The GAG chains in the aggrecan brush are inhomogeneously distributed since the aggrecan molecules are end-grafted on the surface. The added geometrical constraints of the GAG chains on the aggrecan protein backbone create a fixed charge distribution profile that is more ordered than that found when GAG chains are free to move in solution.

The stress calculated from the rod model follows the aggrecan data well for a large range of strains ($0-0.4$) although it tends to slightly overestimate the data in the lower strain range ($0-0.25$). It is expected that a model which only takes the electrostatic interactions into account will deviate at higher strains when nonelectrostatic forces, such as sterics, become more important. It is surprising, however, that the rod model is so close to the data since it represents a geometry that is somewhat different from that of the aggrecan brush. In the rod model, the cylindrical rods represent the time-averaged space taken up by the GAG chains that are tethered to an infinite plane while in the aggrecan experiment, the GAG chains are tethered to individual aggrecan core proteins. The difference in geometry explains the overestimation of the stress by the rod model. While the unit cell model represents a experimental geometry with randomly oriented GAG chains, the rod model imposes more order than the experimental aggrecan geometry as all the rods in the model are placed on a square lattice parallel to each other. However, the aggrecan density is very high on the surface and therefore the infinite planar arrangement of the rods can model the more complex geometry of the very dense aggrecan brush relatively well.

5.6.3 Comparison of Aggrecan Brush Interaction Forces to Whole Cartilage Unconfined Compression Measurements

The concentration of aggrecan found in articular cartilage is $20 - 80 mg/ml$[18, 64, 100]. The effective concentration of aggrecan in our brush system is $\sim 55 mg/ml$ and therefore is at physiologically relevant density. The electrostatic component of the whole cartilage tissue modulus has been estimated to be $\sim 50\%$ of the total modulus. Since proteoglycans are the most highly charged component of the cartilage extracellular matrix, it is thought that they are responsible for most of this electrostatic component to the modulus.[18, 11] Using the high-resolution force measurements presented here, we can directly calculate a compressive stiffness for the aggrecan alone. This aggrecan stiffness was $\sim 50\%$ to previous measurements in unconfined compression on whole tissue sources which contain similar aggrecan molecules to the ones used in our experiments (i.e. calf femoropatellar articular[85] and human fetal epiphyseal[8] cartilage) (Figure 5-12). The difference between the aggrecan stresses and the whole cartilage data was greatest at high strain (> 0.5). This indicates that aggrecan is especially important for the mechanical properties of cartilage in the normal physiologically relevant strain range and that perhaps the other matrix components such as collagen are responsible for the properties of the tissue in very high (injury) strains.

One area for further study would be to look at the differences between the aggrecan nano-mechanics in quasi-equilibrium such as these experiments and the nanomechanics when the molecules are compressed dynamically. Dynamic measurements could be taken with the current setup by varying the tip velocity on approach. The properties of the aggrecan brushes on retraction are also quite interesting and are discussed in Appendix I.

Appendix A

Background on High Resolution Force Spectroscopy

With the development of high-resolution force spectroscopy (HRFS) instruments like the atomic force microscope (AFM) and molecular force probe (MFP), it is possible to measure the nanoscale interaction forces between molecules. [35, 45] In HRFS, a small (nano-size) probe or tip and a substrate are approached. The probe is on the end of a cantilver that bends in response to the force between the tip and sample. The forces between the tip and the substrate are measured as a function of separation distance on approach and retract.

A.1 Atomic Force Microscope (AFM)

The atomic force microscope (AFM) has been popular tools for imaging surfaces and biological samples for quite some time.[40, 42, 57, 37] There are 2 common modes for imaging with AFM: contact mode and intermittent mode (also known as tapping mode on the Digital Instrument AFM[27] that were used in this thesis).

Contact mode works in much the same way old record players operated. In contact mode, the tip scans across the sample and as it is being dragged, a laser beam measures the deflection of the cantilever. A piezo-electric tube scanner moves the sample in response to the measured cantilever deflection to maintain a constant force

between the tip and sample. In this way, you can obtain a topographical map of the sample from the movement of the piezo (this is the "height" image). You can also look at the output of the deflection signal from the tip movement (this is the "deflection" image). The deflection image does not give you actual heights of topographic features of your substrate. However, because the response of the piezo to the deflection of the cantilever has a delay, the deflection image does highlight edges and can sometimes give more fine detail than the height image. One issue with contact mode though is that very delicate soft samples may be damaged by the force needed to maintain the tip in contact with the substrate. Also, if the tip-sample interactions have large lateral forces as the tip is scanned across the substrate this might cause some distortion or noise of the lateral signal on the normal signal.[27]

To avoid some of these issues, we can e use tapping mode imaging. In tapping mode, the cantilever is oscillated at its resonant frequency (usually several hundred kHz). The tip and substrate are approached until the tip just barely taps the surface as it oscillates. In this way the tip is in contact for only a very small amount of time, the force of tip on the substrate is much smaller, and there is very little lateral torquing of the cantilever. As the tip is tapped across the substrate the piezo is moved so that the oscillation of the cantilever is nearly constant in amplitude. Again, the movement of the piezo gives the height ("height" image). In this case, the change in amplitude will give an "amplitude" image. Similar to the deflection image, this image can sometimes show more of the fine structure of the sample since there is a delay in the feedback with the piezo.[79]

More recently, they have also been used for force measurements as well. [12, 13, 46, 70, 67] In a force measurement, the tip and substrate are approached at a constant rate and the deflection of the tip is measured. With the Multimode Nanoscope IV AFM that was used in this thesis, the sample is approached to the tip at a constant rate until the cantilever deflects some set amount. The tip and substrate can be held at that constant force for a set surface dwell time (usually 0). Then the substrate is retracted. The raw output is the deflection of the cantilever versus the piezo distance (Figure A-1a. To convert this to a force-distance curve, you need the spring

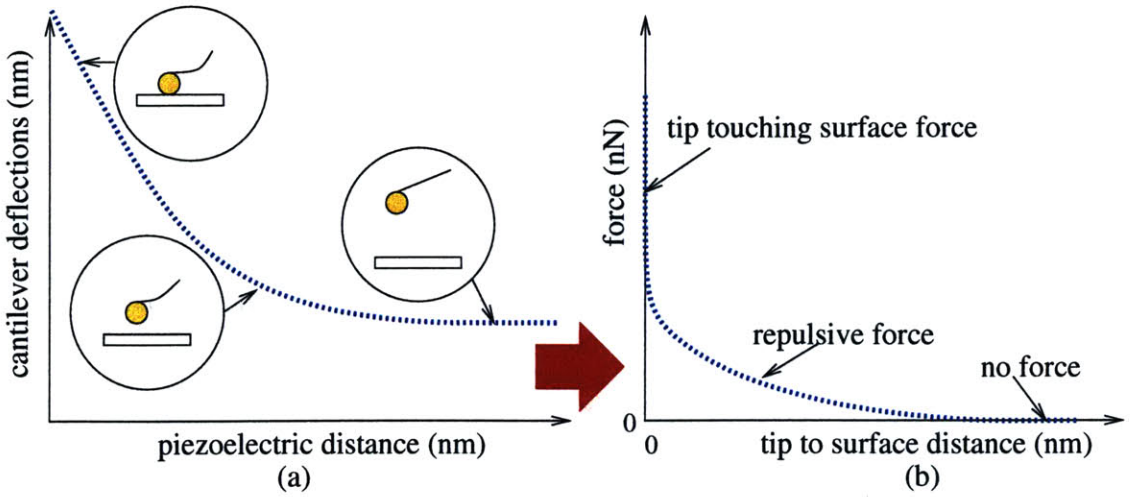

Figure A-1: (a) An example of deflection curve; (b) An example of a force curve.

constant for the cantilever. The spring constant to convert tip deflection to force is obtained by recording the thermal fluctuations of the cantilever away from the surface and fitting the curve to a simple harmonic oscillator model.[52, 14] The curve is then converted to a force versus tip-sample separation distance (Figure A-1b).[27, 78] These measurement techniques are particularly useful for biological applications because they can be carried out in an aqueous environment without damaging the sample.

A.2 Molecular Force Probe (MFP)

The molecular force probe (MFP) is a more recent instrument that is very similar to the AFM but has been optimized specifically for the measurement of force. It overcomes some of the optical interference problems inherent to standard AFMs and has slightly better resolution. The MFP (Asylum Research, Santa Barbara, CA) also measures force versus tip-sample separation distance. The MFP-1D can only do force measurements; it does not have the ability to scan in the x and y directions. However, the newer MFP-3D can scan in both the x and y directions as well as going in the z direction and it is therefore by definition an atomic force microscope. In the MFP, the tip moves up and down while the sample can move from side to side. The basic ideas though are the same; however, there are some key difference between the MFP and the

MultiMode AFM which makes MFP have better normal force measurements. One of the main differences is the use of an adjustable laser focus, novel optic lever geometry, and a low coherence light source that minimize optical interference reflections from the sample. This is particularly important if the sample is highly reflective and the measured forces are small. Also, a piezoelectric translator located on a flexure plate in the head incrementally moves the tip towards and away from the sample at a constant rate. A linearly variable differential transformer position sensor, also located on the flexure plate in the head, quantifies the distance the z-piezo moves the cantilever directly (close-loop feedback), eliminating error due to piezo hysteresis and other nonlinearities, and also reducing or eliminating the effects of thermal drift over long time scales. One of the other differences is that the MFP used an open fluid cell versus the closed fluid cell of the AFM. This has some disadvantages if the experiment runs for a long time as evaporation becomes a problem.

One problem with both the AFM and the MFP is that the tip-sample separation distance is not measured during force measurements. After conversion of the deflection curve (Figure A-1a) to a force curve (Figure A-1b), the force curve is shifted so that the constant compliance regime (the part where the force curve is vertical) is put at distance = 0. However, the tip and underlying sample may not be in contact at that point. This offset, sometimes known as the incompressible layer thickness, needs to be measured independently (see Chapters 4 and 5).[105]

Another instrument that is used to measure nano-scale forces is the surface forces apparatus (SFA).[56, 51, 54] In the SFA, two micron-sized mica cylinders in a crossed geometry are approached. A light is shined through the cylinders and the distance between the surfaces is measured by an interferometric technique. This is very accurate and has a resolution of about 3Å. At the same time, the force is measured from a horizontal leaf spring that supports the lower cylinder. The smallest force detectable is on the order of 10nN. The problem is that this instrument requires transparent flat substrate for the interferometry. Also, it is impossible to probe forces between individual molecules since the SFA is limitted to micron-sized interacting surfaces.

Appendix B

Charge Titration at Surfaces

As stated in the text, we used constant charge rather than constant potential boundary conditions on the surface of the tip and the substrate. In general, the pH at a charged surface will differ from the pH of the adjacent fluid bath since the concentration of H^+ and all other mobile ions will vary with the electrical potential away from the surface.[69] The ionization state of the surface charge groups and the surface pH will depend on bath pH, bath ionic strength, and the pKa's of the ionizable charge groups. A lower bound estimate of the surface pH was calculated using the linearized PB equation and from this, we calculated the self-consistent upper bound for the concentration of the protonated form of the charged groups on the surface.

The local ion concentration depends on the potential, Φ (see equation 3.6). For small enough Φ, (i.e. $\frac{F\Phi}{RT} << 1$), linearization of the PB equation gives:

$$\nabla^2\Phi \approx \frac{2FC_0}{\epsilon_w}(\frac{F\Phi}{RT}) = \kappa^2\Phi \tag{B.1}$$

Similarly, linearization of the local ion concentrations (from equation 3.6) gives an expression for the H^+ concentration:

$$c_{H^+}(z=0) = \bar{c}_{H^+}e^{-\frac{F\Phi(z=0)}{RT}} \approx \bar{c}_{H^+}(1 - \frac{F\Phi(z=0)}{RT}) \tag{B.2}$$

where $c_{H^+}(z=0)$ is the H^+ concentration at the surface at $z=0$, $\bar{c}_{H^+}$ is the known

(measured) bulk H^+ concentration (given from the bulk pH of the solution), and $\Phi(z = 0)$ is the surface potential. The linear approximation will give a tight lower bound even if the potential is not small enough since $e^{-\frac{F\Phi}{RT}} > 1 - \frac{F\Phi}{RT}$ is always true. Therefore, since the local pH is:

$$\mathrm{pH}(z = 0) = -\log(c_{H^+}(z = 0)) \tag{B.3}$$

the pH calculated from the linear approximation of the PB (equation B.1) equation will always be lower than the pH calculated from solution of the full nonlinear equation. Given charged parallel plates of infinite extent (Fig. 3-1a), solution of the linearized PB equation for the potential, $\Phi(z)$, between the plates gives:

$$\Phi(z) = \frac{\sigma_1 \cosh(\kappa(z - D)) + \sigma_2 \cosh(\kappa z)}{\kappa \epsilon_w \sinh(\kappa D)} \tag{B.4}$$

where D is the separation distance between the two plates, σ_1 is the surface charge density of the plate at $z = 0$, and σ_2 is the surface charge density of the plate at $z = D$. We first consider the case of equally charged surfaces, $\sigma_1 = \sigma_2 = \sigma$. We also assume that the ionization processes can be described by a reversible bimolecular dissociation reaction leading to the form of a Langmuir charging isotherm in which the surface charge density, σ, will vary with the pH of the surface:[97]

$$\sigma = \frac{K}{K + c_{H^+}(z = 0)} \sigma_{max} \tag{B.5}$$

where K is the dissociation constant of the charge groups on the surface ($K = 10^{-\mathrm{pK}}$) and σ_{max} is the maximum charge density if all the groups on the surface were charged. From equations B.2 and B.4, we can solve for $c_{H^+}(z = 0)$:

$$c_{H^+}(z = 0) = \frac{1}{2}\left(\bar{c}_{H^+} - K + \sqrt{(\bar{c}_{H^+} + K)^2 - 2\frac{\bar{c}_{H^+} K \sigma_{max} \kappa(\cosh(\kappa D) + 1)}{F C_0 \sinh(\kappa D)}}\right) \tag{B.6}$$

In the limit $D >> 1$, equation B.6 reduces to the H^+ concentration at a single charged

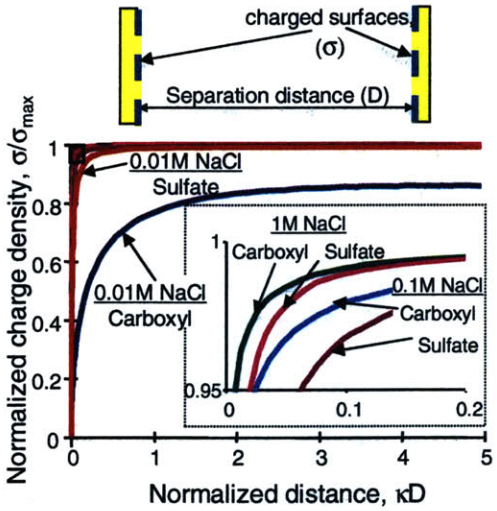

Figure B-1: Surface charge as a function of separation distance at a bath pH of 5.5 and different bath NaCl concentrations assuming all the surface charges are due to sulfate groups (red line = 0.01M NaCl, purple line = 0.1M NaCl, and pink line = 1M NaCl) with pKa = 2 and assuming all the surface charges are due to carboxyl groups (navy line = 0.01M NaCl, blue line = 0.1M NaCl, and gree line = 1M NaCl) with pKa = 3.5. The rectangle in the top left corner was expanded in the inset.

plate:

$$c_{H^+}(z=0) = \frac{1}{2}\left(\bar{c}_{H^+} - K + \sqrt{(\bar{c}_{H^+}+K)^2 - 2\frac{\bar{c}_{H^+}K\sigma_{max}\kappa}{FC_0}}\right) \tag{B.7}$$

In the limit when $\kappa D << 1$, $c_{H^+}(z=0)$ becomes very large and tends to infinity:

$$c_{H^+}(z=0) = \frac{1}{2}\left(\bar{c}_{H^+} - K + \sqrt{(\bar{c}_{H^+}+K)^2 - \frac{\bar{c}_{H^+}K\sigma_{max}(4+(\kappa D)^2)}{FC_0 D}}\right) \tag{B.8}$$

This latter nonphysical limit is a result of the PB assumption that ions take up no volume.

From equation B.8, the surface pH will be lowest when the ionic strength is low and when κD is small. Therefore, to determine whether constant charge boundary conditions were appropriate, we calculated the percentage of charged groups on the surface that would be neutralized (protonated) at $D = \kappa^{-1}$ versus $D \to \infty$ at $0.01M - 1.0M$ NaCl, pH 5.5. The effective surface charge density, σ, is plotted as a function of normalized separation distance in Fig. B-1 for the case where all charges are assumed

Charged group type	$D = \kappa^{-1}$	$D \rightarrow \infty$
Caboxyl groups (pKa = 3.5)[39]	$-0.0750\frac{C}{m^2}$	$-0.0860\frac{C}{m^2}$
Sulfate groups (pKa = 2)[60]	$-0.0987\frac{C}{m^2}$	$-0.0995\frac{C}{m^2}$

Table B.1: Calculated surface charge density if titration is taken into account assuming a bath NaCl concentration of 0.01M with no pH buffers in the bath, a maximum surface charge density of $-0.1\frac{C}{m^2}$, and that all the charge are either all carboxyl or all sulfate groups alone.

to be on the surface and are either carboxyl or sulfate groups alone, and assuming a maximum charge density (σ_{max}) of $-0.1\ C/m^2$. Values of σ for the case of $0.01M$ NaCl bath concentration are tabulated in Table B.

As shown in Table B and Fig. B-1, there is very little change in the surface charge density if all the charge groups are due to sulfate groups and, for such a case, the assumption of constant charge on the tip seems appropriate. GAG molecules contain carboxyl as well as sulfate groups. If all the charge due to carboxyl groups in the GAG molecules were placed on the surface of the substrate, there would be a $\sim 15\%$ change in the effective surface charge density as the tip and the substrate are brought to a separation of $3nm$ at $0.01M$ NaCl; at $0.1M$ NaCl, there would only be a 5.8% in the surface charge density as the tip and substrate are brought to a separation of $1nm$.

However, the carboxyl and sulfate groups in our experiment are on GAG chains and, as such, are not directly on the surface of the substrate. In three dimensions, the GAG charge groups could be modeled as a volume charge density above a neutral substrate as in Fig. 3-1b. The titration of charge groups within a volume charge density can be described as follows[97]

$$\rho_{volume} = \rho_{max}\frac{K}{K + c_{H^+}(z)} = \frac{\sigma_{max}^{brush}}{h}\left(\frac{K}{K + c_{H^+}(z)}\right) \tag{B.9}$$

where ρ_{volume} is the volume charge density of the brush, h is the height of the brush, $\rho_{max} = \frac{\sigma_{max}^{brush}}{h}$ is the maximum charge density when all the groups in the brush are

ionized, and is the local H^+ concentration inside the brush. This is a two-region problem and therefore the linear PB equation (equation B.1) has an added charge term inside the brush:

$$\nabla^2\Phi \approx \kappa^2\Phi - \frac{\rho_{volume}}{\epsilon_w} \quad \text{for } 0 < z < h \tag{B.10}$$

This equation can be solved analytically subject to the following boundary conditions:

$$\left.\frac{\partial\Phi}{\partial z}\right|_{z=0} = 0 \tag{B.11}$$

$$\left.\frac{\partial\Phi}{\partial z}\right|_{z=h_+} = \left.\frac{\partial\Phi}{\partial z}\right|_{z=h_-} \tag{B.12}$$

$$\Phi|_{z=h_+} = \Phi|_{z=h_-} \tag{B.13}$$

$$\left.\frac{\partial\Phi}{\partial z}\right|_{z=D} = \frac{\sigma_{tip}}{\epsilon_w} \tag{B.14}$$

For brush height larger than κ^{-1}, the potential inside the brush (i.e. $0 < z < h$) is:

$$\Phi = -\frac{\sigma_{brush}}{2\epsilon_w h}z^2 + \frac{\sigma_{brush}e^{-\kappa h}}{h}\left(\frac{h^2}{2\epsilon_w} + \frac{h}{\kappa\epsilon_w}\right)\cosh(\kappa h) \quad \text{when } D >> h \tag{B.15}$$

$$\Phi = -\frac{\sigma_{brush}}{2\epsilon_w D}z^2 + \frac{\sigma_{tip}}{\kappa\epsilon_w}\left(\frac{\cosh(\kappa z)}{\sinh(\kappa D)}\right) \quad \text{when } D = \kappa^{-1} \tag{B.16}$$

where $\frac{\sigma_{brush}}{h} = \rho_{volume}$. Using this brush potential, one can first calculate the H^+ inside the brush and then the total charge in the brush as a function of separation distance, D. When setting $\sigma_{tip} = -0.1\ C/m^2$, $h = 10nm$ and $\sigma_{max}^{brush} = -0.1\ C/m^2$ and assuming all the charge in the brush is due to carboxyl groups, then at $0.01M$ bath NaCl, the total charge in the brush changes by at most 7% when the tip and substrate are brought to within one Debye length of each other (see Table B).

This value is still a tight upper bound on the change in charge as a function of distance since we used the upper bound on the tip and brush charges and the lower bound on the brush height. Therefore, it seems reasonable to assume that the charge is constant as a function of separation distance and constant charge conditions are appropriate. Of course, if the bulk pH were much lower or if the charge groups

Charged group type	$D = \kappa^{-1}$	$D \rightarrow \infty$
Caboxyl groups (pKa = 3.5)	$-9.1 \times 10^6 \frac{C}{m^3} \approx 0.094M$	$-9.8 \times 10^6 \frac{C}{m^3} \approx 0.10M$
Sulfate groups (pKa = 2)	$-10 \times 10^6 \frac{C}{m^3} \approx 0.1M$	$-10 \times 10^6 \frac{C}{m^3} \approx 0.1M$

Table B.2: Average value of volume charge density if titration is taken into account assuming a bath NaCl concentration of 0.01M with no pH buffers in the bath, a maximum volume charge density of $-10 \times 10^6 \frac{C}{m^3}$, and that all the charge are either all carboxyl or all sulfate groups alone.

had higher pKa, one would need to include titration into the models discussed here as described. The boundary conditions and volume charge densities would then be functions of the potential. For example, the boundary condition on the substrate could change to: $\frac{\partial \Phi}{\partial z} = -\frac{\sigma}{\epsilon_w}$ at $z = 0$ where $\sigma = \sigma_{max} \frac{K}{K + \bar{c}_{H^+} e^{-\frac{F\Phi(z=0)}{RT}}}$ and it is still possible to solve the nonlinear PB equation with these more complicated expressions for the charge densities using the same numerical techniques used here.

Appendix C

Hemispherical Tip Approximation

All the models associated with Fig. 3-1a-c were solved numerically for a plane parallel geometry. However, in the experiments, the probe tip is a blunted pyramid (Fig. 3-2) that can be modeled as a hemisphere, since the distances probed are on the order of the radius of curvature. Therefore, the calculated forces between planar surfaces were converted to approximations of the force between a flat substrate and a hemispherical tip. The method, based on the original formulation of Derjaguin[25] and sometimes known as Surface Element Integration (SEI)[5], is the numerical version of the integral of a uniform normal stress or pressure over the surface of the hemisphere tip. This method will give the appropriate total force only if the stress (force per unit area) is everywhere normal to the surface. For the case of electrostatic forces, this requirement is automatically met if the surface is an equipotential (i.e., the case of a constant potential boundary condition), since the electric field and therefore the electrical stress are everywhere normal to an equipotential surface. However, when a curved probe tip or a non-infinite planar surface (e.g., the substrate under the brush) has a constant charge density, that surface is no longer an equipotential and the E-field and electrical stress will not be everywhere normal to the tip and substrate surfaces. This approximation method will then underestimate the total force, since tangential components of the stress are not taken into account. Therefore, this method can only be used to estimate the force between a constant charge hemispherical tip and a substrate when the radius of the tip is much larger than κ^{-1}, since the

tangential components of the stress will then be small. This method has advantages over the standard Derjaguin approximation in which the force between a hemisphere and plane separated by distance D is approximated by calculating the force per unit area between two infinite planes separated by D and then multiplying by $2R_{hemisphere}$. This latter Derjaguin approximation is only valid when $R_{hemisphere}$ is very large compared to D.[55] Although this approximation is typically justified for the geometry of the surface force apparatus (SFA),[55] it is not justified with many AFM probe tip geometries, such as our using a probe tip radius of $25 - 50nm$. The SEI Derjaguin approximation is valid for any value of D as long as $R_{hemisphere}$ is larger than the κ^{-1}. In addition, it can be used for geometries other than hemispherical, while the standard Derjaguin approximation is only valid for convex tip geometries.[5]

Appendix D

Extensions of the Models: Aqueous Solutions with Divalent Ions and Non-Brush Polyelectrolyte Systems

The models described in Chapter 3 can be extended to model other non-brush systems and for systems with multivalent ions in solution. Examples are shown below.

D.1 Modeling systems with divalent ions

The addition of divalent ions is relatively easy to incorporate into all of the models described Chapter 3. Although there is an added term in the Poisson-Boltzmann equation, the numerics (Newton method on finite diferences) used to solve it do not change. Instead of using the 1:1 electrolyte form of the Poisson-Boltzmann equation (Equation 3.9), the more general equation 3.8 is used. The extra terms also carry into the energy calculation. The example in the next section on poly(ethylene oxide) mushroom uses this.

It should be noted that whenever mulivalent ions are used in the experiment, even in low concentrations, they should be included in the electrostatic force calculation. That is because the higher the valence of the ions the more fixed charge it is able to screen. As shown in Figure D.1, the potential away from the surface of charge

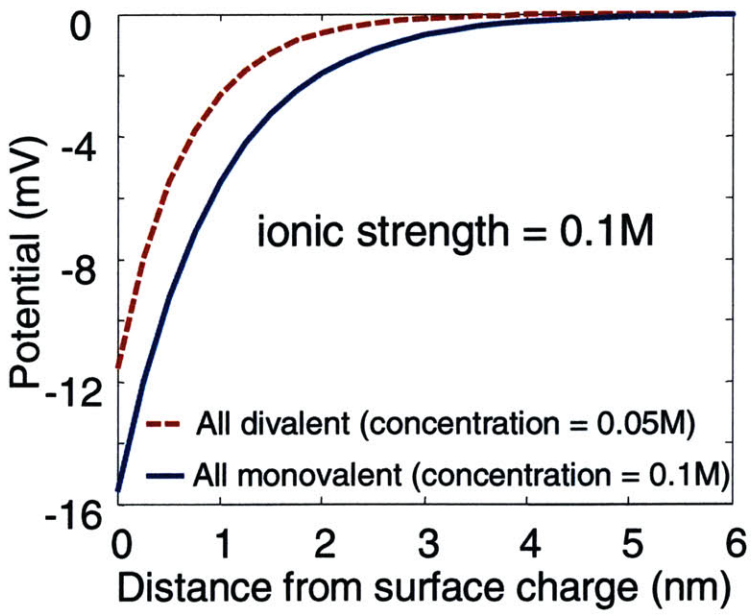

Figure D-1: The electrostatic potential away from a surface of charge ($-0.01C/m^2$) as a function of distance in 0.1M ionic strength bath when all the mobile ions are divalent (red dashed line) and when all the mobile ions are monovalent (blue line).

is smaller in magnitude and decay more rapidly when divalent ions are used instead of monovalent ones even if the total ionic strength is the same. Therefore, in a solution of divalent ions, two surfaces have to be closer together before they feel the same magnitude electrostatic force than they would need to be in a monovalent salt solution.

D.2 Modeling compression of a poly(ethylene oxide) mushroom

Poly(ethylene oxide) (PEO) is a synthetic polymer that is used extensively to provide a protective coating to improve protein resistance of biomaterial surfaces. These chains are end-grafted onto substrates at very low densities and probed with a variety of different probe tips using the Molecular Force Probe (MFP).[84, 83] When grafted at low density (the spacing between the chains is much less than the Flory radius), PEO chains will adopt a mushroom configuration where the theoretical radius of

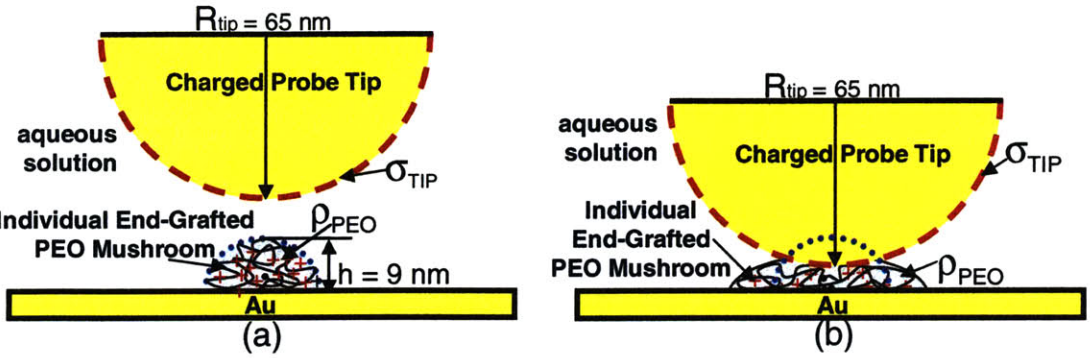

Figure D-2: Schematic of positively charged Poly(ethylene oxide) (PEO) mushroom being compressed by a negatively charged tip: (a) uncompressed PEO mushroom and (b) PEO mushroom compressed. The model assumes that the volumetric charge density remains constant as the mushroom is deformed (constant volume deformation).[84]

the mushroom is equal to the Flory radius ($\sim 9nm$ in the case of the PEO chains used in the experiment). If these chains are charged, this can be modeled as a small hemisphere of fixed charge density (see Figure D-2).

Since it is possible for PEO carry a positive charge due to the ether oxygen atoms chelating metal cations in electrolyte solution [53] the hypothetical case for all of the oxygen, atoms being involved in chelation is considered yielding a maximum charge per PEO molecule of $+3.52 \times 10^{-17}C$. A single PEO chain was modeled as a uniform hemispherical-shaped volume of positive charge density, $\rho_{PEO} = 23.05 \times 10^{6}C/m3$, whose radius was equal to the Flory radius of PEO $= 9nm$ and the probe tip was modeled as an impermeable hemisphere with a constant negative surface charge per unit area, ($\sigma_{tip}(HSA) = -0.0064C/m^2$, $R_{tip} = 65nm$).[17] Since the buffers used in the experiment contain divalent anions, the Poisson-Boltzmann equation has an extra term:

$$\nabla^2\Phi = \frac{F}{\epsilon_w}\left(c_- e^{\frac{F\Phi}{RT}} + 2c_{2-}e^{\frac{F\Phi}{RT}} - C_0 e^{-\frac{F\Phi}{RT}}\right) - \frac{\rho_{PEO}}{\epsilon_w} \tag{D.1}$$

where Φ is the electrostatic potential, F is Faraday constant, ϵ_w is the permittivity of water, R is the gas constant, T is the temperature, C_0 is the ionic strength, c_- is the monovalent anion concentration, c_{2-} is the divalent anion concentration. When the separation distance between the probe tip and the substrate is less than the radius

of the PEO hemisphere, the compressed PEO molecule was modeled as a spheroid whose volume was equal to the initial PEO hemisphere volume (see Figure D-2b). The boundary conditions are the same as the volume charge model (see Chapter 3 Section 3.3.2). There is also an additional term in the electrostatic free energy equation:

$$\begin{aligned} W_e(z,q) &= \int_{\text{surface}} \sigma\Phi dS + \int_{\text{volume of mushroom}} \rho_{PEO}\Phi dV \\ &\quad - \int_{\text{volume}} RT\left(c_-(e^{\frac{F\Phi}{RT}}-1) + 2c_{2-}(e^{\frac{F\Phi}{RT}}-1) + C_0(e^{-\frac{F\Phi}{RT}}-1)\right)dV \\ &\quad - \int_{\text{volume}} \frac{\epsilon_w}{2}(\nabla\Phi)^2 dV \end{aligned} \tag{D.2}$$

The PB equation was solved numerical using a Newton method with inequivalent Jacobian on a 3D finite difference grid[21] and the force was calculated as described in Chapter 3.

Although the long range electrostatic forces are attractive since the charged mushroom and the tip are opposite in charge, the force does become repulsive for shorter distances when the mushroom is fully compressed under the tip and the charge density increases (see Figure D.2). The model was compared to the data between a PEO chain and human serum albumin (HSA). It does not match the data well and the repulsive interaction between PEO and HSA was later found to increase with increase ionic strength further showing that this force was in fact not electrostatic in origin.

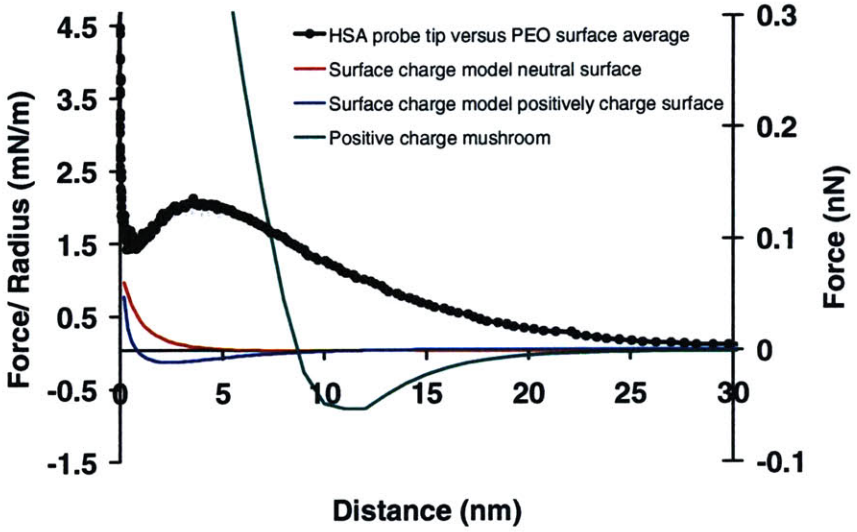

Figure D-3: Compare the interaction of HSA and PEO (black dots) to different electrostatic models. The HSA is modeled as a negative surface charge density while the PEO surface is modeled as a neutral surface (red line), a positive surface (blue line), and a positive mushroom (green line).

Appendix E

Modeling forces between opposing GAG brushes

The modeling results summarized here are an excerpt of a published paper in the Journal of Biomechanics in 2004.[90] In these experiments, GAG molecules were end grafted to both the tip and the substrate and they were brought in contact using the MFP. They were modeled using an interdigitating rod model. The interdigitating and compressed rod models (see Chapter 3) are slightly different for the values of the experiment. However, this difference was within the noise of the experiment (see Figure E) and since there is some evidence that GAG brushes interdigitate when they are brought together[68], only the interdigitated model was included in the publication.

E.1 Theoretical Modeling Methods

Nanomechanical data were compared to the predictions of a charged-rod Poisson-Boltzmann (PB) model for electrostatic double layer forces as described previously (see Chapter 3).[24] The time-averaged space occupied by an individual CS-GAG chain and its fixed charge groups was represented by a circular cylinder having GAG height, h, effective rod radius, w, and a fixed uniform volume charge density. Opposing cylinders interdigitate as they are brought together on approach and, for $D < h$,

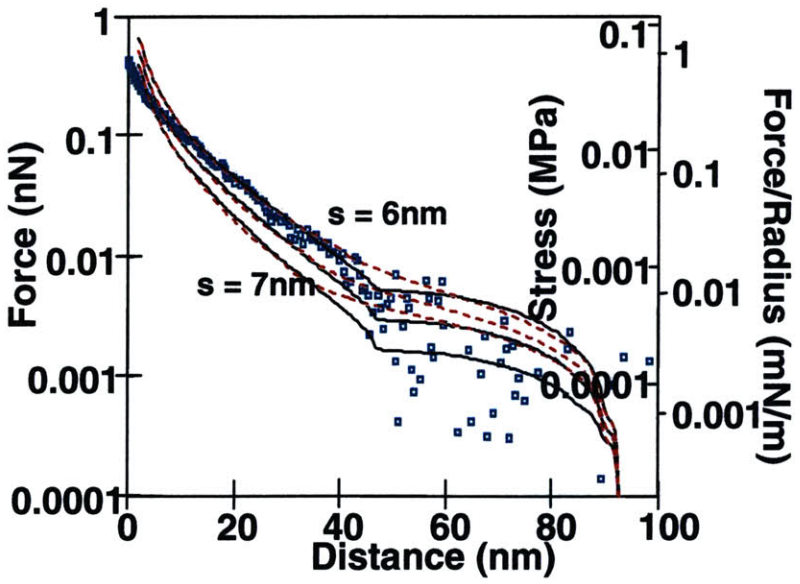

Figure E-1: Force versus separation distance for a GAG-functionalized probe tip vs. GAG-functionalized planar substrate with $s \sim 6.5nm$ at pH 5.6, 0.1M NaCl (squares) compared to the predictions of the interdigitated (black line) and the compressed (red dashed line) rod models with parameter values fixed at: [NaCl]=0.1M, $R_{tip} = 50nm$, $h = 45nm$, $w = 2nm$, $s = 6 - 7nm$, $Qrod = -8 \times 10^{-18}C$.

each rod deforms while maintaining a constant volume. The PB equation was solved numerically in a plane parallel geometry to find the electrical potential, Φ, in space using a Newton method on a finite difference grid was then used to calculate the electrostatic free energy, and the force was calculated as the derivative of the free energy with respect to distance perpendicular to the sample plane. The probe tip geometry was approximated as a hemisphere by using the calculated force between the planar surfaces and summing up the force on appropriately sized concentric cylinders. Based on biochemical and biophysical measurements on rat chondrosarcoma GAGs used in our study, the average GAG chain was assumed to be 25 disaccharides long. Therefore, the following fixed parameters values were used in the model: total GAG (cylinder) charge, $Qrod = -8 \times 10^{-18}C$ (assuming one ionized COO^- and $SO3^-$ group per disaccharide); probe tip end-radius $R = 50nm$;[88] $h = 45nm$ (measured by VASE), effective rod radius, $w = 2nm$, and inter-GAG spacing, $s = 6 - 7nm$ (measured by scintillation counting).

E.2 Results: Comparing the GAG-GAG measurement to the rod model

The data at 0.1M NaCl (Figure E) were compared to the predictions of a Poisson-Boltzmann-based theoretical model that describes normal interaction forces between two opposing surfaces of end-grafted rods of constant volume charge density and finite length, which deform by interdigitating. Model parameter values were fixed at their known values obtained from independent characterization techniques (see Materials and Methods section), and the inter-rod separation distance was set at $s = 6 - 7nm$. At $D = 85nm$ the model predicted a slight inflection point corresponding to the edges of the two GAG layers making contact with each other. Very little repulsive force was predicted or observed at this distance D for 0.1M NaCl. In the interdigitation regime ($45nm < D < 85nm$), the measured force is very low and approaching the resolution limit of the instrumentation; thus, a quantitative comparison between model and experiment was difficult. At $D = 45nm$ (i.e. $D = h$) another inflection point was predicted by the model corresponding to the point where the top of the rods begin to hit the hard walled substrate. At this position, the effective rod radius, w, begins to increase as D decreases such that the rod maintains a constant volume. For $D < 45nm$, the most physiologically relevant strain regime, the theoretically predicted force matched the data well for reasonable model parameter values, especially for $s = 6nm$.

E.3 Discussion

As expected, the strong dependence of the measured GAG-GAG interaction force on ionic strength and pH suggested that electrostatic repulsion dominates these interactions. A comparison of the results of and previous data[89, 88] shows that repulsion between opposing GAG chains is greater and occurs over a longer range than that between a GAG-functionalized substrate and charged tip or a GAG-functionalized tip and charged substrate. Qualitatively, the deformation of opposing GAGs may mimic

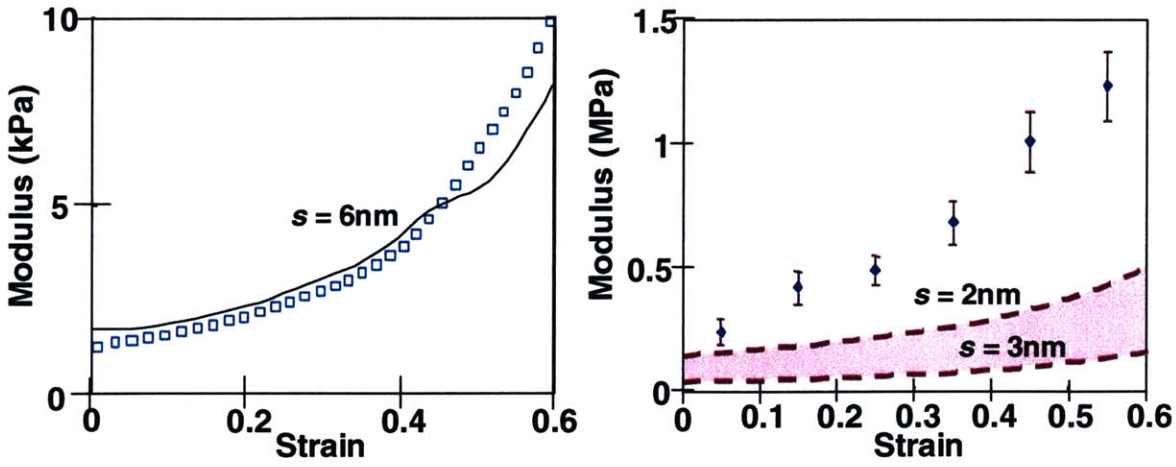

Figure E-2: (a) Effective compressive modulus associated with GAG-GAG interactions calculated from nanomechanical data (squares) of Figure E versus compressive strain, estimated from strain $= 1 - (D/h)^2$; the GAG-GAG modulus is compared to the prediction of the interdigitated charged rod model (s=6nm) (black line). (b) Equilibrium compressive modulus of human ankle cartilage measured in confined compression (blue diamonds) compared to the component of the modulus predicted by interdigitated charged rod model of GAG-GAG electrostatic repulsive interactions with parameters values $s = 2 - 3nm$, $h = 30nm$, $w > 0.5nm$ (shaded region inside dashed lines).

certain aspects of intratissue loading in which the substrate and tip act as boundary conditions (in 2D) similar to that provided by aggrecan core protein and other ECM molecules in 3D. We further explored the implications of these measurements to tissue level mechanical properties.

E.3.1 GAG data compared to models

Using the nanomechanical data and theoretical predictions of Figure E (0.1M NaCl, pH$\sim$ 5.6) we calculated the component of an effective compressive modulus associated with GAG-GAG electrostatic interactions as a function of normal (compressive) strain for the GAG density corresponding to $s \sim 6$ (Figure E.3a). The resulting electrostatic component of the modulus increased nonlinearly with compressive strain, reaching a maximum value of $\sim 10kPa$ at 0.6. Strain, ϵ, was estimated as the 2nd order function: $\epsilon = 1 - (D/h)^2$, thus representing the experiment as a 2-dimensional compression of

opposing GAGs, with $D = h$ taken to be the undeformed, zero-strain length scale). The interdigitating charged rod model predicted the trends of the strain-dependent GAG-interaction modulus very closely for reasonable values of model parameters (Figure E.3a). The small inflection observed in the model prediction at 0.45 is due to the change in slope of the force profile that occurs as the rods transition from approaching and interdigitating at constant volume (and constant charge density) to the position at which the rods have expanded to fill their individual unit cells and further compression causes the volume charge density to increase with decreasing separation distance. This inflection was not observed in the nanomechanical data, suggesting that there is no such sharp transition between regimes in the experiment.

E.3.2 Comparison of GAG-GAG Measurement and Model to Tissue Biomechanical Data

The equilibrium modulus of cylindrical disks of normal adult human ankle cartilage measured in confined compression was $\sim 0.25 - 0.5MPa$ in the $5 - 25\%$ strain range (Figure E.3a), and increased nonlinearly to $\sim 1.2MPa$ by 60% strain, modulus values that were ~ 2 orders of magnitude greater than the GAG-GAG modulus of Figure E.3a. This disparity is mainly due to the fact that the GAG density in the nanomechanical experiments was $\sim 4\times$ smaller than the known GAG density in human ankle tissue.[99] We therefore recomputed the component of the modulus attributed to GAG-GAG electrostatic repulsive interactions using the charged rod model with a range of model parameters known to include values reported for adult GAG and aggrecan cartilage (i.e., $s = 2 - 3nm$, $h = 30nm$[68]). The results (Figure E.3b) show that the GAG-GAG component is predicted to be 1/3 to 1/2 that of the measured tissue modulus. This finding is consistent with previous experiments showing that electrostatic interactions account for $\sim 50\%$ of the total compressive modulus of cartilage,[31] and that the compressive modulus of cartilage is generally proportional to its GAG content.[104] In addition, we now suggest that it may be possible to explore the consequences of specific nanomolecular structural parameters

on tissue level properties using such an approach. Thus, the comparison between theory and experiment in Figure E.3b exemplifies a bridge between molecular level structure and tissue level biomechanical properties. Of course, values for GAG structural parameters (e.g., s and h) will clearly vary with cartilage species, age, and location. Thus, a limitation of our comparison is that the GAGs were from rat chondrosarcoma cells while the tissue was from adult human ankle. (The rationale was the need to use well characterized metabolically labeled ^{3}5S-GAGs derived from a high density cell culture, since this was the only way to achieve radiolabel specific activity that was high enough to enable assessment of GAG grafting density.) In addition, human aggrecan has an abundance of keratan sulfate (KS) in the CS-GAG domain, which may contribute to electrostatic interactions, as well as to the spacing between CS-GAG chains along the core protein.[15] Ongoing studies are aimed at the combined use of experiment and theoretical modeling to address such issues. Additional studies focus on measurement of nanomolecular interactions between whole aggrecan molecules. The dependence of the measured nanomechanical force on aggrecan structure and the location of the charge along the GAG molecules will again depend on tissue age and disease state, and can be directly compared to the properties of the parent normal or osteoarthritic tissue using the methods similar to those described here. In summary, unique nonlinear, long-range repulsive behavior was observed in the direct measurement of GAG-GAG interactions, and comparison with a Poisson-Boltzmann-based polyelectrolyte "charged rod" model for electrostatic double layer interactions provided strong evidence that nonplanar charge distributions and lateral electrostatic interactions of GAG macromolecules play a major role in the observed molecular interactions.

Appendix F

Comparing nanomechanical data to macroscopic measurements

In order to compare nanomechanical data to macroscopic measurements, it is sometime helpful to convert standard high resolution force spectroscopy force-distance curves to strain versus strain curves. From such curves, we can also then calculate an apparent stiffness of the molecular components being probed which can be compared to macroscopic modulus measurements.

F.1 Converting force to stress

There are three ways one can estimate the stress (force per unit area) that is being applied on the sample by the tip. First, we approximate the interaction area on the tip analytically and sample and divide the force by this analytical approximation. Second, we approximate the stress by deconvolving the function for the probe tip geometry (i.e. do the inverse of Appendix C). Third, we could run complex finite element simulation which would model what the stresses are everywhere on the tip and sample. We will discuss the first to methods here. The third method is much more computationally intensive and requires many modeling assumptions. Therefore, at least for the data presented in this thesis, the effort did not seem worthwhile.

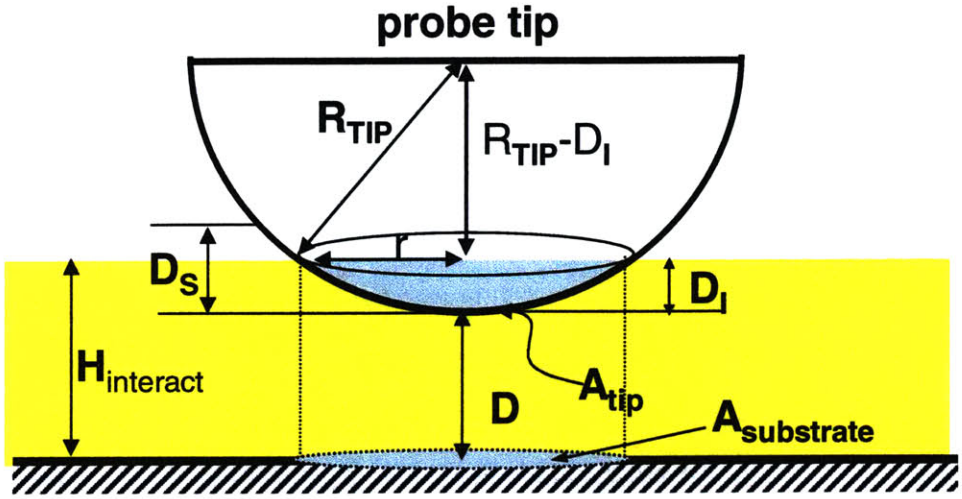

Figure F-1: Schematic showing the interaction area on the tip and the substrate for a hemispherical tip.

F.1.1 Approximating the interaction area

For a first approximation of the interaction area of a large tip at close distances, we can use the Derjaguin approximation[25] which is just $2\pi R_{tip}$. However, this is not always the case so here are a few other approximations one can make.

If we assume that the tip is a hemisphere, then the math becomes relatively simple (Figure F.1.1). First we assume that the interaction starts at some distance $\mathrm{H}_{\mathrm{interact}}$ from the surface. Therefore, the interaction area on the substrate is the projection of the piece of the hemisphere that is lower the distance $\mathrm{H}_{\mathrm{interact}}$ which is just the cross-section of the hemisphere at a distance $R_{tip} - D_I$ from the center where $D_I = \mathrm{H}_{\mathrm{interact}} - D$. This is just $A_{\mathrm{substrate}} = \pi(R_{tip}^2 - (R_{tip} - D_I)^2)$. The interaction area on the tip is the surface are of the piece of sphere in the interaction region: $2\pi R_{tip} D_I$. This is a pretty good model for colloidal tips or for experiments using standard AFM pyramidal probes when the interaction distance is much smaller than the tip radius.

For experiments using standard pyramidal probe tip where the probe tip radius, R_{tip}, is not much larger than the interaction area, the non-spherical part of the tip must be accounted for. However, a blunted square pyramid is a little complicated in that the cross-sections of the pyramid are square whereas those of the blunted part near the end are mostly round. This geometry is not exact and can vary from tip to

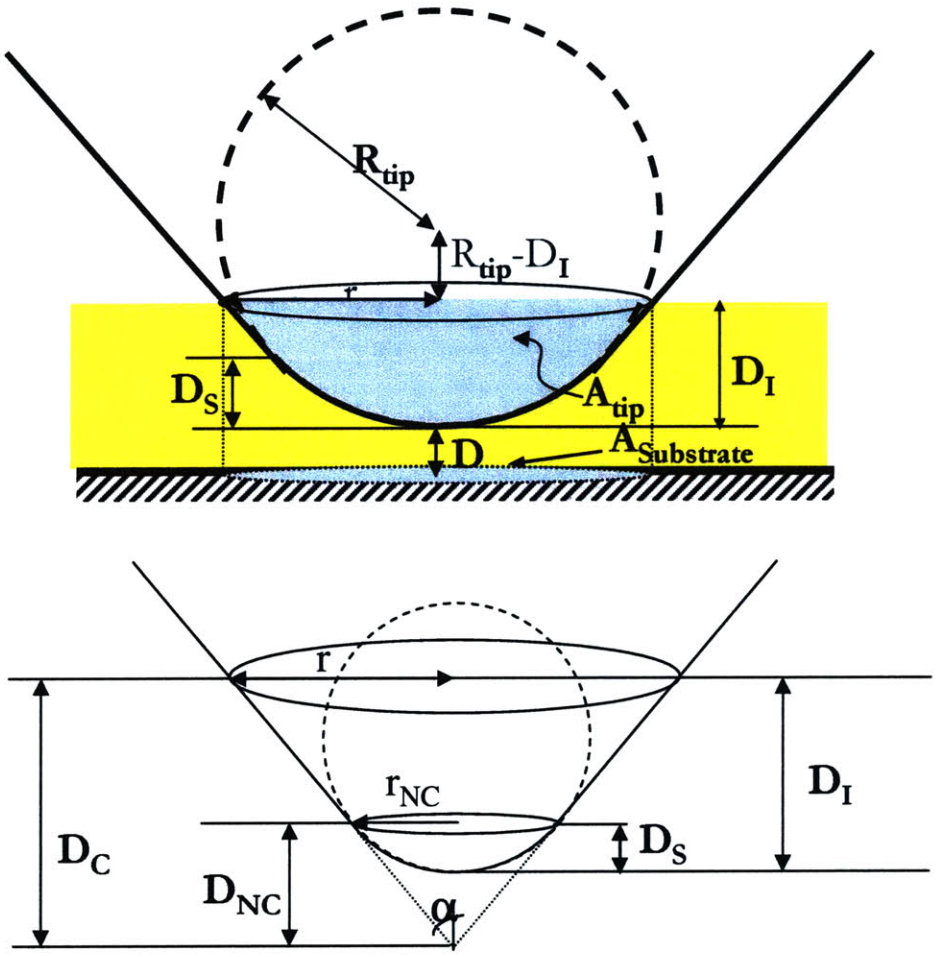

Figure F-2: Schematic showing the interaction area on the tip and the substrate for a blunted cone tip.

tip. One can model this by using a square pyramid that transitions to a sphere at a certain point. However, this tends to introduce kinks in the convert stress curve which were not measured in the data and are solely due to the tip model. The simple solution is to model the tip as a blunted cone (Figure F.1.1) so that the cross-sections remain circular and the interaction area functions are smooth. For separation distances that are large ($D_I < D_S$), then we are still in the region where the tip is modeled as a piece of sphere the equations above hold. When $D_I > D_S$, then the area on the substrate is the cross-sectional area of the cone (πr^2 on Figure F.1.1). The radius of the cross-section at that point will be $r = D_C \tan(\alpha) = \left(D_I + \frac{R_{tip}}{\sin(\alpha)} - R_{tip}\right)\tan(\alpha)$ where α is the half angle of the cone (see Figure F.1.1). The area for the substrate simplifies to:

$$A_{\text{substrate}} = \pi\left(R_{tip}^2 - (R_{tip} - D_I)^2\right) \text{ when } D_I < D_S \tag{F.1}$$

$$A_{\text{substrate}} = \pi\left(D_I + \frac{R_{tip}}{sin(\alpha)} - R_{tip}\right)^2 \tan(\alpha)^2 \text{ otherwise} \tag{F.2}$$

The area on the tip will be the surface area of the truncated cone plus the area of the piece of sphere. Therefore, the area for the tip will be $\pi(r\sqrt{(r^2 + D_C^2)} - r_{NC}\sqrt{(r_{NC}^2 + D_{NC}^2)} + R_{tip}D_S)$ with the parameters as defined on Figure F.1.1. After some trigonometry and algebra this simplifies to:

$$A_{tip} = 2\pi R_{tip} D_I \text{ when } D_I < D_S \tag{F.3}$$

$$A_{tip} = \pi\left(\frac{D_I + Rtip(1 - \sin(\alpha))}{\cos(\alpha)}\right)^2 \text{ otherwise} \tag{F.4}$$

F.1.2 Deconvolving the surface area

The method to calculate an approximation for the force on a hemisphere giving the stress on parallel planes as a function of separation distance described in Appendix C can be represented in matrix form. So given the stress, $\mathbf{P}$, on parallel planes from distance D to $D + R_{tip}$ in increments of Δ (so P is a R_{tip}/Δ sized row vector), we can write the operation of getting the force on a hemisphere at distance D from a surface

as follows:

$$F_{\text{sphere}}(D) = \mathbf{P} \cdot \begin{bmatrix} 2\pi\Delta(R_{tip} - 0.5\Delta) \\ \vdots \\ 2\pi\Delta(R_{tip} - \Delta(i - 0.5)) \\ \vdots \\ pi\Delta^2 \end{bmatrix} \tag{F.5}$$

where i is the index into the vector. So now if you want the force from D_{start} to D_{end}, $\mathbf{F}$ (it's a row vector now too), you can stack up equation F.5 to get a matrix equation (putting 0 in the matrix for when $R_{tip} - \Delta(i - 0.5), 0$):

$$\mathbf{F} = \mathbf{PM} \tag{F.6}$$

Therefore, one simple way to approximate the stress from the force is just to do the inverse operation:

$$\mathbf{P} \sim \mathbf{F}_{\text{experimental}}\mathbf{M}^{-1} \tag{F.7}$$

F.2 Converting distance to strain

Unlike the problem of converting force to stress, the problem of converting distances in high resolution force experiment to nanomechanical strain requires a lot of knowledge of the particular molecular system being probe. While one dimensional strains are appropriate in certain condition (if the tip is very large for example), that might not always be appropriate. Another issue is the length-scale of the experiment and how to define 0 strain. Some of this is discussed for the aggrecan system in Chapter 5. In this case, there were 3 main assumptions made in the calculation of the strain. The first was that the strain was a 1 dimensional function of the distance $1 - \frac{D}{D_0}$, where D is the tip-substrate separation and D_0 is the distance at which the strain is set to 0, since the aggrecan is very dense and the tip is very large compared to the spacing between molecules. This means that when the tip compresses the molecules by a small amount δ the molecules will also compress by that amount since they are

so constrain by their neighbors. The other two assumptions deal with D_0. It was assumed that the brushes fully interdigitate before compressing meaning that D_0 is equal to the brush height, h. If the brushes had been assumed to completely exclude then $D_0 = 2h$. Finally, it was assumed that h was assumed to be $290nm$ as estimated from the the height data as measured by contact mode AFM (Figure 5-6a&b) and from the point of initial force increase on the force curve (Figure 5-8).

To further highlight how the calculation of strain is very problem specific, the calculation of strain for the GAG only brush system from Appendix E is compared. In this case, a 2 dimensional strain model was used $1 - (D/h)^2$, thus representing the experiment as a 2-dimensional compression of opposing GAGs, with $D = h$ taken to be the undeformed, zero-strain length scale. This is because in this experiment the spacing of the GAG chains was much greater. Therefore, when the tip moved by some small amount δ, the GAG molecules can move a little bit out of the way and therefore would only compress by $\sqrt{(\delta)}$. The brush height was also taken to be the 0 strain point in this experiment.

Appendix G

End-grafting of aggrecan on gold

G.1 Protocol details for attaching aggrecan to gold

Fetal bovine cartilage was obtained from the epiphyseal growth plate region and processed. Purified aggrecan (A1A1D1D1) was then obtained as described by Ng et al. 2003[68] The aggrecan was first diluted to a concentration of $0.5mg/ml$. Then, enough dithiobis(sulfosuccinimidyl propionate), DTSSP (Pierce), was added to get a 1μM solution. This excess DTSSP was allowed to react with the amine groups on the aggrecan core protein for $\sim$ 1 hour (see Figure G-1). Dithiothreitol, DTT (Pierce), was added to get a 1mM concentration and allowed to react for $\sim$ 1 hour in order to break all the disulfid bonds. These excess reactants were removed by spinning at 3500 rpm overnight with a 10kDa cutoff centrifugal filter. The aggrecan remains on top of the filter and the reactants will go through to the bottom. The vial containing the excess reactants was removed, the tube with the filter was turned upside down and spun for another 30 min. Then enough deionized water was added to the aggrecan to make a $1mg/ml$ concentration. The solution was either used immediately, stored in the 4° refridgerator for up to 2 weeks, or in the $-80°$ freezer for up to 2 months.

Silicon wafers (Recticon Enterprises Inc., Pottstown, PA; test grade) and Si_3N_4 cantilevers (Thermomicroscope, Sunnyvale, CA) were coated with $2nm$ of chromium to promote the adhesion of gold, followed by a $100nm$ of gold deposited using thermal evaporator at $1.5\frac{A}{s}$ and a pressure of $\sim 2 \times 10^{-6}$ Torr. $\sim 1cm \times 1cm$ squares were

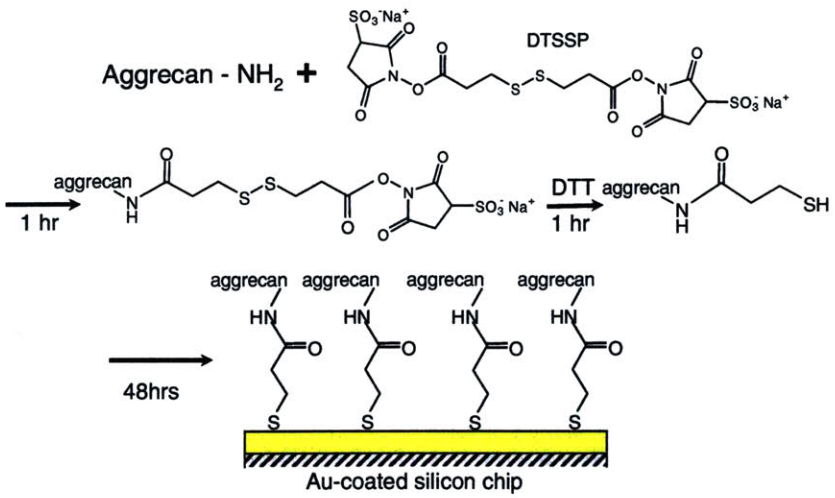

Figure G-1: Attachment of aggrecan to gold. Dithiobis(sulfosuccinimidyl propionate), DTSSP, and dithiothreitol, DTT, react with the amines on the core protein of aggrecan to form a thiol. The thiol then reacts with the gold substrate to form a thiol-gold bond.

cut from the whole wafer. The gold coated substrates were cleaned with *piranha* (3:1 H_2SO_4 (100%) and H_2O_2 (30%) *Caution! piranha reacts violently with organics.*) and thouroughly rinsed with deionized water, and then ethanol just prior to use. $50\mu l$ of $1mg/ml$ thiol-modified aggrecan solution was incubated on the freshly cleaned substrate for 48 hours. The substrates were then rinsed with water before use.

G.2 Characterization of the surface

The success of the surface functionalization reaction was verified by contact angle measurements (Figure G-2) and by dimethylmethylene blue dye (DMMB) assay[32] (Figure G-3). The advancing angle for the aggrecan modified substrate ($5 \pm 2°$) was significantly smaller than that of a bare gold substrate ($90 \pm 9°$). DMMB dye is used to measure sulfated glycosaminoglycans. To measure the amount of aggrecan on the surfaces, the aggrecan must first be removed and the thiol-gold bond needs to be broken. The substrates were put in $3ml$ of deionized water and then they were boiled until there was only $\sim 1ml$ of water left which was frozen, lyophilized, then reconstituted with $50\mu l$ of deionized water. $20\mu l$ of the sample was added to $180\mu l$ of

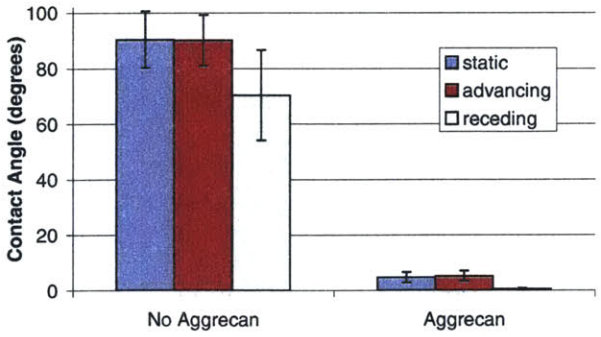

Figure G-2: Contact angle measurements on a bare gold substrate and an aggrecan modified substrate.

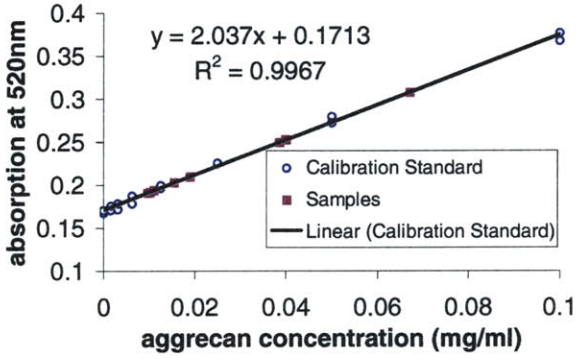

Figure G-3: Dimethylmethylene blue dye (DMMB) assay results showing the absorption at $\lambda = 520nm$ of the calibration standard, corresponding best-fit line, and the sample removed from various modifed substrates.

dye. A standard series of aggrecan solutions of known concetration was also done as a calibration (see Figure G-3). All the samples from the modified substrates were found to have on $\sim 0.5 - 3\mu g$ of aggrecan while the controls of bare gold samples boiled in the same way had less than $<< 0.03\mu g$ (the smallest point on the calibration series). The average aggrecan density was found to be $\sim 2590 \pm 90$ aggrecan molecules per $1\mu m \times 1\mu m$ or 1 aggrecan per $\sim 19nm \times 19nm$.

Finally, to further confirm the presence of aggrecan on the surface, the thickness of the aggrecan layer was measured to be $7 \pm 1nm$ in ambient conditions using ellipsometry (VASE VB-250 J.A. Woollam Co., Inc., USA). Measurements were also done with the substrates in a custom fluid chamber filled with 0.001M-1M NaCl solutions (Figure G-4). The change in polarization state of light reflected from the surface of

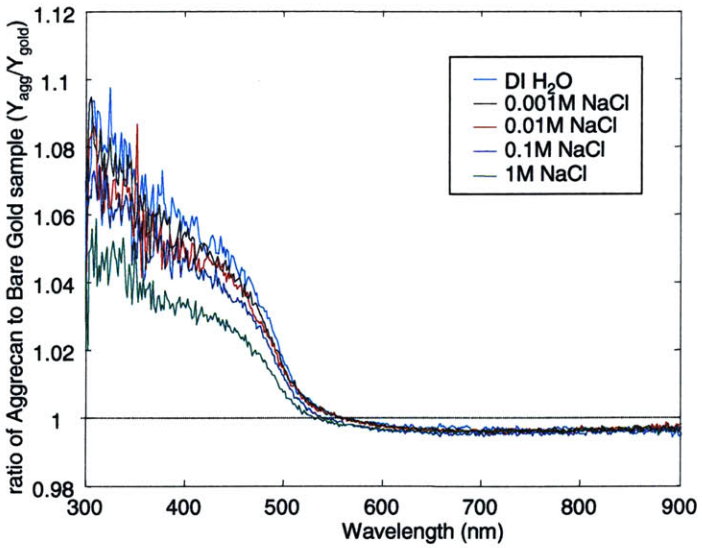

Figure G-4: Ratio of the the ellipsometric angle Ψ measured on a aggrecan surface to that measured on a bare gold substrate in different ionic strength solutions (0.001M-1M NaCl). The dotted line represents a value of 1.

the sample was measured via the ellipsometric angles Ψ and Δ versus wavelength $(240 - 1000nm)$ at a fixed angle of incidence (70°) between the incoming beam and the sample normal. As shown in Figure G-4, there were distinct differences between the sample with the aggrecan coated sample and the bare gold control and these differences decrease with increasing ionic strength. However, the ellipsometric data needs to be fit to theoretical models in order to obtain a thickness measurement. For the measurement in ambient conditions (dry), a simple model with 2 layers can be used (using the pre-packaged software). The first layer is the default gold model, and using a Cauchy model with 2 fitting parameters (the thickness, A_n, and $B_n = 0$). Fitting the measurements in fluid, however, is significantly more difficult and requires too many unknown parameters to be fit.

The contour length of the fetal bovine epiphyseal aggrecan is $\sim 400nm$ and the maximum height that was measured by AFM (Chapter 4) is very near the full length of the molecule. This gives some indication that the aggrecan is attached near one of its ends on the gold. Another indication comes from looking at the amino acid sequence of the core protein (Figure G-5). DTSSP will react with the amine group at the N-terminal of the protein as well as the ϵ-amine group on the side chain of lysine.

As shown in Figure G-5, lysines are predominantly found on either ends of the core protein with only 4 found inside the chondroitin sulfate (CS) domains. Therefore, it is very likely that the aggrecan core protein is attached to the substrate by one of its ends. However, we can not be sure if it is attached by the N-terminal or C-terminal side since there are lysines at either end.

MTTLLWVFVTLRVITAAVTVETSDHDNSLSVSIPQPSPLRVLLGTSLTIPCYFIDPMHPVTTAPSTAPLAP
RIKWSRVSKEKEVVLLVATEGRVRVNSAYQDKVSLPNYPAIPSDATLEVQSLRSNDSGVYRCEVMHGIEDS
EATLEVVVKGIVFHYRAISTRYTLDFDRAQRACLQNSAIIATPEQLQAAYEDGFHQCDAGWLADQTVRYPI
HTPREGCYGDKDEFPGVRTYGIRDTNETYDVYCFAEEMEGEVFYATSPEKFTFQEAANECRRLGARLATTG
HVYLAWQAGMDMCSAGWLADRSVRYPISKARPNCGGNLLGVRTVYVHANQTGYPDPSSRYDAICYTGEDFV
DIPENFFGVGGEEDITVQTVTWPDMELPLPRNITEGEARGSVILTVKPIFEVSPSPLEPEEPFTFAPEIGA
TAFAEVENETGEATRPWGFPTPGLGPATAFTSEDLVVQVTAVPGQPHLPGGVVFHYRPGPTRYSLTFEEAQ
QACPGTGAVIASPEQLQAAYEAGYEQCDAGWLRDQTVRYPIVSPRTPCVGDKDSSPGVRTYGVRPSTETYD
VYCFVDRLEGEVFFATRLEQFTFQEALEFCESHNATATTGQLYAAWSRGLDKCYAGWLADGSLRYPIVTPR
PACGGDKPGVRTVYLYPNQTGLPDPLSRHHAFCFRGISAVPSPGEEEGGTPTSPSGVEEWIVTQVVPGVAA
VPVEEETTAVPSGETTAILEFTTEPENQTEWEPAYTPVGTSPLPGILPTWPPTGAETEESTEGPSATEVPS
ASEEPSPSEVPFPSEEPSPSEEPFPSVRPFPSVELFPSEEPFPSKEPSPSEEPSASEEPYTPSPPEPSWTE
LPSSGEESGAPDVSGDFTGSGDVSGHLD

CS DOMAINS:

FSGQLSGDRASGLPSGDLDSSGLTSTVGSGLTVESGLPSGDEERIEWPSTPTVGELPSGAEILEGSASGVG
DLSGLPSGEVLETSASGVGDLSGLPSGEVLETTAPGVEDISGLPSGEVLETTAPGVEDISGLPSGEVLETT
APGVEDISGLPSGEVLETTAPGVEDISGLPSGEVLETTAPGVEDISGLPSGEVLETAAPGVEDISGLPSGE
VLETAAPGVEDISGLPSGEVLETAAPGVEDISGLPSGEVLETAAPGVEDISGLPSGEVLETAAPGVEDISG
LPSGEVLETAAPGVEDISGLPSGEVLETAAPGVEDISGLPSGEVLETAAPGVEDISGLPSGEVLETAAPGV
EDISGLPSGEVLETAAPGVEDISGLPSGEVLETAAPGVEDISGLPSGEVLETTAPGVEEISGLPSGEVLET
TAPGVDEISGLPSGEVLETTAPGVEEISGLPSGEVLETSTSAVGDLSGLPSGGEVLEISVSGVEDISGLPS
GEVVETSASGIEDVSELPSGEGLETSASGVEDLSRLPSGEEVLEISASGFGDLSGVPSGGEGLETSASEVG
TDLSGLPSGREGLETSASGAEDLSGLPSGKEDLVGSASGDLDLGKLPSGTLGSGQAPETSGLPSGFSGEYS
GVDLGSGPPSGLPDFSGLPSGFPTVSLVDSTLVEVVTASTASELEGRGTIGISGAGEISGLPSSELDISGR
ASGLPSGTELSGQASGSPDVSGEIPGLFGVSGQPSGFPDTSGETSGVTELSGLSSGQPGVSGEASGVLYGT
SQPFGITDLSGETSGVPDLSGQPSGLPGFSGATSGVPDLVSGTTSGSGESSGITFVDTSLVEVAPTTFKEE
EGLGSVELSGLPSGEADLSGKSGMVDVSGQFSGTVDSSGFTSQTPEFSGLPSGIAEVSGESSRAEIGSSLP
SGAYYGSGTPSSFPTVSLVDRTLVESVTQAPTAQEAGEGPSGILELSGAHSGAPDMSGEHSGFLDLSGLQS
GLIEPS

GEPPGTPYFSGDFASTTNVSGESSVAMGTSGEASGLPEVTLITSEFVEGVTEPTISQELGQRPPVTHTPQL
FESSGKVSTAGDISGATPVLPGSGVEVSSVPESSSETSAYPEAGFGASAAPEASREDSGSPDLSETTSAFH
EANLERSSGLGVSGSTLTFQEGEASAAPEVSGESTTTSDVGTEAPGLPSATPTASGDRTEISGDLSGHTSQ
LGVVISTSIPESEWTQQTQRPAETHLEIESSSLLYSGEETHTVETATSPTDASIPASPEWKRESESTAADQ
EVCEEGWNKYQGHCYRHFPDRETWVDAERRCREQQSHLSSIVTPEEQEFVNNNAQDYQWIGLNDRTIEGDF
RWSDGHPMQFENWRPNQPDNFFAAGEDCVVMIWHEKGEWNDVPCNYHLPFTCKKGTATTYKRRLQKRSSR
HPRRSRPSTAH

K = lysine
H = histidine
R = arginine

Figure G-5: Amino acid sequence of the core protein of aggrecan. The basic amino acids (lysines (K), histidines (H), and arginine (R)) are highlighted. DTSSP should react with the amine at the N-terminal of the protein as well as the ϵ-amine group on the side chain of lysine.

Appendix H

Nanomechanical properties of aggrecan monolayers

In this appendix, interaction forces were measured between a negatively charged probe tip and a dense monolayers of aggrecan adsorbed onto a mica substrate and aggrecan chemically bound to amine terminated self-assembled monolayers on a gold substrate. As opposed to the end-grafted setup in Chapter 4, the aggrecan here is attached to the substrate by its chondroitin sulfate glycosaminoglycan (CS-GAG) side chains.

H.1 Methods

H.1.1 Aggrecan on Mica

$50\mu l$ of $500\mu g/ml$ DI water solution of A1A1D1D1 aggrecan from fetal bovine epiphyseal growth plate was allowed to incubate on positively-charged mica that had been functionalized with A3-amino-propyltriethoxysilane (AP-mica)[68] for 30-40 min, then rinsed, and dried in air for at least 10 hrs. COO^--modified probe tips of known negative surface charge density ($-0.018C/nm^2$) were made by modifying Au-coated Thermomicroscopes V-shaped Si_3N_4 cantilevers (probe tip radius, $R_{tip} \sim 50nm$, spring constant $\sim 0.01N/m$) incubated in 2 mM solution of 11-mercaptoundecanoic acid ($HS(CH_2)_10COOH$ (Aldrich #45,056-1) in ethanol for 48 hrs, followed immediately

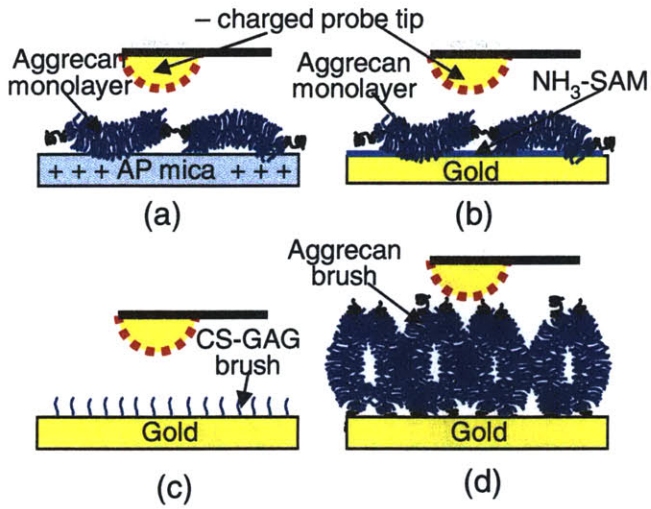

Figure H-1: Experimental setup for 3 configurations discussed in this appendix: (a) aggrecan monolayer on AP mica, (b) aggrecan monolayer covalently attached to gold, and (c) previous CS-GAG experiment setup.

by rinsing with DI water before experimentation[83].

H.1.2 Aggrecan on Amine Terminated Self-Assembled Monolayers (NH_3-SAM)

H.1.3 Force measurements

The forces between the negatively charged tip and the aggrecan monolayer were measured at 3-5 different locations along the monolayer in 0.0001-0.1M NaCl solutions using a 3-D Molecular Force Probe (3-D MFP) (Asylum Research) (Figure 1a). To confirm the presence of a dense aggrecan monolayer on mica, the substrate was first imaged in air using tapping mode with Olympus Si cantilevers ($R_{tip} < 10nm$, spring constant $\sim 2N/m$) and in fluid using contact mode with the modified probe tip (Figure H-2. Forces between a COO^--modified probe tip ($R_{tip} \sim 120nm$) and a CS-GAG brush layer were measured in 0.001-1.0 M NaCl solutions using a 1-DMFP (Asylum Research). The CS-GAG was obtained from rat chondrosarcoma cell cultures and end-grafted onto $1cm \times 1cm$ Au-coated silicon substrates using methods previously described.[89] The CS-GAG density was measured by DMMB assay and was found

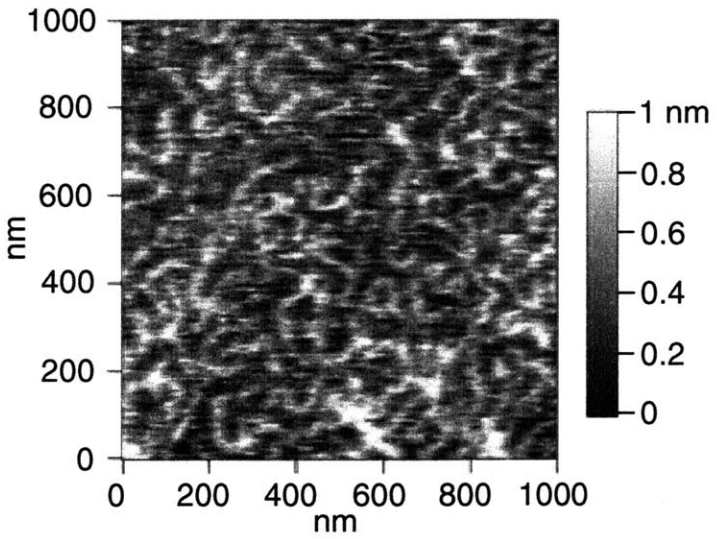

Figure H-2: Height image of aggrecan monolayer adsorbed onto AP-mica in air taken with an MFP-3D

to be $\sim$ 1 chain per $9nm^2$.

H.2 Results and Discussion

H.2.1 Aggrecan monolayer on Mica

Repulsive forces between the COO^--modified tip and the aggrecan monolayer on mica were observed on approach at all ionic strengths (Figure H-4). The repulsive forces at 0.1 and 0.01M NaCl were longer ranged than the forces at the 0.001M NaCl; the force at 0.01M NaCl started at about the same separation distance ($\sim$ $100nm$) as the force in 0.0001M NaCl. The retraction force was purely repulsive at lower ionic strength; however, attractive forces were observed on retract in some of the curves at the higher ionic strengths. The frequency of attractive retraction forces increased with increasing ionic strength. In contrast, the forces on the CS-GAG brush were purely repulsive on approach and retract, and the magnitude of the force decreased with increasing ionic strength as previously reported.[89] Most importantly, as shown in Figure 3, the force due to the aggrecan monolayer was longer range than the force due to the GAG brush alone.

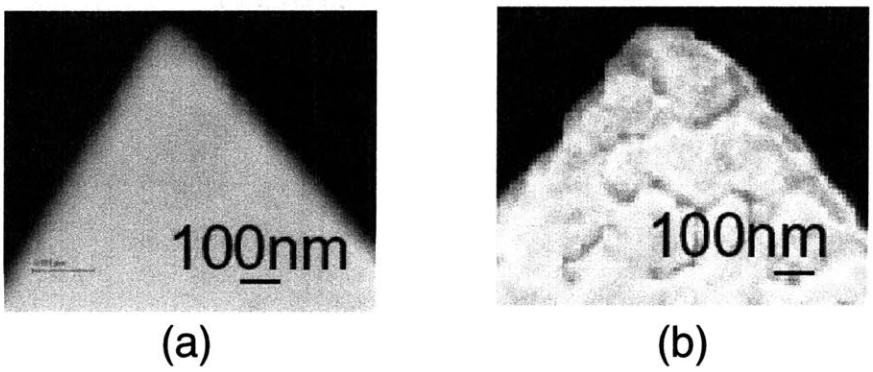

Figure H-3: SEM image of tip used with (a) the aggrecan experiments ($R_{tip} \sim 50nm$) and (b) the GAG brush experiments ($R_{tip} \sim 120nm$).

The force profiles for the lower IS (0.0001M and 0.001M NaCl in Figure H-4) agree well with the predictions of an electrostatic repulsion model that represents aggrecan-GAG charge as a uniform surface charge.[24] This is consistent with the fact that the underlying AP-mica is positive and, therefore, the GAG chains most likely collapse onto the surface due to the strong electrostatic attractive force at lower ionic strengths. Since the GAGs lie on the substrate, they effectively form a very highly negatively charged surface. The collapsed GAG chains also effectively shield the tip from the positive AP-mica and the protein core, so the frequency of attractive forces on retraction is low. However, as the IS is increased (0.01M and 0.1M NaCl, Figure H-4), the length scale of interaction forces is only 1-3nm and only the GAG chains very near the surface would be attracted, leaving many GAGs oriented vertically into the NaCl solution.

This hypothesis is consistent with the observed increase in the range of the measured repulsive force beyond what would be predicted from a surface charge model, since the GAG chains on the aggrecan are in a more physiological brush-like configuration away from the surface.[24] The repulsion forces produced by the aggrecan monolayer also appear to act over a longer range than those produced by the GAG brush (Figure H-5). From the images of the aggrecan monolayer in air, the aggrecan density on the mica surface was found to be reasonably uniform over large areas (measured to be $\sim$ 1 aggrecan monomer per $400nm^2$). Since there are about 80-100

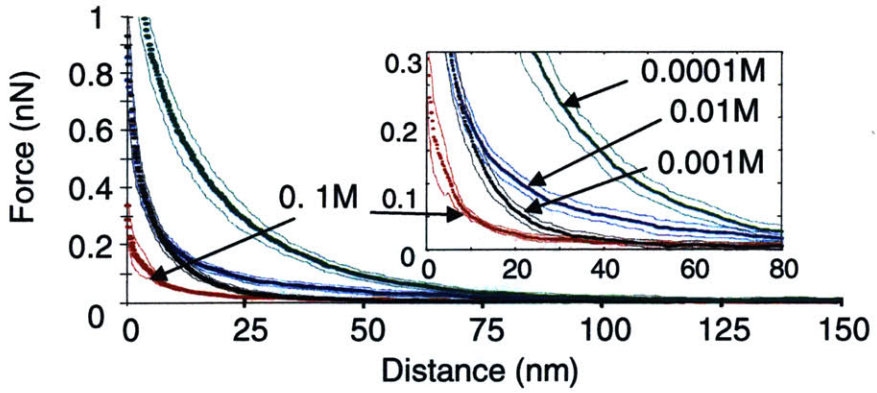

Figure H-4: Results aggrecan monolayer on mica versus a negatively charged tip as a function of ionic strength ([NaCl] = 0.1-0.0001M)

GAG chains per aggrecan monomer, this translates to almost 1 GAG chain per $4nm^2$ which is much higher than the density of GAG in the CS-GAG brush experiment of Figure H-1b. This is also consistent with the observation that once the tip is within the aggrecan GAG-brush, the force due to aggrecan is bigger than the force due to the isolated CS-GAG brush. The contour length of the GAG chains on fetal bovine epiphyseal aggrecan is $\sim 50nm$ while the contour length of the GAG chains from the rat chondrosarcoma cells is $\sim 40nm$. The forces on aggrecan would be expected to start only $\sim 10nm$ further out than the forces on the GAG brush; however, the repulsive force due to the aggrecan monolayer starts at a distance almost $50nm$ further. Taken together, these findings suggest that the density of GAG on fetal aggrecan produces high repulsive forces that extend far from the macromolecule compared to forces attributable to less dense GAG brushes having GAG densities more similar to those of mature aggrecan.[68, 24]

H.2.2 Aggrecan covalently attached to amine SAM

Aggrecan was covalently attached an amine terminated self-assembled monolayer on gold such that the geometry would the same as the aggrecan on mica (Figure H-6. In this way, aggrecan did not detach at the higher ionic strength and the aggrecan density was maintained the same as the ionic strength of the bath was increased. The

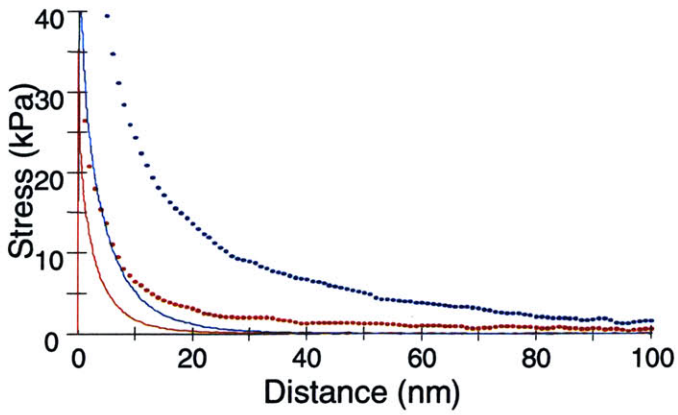

Figure H-5: Aggrecan monolayer (dashed lines) results compared to results on GAG brushes (solid lines) at 0.1M (red) and 0.01M (blue) NaCl.

results were similar to the forces between a negative tip and an aggrecan monolayer on mica (Figure H-7).

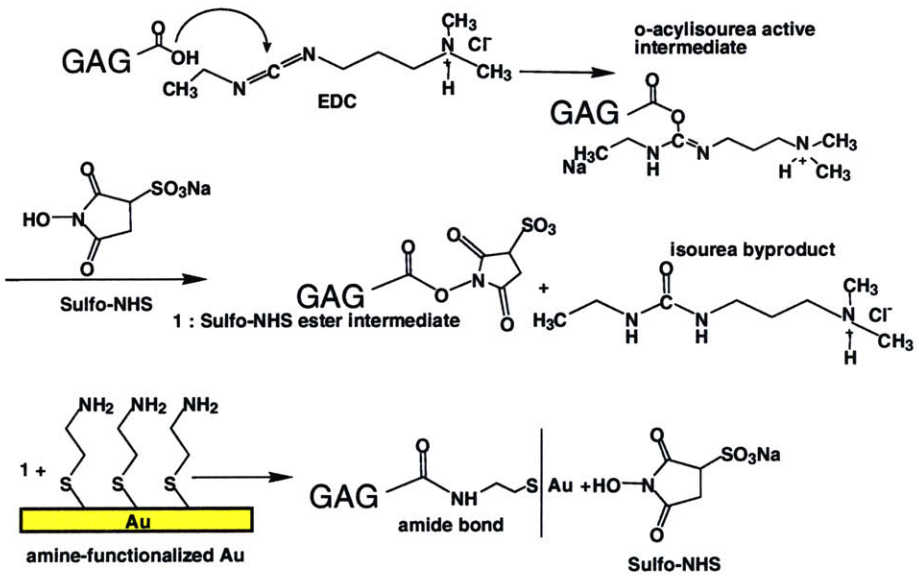

Figure H-6: Schematic of the covalent attachment of aggrecan to an amine terminated SAM.

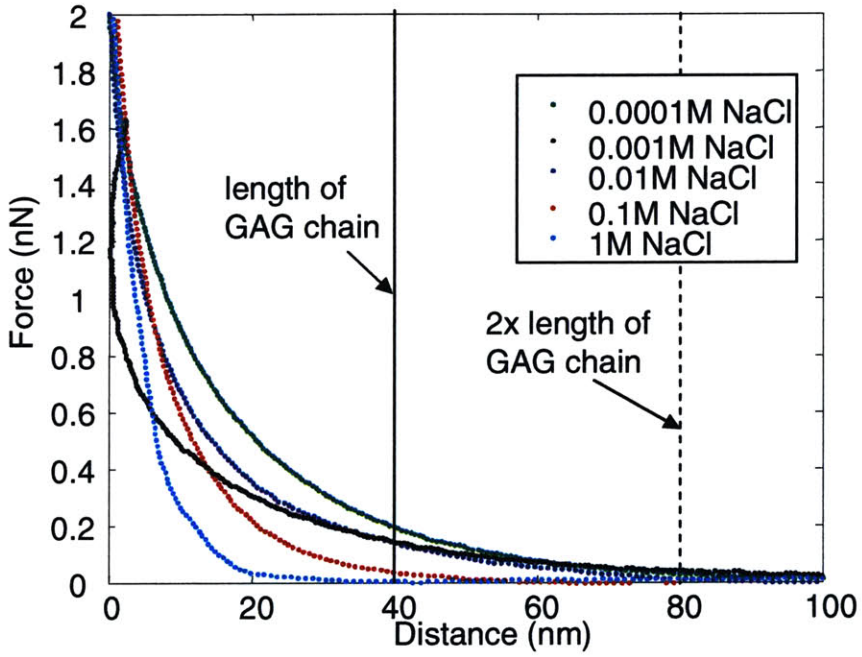

Figure H-7: Force between a negatively charged probe tip and an aggrecan monolayer covalently attached to an amine SAM as a function of ionic strength.

Appendix I

Retraction forces between aggrecan brush layers

The force curves obtain from chondroitin sulfate glycosaminoglycan (GAG) only brushes were always purely reversible and repulsive. This means that both while the tip coated with GAG approached and retracted from the GAG brush on the surface, the tip was repelled indicating that the repulsive forces between the GAGs were always large enough to counteract any attractive interaction. However, the forces between aggrecan brushes were not reversible and attractive pulling forces were seen on retraction even though the forces on approach were always repulsive (see Figure I.0.3).

I.0.3 Results

The approach curves had very little variation (standard deviation $\sim .003nN$) while the attractive forces showed large changes with each repeat even when all other parameters (e.g. tip velocity or dwell time on the surface) are kept constant (see Figures I.0.3). The peak magnitude and length of these retraction forces increased with ionic strenght and surface dwell time (Figure I-2). Dwell time is the time which the tip is forces to stay in contact with the surface (keeping the force constant). In our experiments, the dwell time was varied between 0, 1, 5 and 10 seconds with the tip

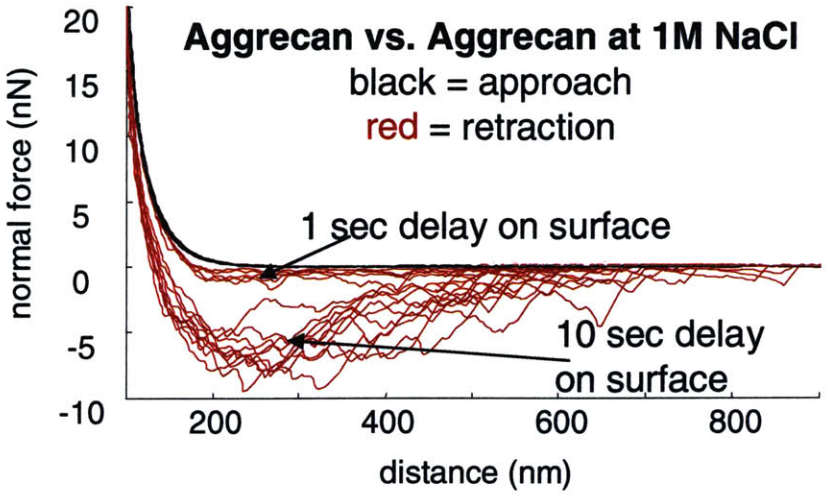

Figure I-1: Approach (black) and retraction (red) curves between an aggrecan coated colloidal tip and aggrecan coated substrate at 1M NaCl with 1sec and 10sec dwell time on the surface.

held to maintain $40nN$ force. The maximum distance of interaction was $\sim 900nm$ at 1M NaCl with 10sec dwell which is slightly larger than than $2\times$ the average contour length of aggrecan ($\sim 800nm$). In order to more clearly see the difference with ionic strength and dwell time, the average peak attractive force was calculated (Figure I-3) and shows the significant differences as ionic strength and dwell time is increased.

I.0.4 Discussion

Considering the range and the jagged shape of the attactive force on retract, thes are probably due to entanglement of the aggrecan molecules from the tip with those on the substrate. At high ionic strength (1M NaCl) when the Debye length (Equation 3.10 and Table 3.2) is smaller the than the spacing between the GAG chains, these are able to get near each other and entangle. At low ionic strength though, the GAG chains still repell each other and no pulling force is observed. This attractive force between aggrecan brushes at high ionic strength as already been indirectly observed. The lateral forces between aggrecan brushes were observed to increase with increasing ionic strength. In particular, the force at 1M NaCl was much larger and had higher noise that the low ionic strengths.[44]

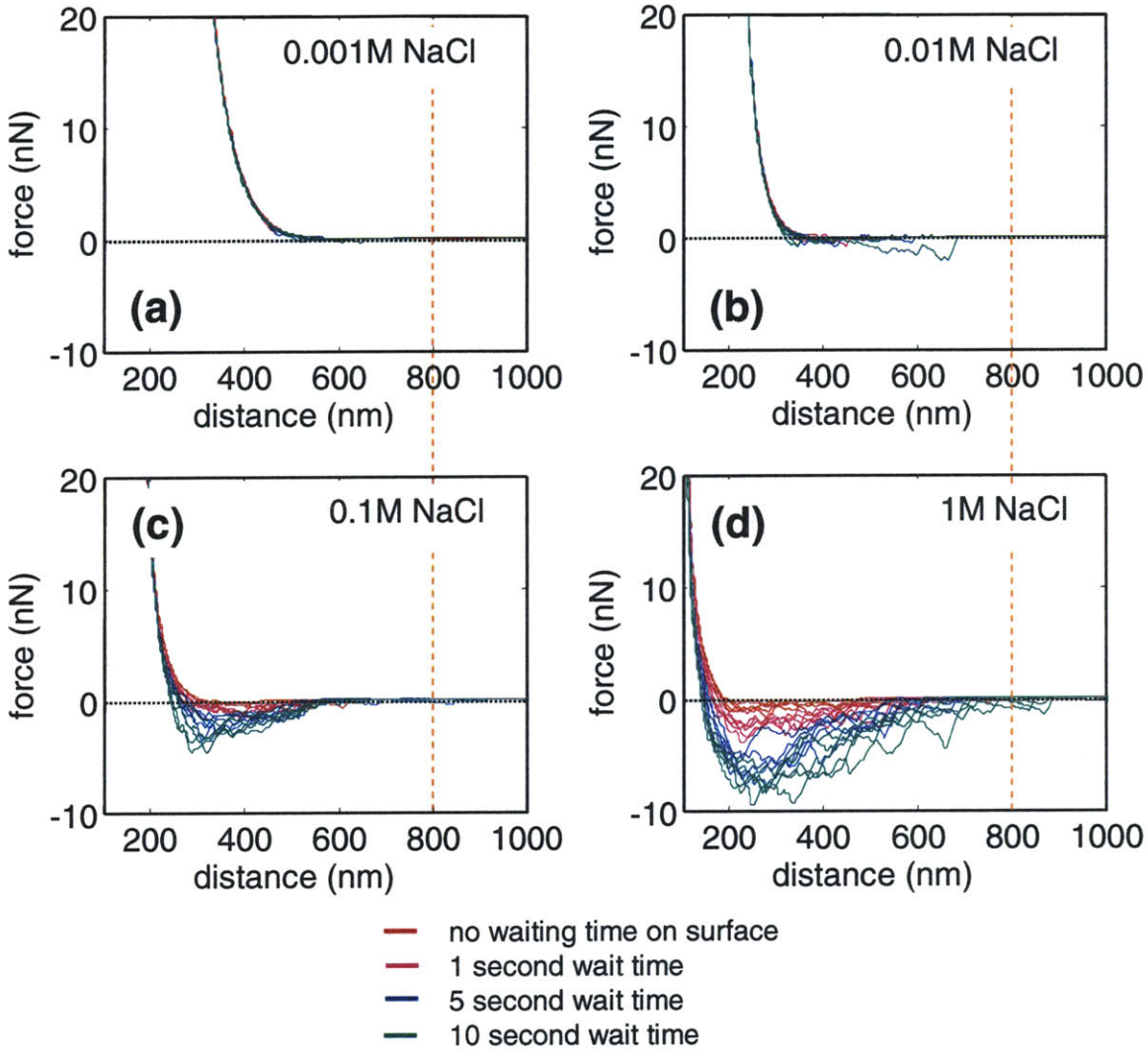

Figure I-2: Retraction forces between aggrecan brush layers at different ionic strengths and using different surface dwell times. The black line indicates 0nN force and the orange dashed line represents 2× the aggrecan contour length.

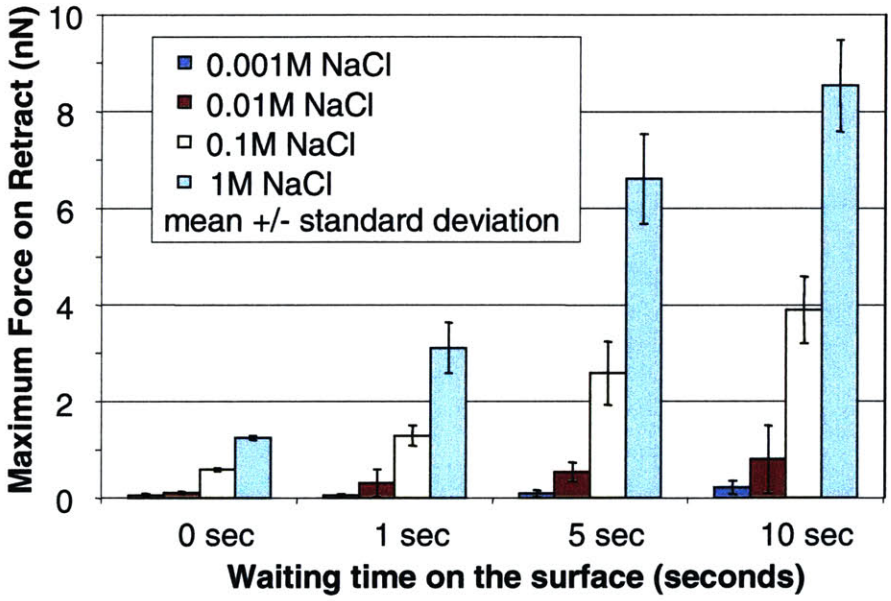

Figure I-3: Summary of the aggrecan maximum retraction force magnitudes at different ionic strengths and different surface dwell times.

Bibliography

[1] T. Abe, N. Higashi, M. Niwa, and K. Kurihara. Density-dependent jump in compressibility of polyelectrolyte brush layers revealed by surface forces measurement. *Langmuir*, 15(22):7725–7731, 1999.

[2] T. Abraham, S. Giasson, J. F. Gohy, and R. Jerome. Direct measurements of interactions between hydrophobically anchored strongly charged polyelectrolyte brushes. *Langmuir*, 16(9):4286–4292, 2000.

[3] B. Alberts, D. Bray, J. Lewis, M. Raff, K. Roberts, and J. D. Watson. *Molecular Biology of the Cell.* Garland, New York, 1994.

[4] M. Bathe, G.C. Rutledge, A.J. Grodzinsky, and B. Tidor. Towards a multi-scale model of cartilage: Coarse-graining glycosaminoglycans. In K.J. Bathe, editor, *Computational Fluid and Solid Mechanics.* Elsevier Science Ltd., Cambridge, MA, 2003.

[5] S. Bhattacharjee and . M. Elimelech. Surface element integration : A novel technique for evaluation of dlvo intreraction between a particle and flat plate. *Journal Colloid Interface Science*, 193:273–285, 1997.

[6] M. Biesalski and J. Rhe. Preparation and characterization of a polyelectrolyte monolayer covalently attached to a planar solid surface. *Macromolecules*, 32(7):2309–2316, 1999.

[7] H. G. Braun and E. Meyer. Microprinting - a new approach to study competitive structure formation on surfaces. *Macromolecular Rapid Communications*, 20(6):325–327, 1999.

[8] T. D. Brown and R. J. Singerman. Experimental determination of the linear biphasic constitutive coefficients of human fetal proximal femoral chondroepiphysis. *Journal of Biomechanics*, 19:597–605, 1986.

[9] J. Buckwalter, L. Rosenberg, and L-H Tang. The effect of link protein on proteoglycan aggregate structure. *J. Biol. Chem.*, 259(9):5361–5363, 1984.

[10] J. A. Buckwalter and L. C. Rosenberg. Electron microscopic studies of cartilage proteoglycans. *Electron Microscopy Review*, 1:87–112, 1988.

[11] M. D. Buschmann and A. J. Grodzinsky. A molecular model of proteoglycan-associated electrostatic forces in cartilage mechanics. *Journal Biomechanical Engineering*, 117(2):179–92, 1995.

[12] H.-J. Butt. Electrostatic interaction in atomic force microscopy. *Biophys. J.*, 60:777–785, 1991.

[13] H.-J. Butt. Measuring local surface charge densities in electrolyte solutions with a scanning force microscope. *Biophys. J.*, 63:578–582, 1992.

[14] H.-J. Butt and M. Jaschke. Calculation of thermal noise in atomic force microscopy. *Nanotechnology*, 6:1–7, 1995.

[15] A. Calabro, R.J. Midura, A. Wang, L.A. West, A. H. K. Plaas, and V. C. Hascall. Fluorophore-assisted carbohydrate electrophoresis (face) of glycosaminoglycans. *Osteoart. and Cart.*, 9(SA):S16–S22, 2001.

[16] D.L. Chapman. A contribution to the theory of electrocapillarity. *Philosophical Magazine*, 25(6):475–481, 1913.

[17] J. Clevelan. The asylum mfp design is such that certain types of highly conducting tips can be grounded via the spring clip that holds the cantilever chip; however this was not the case for our system., 2002. Asylum Research, Personal communication.

[18] W. D. Comper and T. C. Laurent. Physiological function of connective tissue polysaccharides. *Physiol. Rev.*, 58:255–315, 1978.

[19] F. S. Csajka and C. Seidel. Strongly charged polyelectrolyte brushes: A molecular dynamics study. *Macromolecules*, 33(7):2728–2739, 2000.

[20] C. G. de Kruif and E. B. Zhulina. kappa-casein as a polyelectrolyte brush on the surface of casein micelles. *Coll. Surf. A*, 117:151, 1996.

[21] D. Dean. Molecular electromechanics: Modeling electrostatic forces between glycosaminoglycan molecules. Master of engineering thesis, Massachusetts Institute of Technology, Electrical Engineering and Computer Science Department, May 2001.

[22] D. Dean, L. Han, C. Ortiz, and A. J. Grodzinsky. Nano-scale conformation and compressibility of cartilage aggrecan using micro contact printing and atomic force microscopy. submitted for publication as a Communication in Macromolecules., 2004.

[23] D. Dean, L. Ng, J. Seog, C. Ortiz, and A. J. Grodzinsky. Measurement of nanomechanical and electrical interaction forces within intact aggrecan molecules using high resolution force spectroscopy. In *50th Annual Meeting of the Orthopaedic Research Society*, San Francisco, CA, Mar. 2004.

[24] D. Dean, J. Seog, C. Ortiz, and A. J. Grodzinsky. A new molecular-level theoretical model for the electrostatic interactions between polyelectrolyte macromolecules using glycosaminoglycans as a model system. *Langmuir*, 19(13):5526–5539, 2003.

[25] B. V. Derjaguin. Untersuchungen über die reibung und adhäsion. *Kolloid Zeitschrift*, 69:155–164, 1934.

[26] Owen Francis Devereux and P. L. de Bruyn. *Interaction of plane-parallel double layers.* M.I.T. Press, Cambridge, MA, 1963.

[27] Digital Intruments Veeco Metrology Group, Santa Barbara, CA. *MultiMode^{TM} SPM Instruction Manual*, 1997.

[28] F. G. Donnan. Theorie der membrangleichgewichte und membranpotentiali. *Z. Electrochemie*, 17:572, 1911.

[29] J. Dudhia, C.M. Davidson, T.M. Wells, D.H. Vynios, T.E. Hardingham, and M.T. Bayliss. Age-related changes inthe content of the c-terminal region of aggrecan in human articular cartilage. *Biochem. J.*, 313:933–940, 1996.

[30] S. Ehrlich, N. Wolff, R. Schneiderman, A. Maroudas, K. H. Parker, and C. P. Winlove. The osmotic pressure of chondroitin sulphate solutions: experimental measurements and theoretical analysis. *Biorheology*, 35(6):383–97, 1998.

[31] S. R. Eisenberg and A. J. Grodzinsky. Swelling of articular cartilage and other connective tissues: electromechanochemical forces. *J Orthop Res*, 3(2):148–59, 1985.

[32] R. W. Farndale, D. J. Buttle, and A. J. Barrett. Improved quantitation and discrimination of sulphated glycosaminoglycans by use of dimethylmethylene blue. *Biochim Biophys Acta*, 883(2):173–7, 1986.

[33] M. Fixman. Poisson-boltzmann equation and its application to polyelectrolytes. *Journal of Chemical Physics*, 70(11):4995–5005, 1979.

[34] C. R. Flannery, M. W. Lark, and J. D. Sandy. Identification of a stromelysin cleavage site within the interglobular domain of human aggrecan. evidence for proteolysis at this site in vivo in human articular cartilage. *J Biol Chem*, 267(2):1008–14, 1992.

[35] E. L. Florin, V. T. Moy, and H. E. Gaub. Adhesion forces between individual ligand-receptor pairs. *Science*, 264(5157):415–7, 1994.

[36] G. E. Forsythe and W. R. Wasow. *Finite Difference Methods for Partial Differential Equations.* John Wiley +Sons, inc., New York, 1960.

[37] D. Fotiadis, S. Scheuring, S.A. Muller, A. Engel, and D.J. Muller. Imaging and manipulation of biological structures with the afm. *Micron*, 33:385–397, 2002.

[38] A. Franzén, S. Inerot, S.-O. Hejderup, and D. Heinegå rd. Variations in the composition of bovine hip articular cartilage with distance from the articular surface. *Biochemistry Journal*, 195:535–543, 1981.

[39] W. D. S. C. Freeman and A. Maroudas. Charged group behaviour in cartilage proteoglycans in relation to ph. *Annals of the Rheumatic Diseases*, 34(Suppl.):44–45, 1975.

[40] N.J. Fullwood, A. Hammiche, H.M. Pollock, D.J Hourston, and M. Song. Atomic force microscopy of the cornea and sclera. *Curr. Eye Res.*, 14:529–535, 1995.

[41] G. Gouy. Sur la constitution de la charge lectrique la surface d'un lectrolyte. *Journal De Physique*, 9:457–468, 1910.

[42] A.P. Gunning, V. J. Morris, S. Al-Assaf, and G. O. Phillips. Atomic force microscope studies of hylan and hyaluronan. *Carbohydrate Polymers*, 30:1–8, 1996.

[43] B.-Y. Ha and A. J. Liu. Counterion-mediated, non-pairwise-additive attractions in bundles of like-charged rods. *Phys Rev E*, 60(1):803–813, 1999.

[44] L. Han, D. Dean, A. J. Grodzinsky, and C. Ortiz. Lateral and compressive imaging of cartilage aggrecan via atomic force microscopy as a function of ionic strength. In *Materials Research Society Fall Meeting Symposium Y: Mechanical Properties of Bio-Inspired and Biological Materials*, Boston, MA, Dec. 2004.

[45] H. G. Hansma. Atomic force microscopy of biomolecules. *J. Vac. Sci. Tech. B*, 14:1390–1394., 1996.

[46] H. G. Hansma and K. J. Kim. Properties of biomolecules measured from atomic force microscope images: A review. *J. Struct. Biol.*, 119:99–108, 1997.

[47] T. E. Hardingham and A. J. Fosang. Proteoglycans: many forms and many functions. *FASEB J.*, 6:861–870, 1992.

[48] D. Heinegå rd and A. Oldberg. Structure and biology of cartilage and bone matrix noncollagenous macromolecules. *FASEB J.*, 3:2042–2051, 1989.

[49] F Helfferich. *Ion Exchange.* McGraw-Hill Book Company, New York, 1962.

[50] B. Honig and A. Nicholls. Classical electrostatics in biology and chemistry. *Science*, 268:1144–1149, 1995.

[51] R. G. Horn and J. N. Israelachvili. Direct measurement of forces due to solvent structure. *Chemical Physics Letters*, 71(2):192–194, 1980.

[52] J. L. Hutter and J. Bechhoefer. Calibration of atomic-force microscope tips. *Rev. Sci. Instrum.*, 64(7):1868–1873, 1993.

[53] D. J. Irvine, A. M. Mayes, S. K. Satija, J. G. Barker, S. J. Sofia-Allgor, and L. G. Griffith. Comparison of tethered star and linear poly(ethylene oxide) for control of biomaterials surface properties. *J. Biomed. Mater. Res.*, 40(3):498–509, 1998.

[54] J. N. Israelachvili. The forces between surfaces. *Philosophical Magazine a-Physics of Condensed Matter Structure Defects and Mechanical Properties*, 43(3):753–770, 1981.

[55] J. N. Israelachvili. *Intermolecular and Surface Forces.* Academic Press, London, 2nd edition, 1992.

[56] J. N. Israelachvili and G. E. Adams. Direct measurement of long-range forces between 2 mica surfaces in aqueous kno3 solutions. *Nature*, 262(5571):773–776, 1976.

[57] H. Iwamoto, D.M. Czajkowsky, and Z. Shao. Afm in biology: From subcellular to submolecular. *Journal of Electron Microscopy*, 49:395–406, 2000.

[58] A. Katchalsky. Polyelectrolytes. *Pure Appl. Chem.*, 26:327–373, 1971.

[59] I. S. Kovach. A molecular theory of cartilage viscoelasticity. *Biophysical Chemistry*, 59(1):61–73, 1996.

[60] K. Kuettner and A. Lindenbaum. Analysis of mucopolysaccharides in partially aqueous media. *Biochim. Biophys. Acta*, 101:223–225, 1965.

[61] X. Liu, P.C. Noble, and Z.P. Luo. A method for testing compressive properties of single proteoglycan aggrecates. *Biochem. Biophys. Res. Commun.*, 307(2):338–341, 2003.

[62] R. A. Marcus. Calculation of thermodynamic properties of polyelectrolytes. *Journal of Chemical Physics*, 23:1057–1068, 1955.

[63] A. Maroudas. Physicochemical properties of articular cartilage. In M. A. R. Freeman, editor, *Adult Articular Cartilage*, pages 215–290. Pitman Medical, Kent, England, 1979.

[64] A. Maroudas. *Physical Chemistry of Articular Cartilage and the Intervertebral Disk in Joints and Synovial Fluid*, volume II. Academic Press, l. sokoloff edition, 1980.

[65] I. Miller and D. Williams. Steric interaction of an incoming particle with grafted rods: Exact solutions and unusual force profiles. *Physical Review E: Statiscical, Nonlinear, and Soft Matter Physics*, 61(5):R4706–R4709., 2000.

[66] I.H.M. Muir. Biochemistry. In M. A. R. Freeman, editor, *Adult Articular Cartilage*, pages 215–290. Pitman Medical, Kent, 1979.

[67] R. Mukhopadhyay and J. H. Hoh. Afm force measurements on microtubule-associated proteins: the projection domain exerts a long-range repulsive force. *FEBS Lett*, 505(3):374–378, 2001.

[68] L. J. Ng, A. H. K. Plaas, J. D. Sandy, A. J. Grodzinsky, and C. Ortiz. Individual cartilage aggrecan macromolecules and their constituent glycosaminoglycans visualized via atomic force microscopy. *Journal Structural Biology*, 143(3):242–257, 2003.

[69] B. W. Ninham and V. A. Parsegian. Electrostatic potential between surfaces bearing ionizable groups in ionica equilibrium with physiologic saline solution. *Journal Theoretical Biology*, 31:405–428, 1971.

[70] F. Oesterhelt, M. Rief, and H. E. Gaub. Single molecule force spectroscopy by afm indicates helical structure of poly(ethylene-glycol) in water. *New J.ournalPhysics*, 1:6.1–6.11, 1999.

[71] H. Ohshima. Electrostatic repulsion between two parallel plates coverd with polymer brush layers. *Colloid and Polymer Science*, 277:535–540, 1999.

[72] V. A. Parsegian and D. Gingell. On the electrostatic interaction across a salt solution between two bodies bearing unequal charges. *Biophysical Journal*, 12:1192–1204, 1972.

[73] M. Paulsson, M. Morgelin, H. Wiedemann, N. Beardmore-Gray, D. Dunham, T. Hardingham, D. Heingard, R. Timpl, and J. Engel. Extended and globular protein domains in cartilage proteoglycans. *Biochem. J.*, 245:763–772, 1987.

[74] P. Pincus. Colloid stabilization with grafted polyelectrolytes. *Macromolecules*, 24(10):2912–2919, 1991.

[75] A. H. Plaas, L. A. West, S. Wong-Palms, and F. R. Nelson. Glycosaminoglycan sulfation in human osteoarthritis. disease-related alterations at the non-reducing termini of chondroitin and dermatan sulfate. *Journal Biological Chemistry*, 273(20):12642–9, 1998.

[76] A. H. K. Plaas, L.A. West, and R.J. Midura. Keratan sulfate disaccharide composition determined by face analysis of keratanase ii and endo-beta-galactosidase digestion products. *Glycobiology*, 11(10):779–790, 2001.

[77] A. H. K. Plaas, S. Wong-Palms, P.J. Roughley, R.J. Midura, and V. C. Hascall. Chemical and immunological assay of the nonreducing terminal residues of chondroitin sulfate from human aggrecan. *J. Biol. Chem.*, 272(33):20603–20610, 1997.

[78] C. B. Prater, P. G. Maivald, K. J. Kjoller, and M. G. Heaton. Probing nano-scale forces with the atomic force microscope. Application note, Digital Instruments Veeco Metrology Group, 1995.

[79] C. B. Prater, P. G. Maivald, K. J. Kjoller, and M. G. Heaton. Tappingmode imaging applications and technology. Application note, Veeco Instruments Inc., 2004.

[80] Y. Rabin and S. Alexander. Stretching of grafted polymer layers. *Europhysics Letters*, 13(1):49–54, 1990.

[81] S. S. Rao. Section 2.12: Newton-raphson method for simultaneous nonlinear equations. In *Applied numerical methods for engineers and scientists*, pages xx, 1060. Prentice Hall, Upper Saddle River, N.J., 2002.

[82] U. Raviv, S. Giasson, N. Kampf, J.-F. Gohy, R. Jerome, and J. Klein. Lubrication of charged polymers. *Nature*, 425(163-165), 2003.

[83] M. A. Rixman, D. Dean, C. E. Macias, and C. Ortiz. Nanoscale intermolecular interactions between human serum albumin and alkanethiol self-assembled monolayers. *Langmuir*, 19(15):6202–6218, 2003.

[84] M. A. Rixman, D. Dean, and C. Ortiz. Nanoscale intermolecular interactions between human serum albumin and low density poly(ethylene oxide). *Langmuir*, 19(22):9357–9372, 2003.

[85] R. L.-Y. Sah, Y.-J. Kim, J.-Y.H. Dong, A. J. Grodzinsky, A. H. K. Plaas, and J. D. Sandy. Biosynthetic response of cartilage explants to dynamic compression. *Journal of Orthopaedic Research*, 7:619–636, 1989.

[86] J. D. Sandy and C. Verscharen. Analysis of aggrecan in human knee cartilage and synovial fluid indicates that aggrecanase (adamts) activity is responsible for the catabolic turnover and loss of whole aggrecan whereas other protease activity is required for c-terminal processing in vivo. *Biochem J*, 358(Pt 3):615–26, 2001.

[87] A. Sanfeld. *Thermodynamics of charged and polarized layers*, volume 10 of *Monographs in statistical physics and thermodynamics*. Wiley-interscience publication, Bath(UK), 1968.

[88] J. Seog, D. Dean, E. Frank, C. Ortiz, and A. J. Grodzinsky. Preparation of end-grafted polyelectrolytes on nanoscale probe tips using an electric field. *Macromolecules*, 37(3):1156–1158, 2004.

[89] J. Seog, D. Dean, A. H. K. Plaas, S. Wong-Palms, A. J. Grodzinsky, and C. Ortiz. Direct measurement of glycosaminoglycan intermolecular interactions via high-resolution force spectroscopy. *Macromolecules*, 35(14):5601–5615, 2002.

[90] J. Seog, D. Dean, B. Rolauffs, T. Wu, J. Genzer, A. H. K. Plaas, A. Grodzinsky, and C. Ortiz. Nanomechanics of opposing glycosaminoglycan macromolecules. *Journal of Biomechanics*, 2004.

[91] K. A. Sharp and B. Honig. Calculating total electrostatic energies with the nonlinear poisson-boltzmann equation. *Journal of Physical Chemistry*, 94(19):7684–7692, 1990.

[92] A. I. Shestakov, J. L. Milovich, and A. Noy. Solution of the nonlinear poisson-boltzmann equation using pseudo-transient continuation and the finite element method. *Journal of Colloid and Interface Science*, 247(1):62–79, 2002.

[93] M. Stolz, R. Raiteri, A. U. Daniels, M. R. VanLandingham, W. Baschong, and U. Aebi. Dynamic elastic modulus of porcine articular cartilage determined at two different levels of tissue organization by indentation-type atomic force microscopy. *Biophysical Journal*, 86(5):3269–3283, 2004.

[94] Y.L. Sun, Z.P. Luo, A. Fertala, and K.N. An. Direct quantification of the flexibility of type i collagen monomer. *Biochem. Biophys. Res. Commun.*, 295(2):382–6, 2002.

[95] M. B. E. Sweet, E. J-M. A. Thonar, and J. Marsh. Age-related changes in proteoglycan structure. *Archives of Biochemistry and Biophysics*, 198(2):439–448, 1979.

[96] M. N. Tamashiro, E. Hernández-Zapata, P. A. Schorr, M. Balastre, M. Tirrell, and P. Pincus. Salt dependence of compression normal forces of quenched polyelectrolyte brushes. *Journal Chemical Physic*, 115(4):1960–1969, 2001.

[97] Charles Tanford. *Physical chemistry of macromolecules.* John Wiley & Sons, New York, NY, 1961.

[98] Y. Tran, P. Auroy, and L-T. Lee. Determination of the structure of polyelectrolyte brushes. *Macromolecules*, 32(26):8952–8964, 1999.

[99] S. Treppo, H. Koepp, E.C. Quan, A.A. Cole, K.E. Kuettner, and A.J. Grodzinsky. Comparison of biomechanical and biochemical properties of cartilage from human knee and ankle. *J. Orthop. Res.*, 18:739–748, 2000.

[100] J. P. G. Urban, A. Maroudas, M. T. Bayliss, and Dillon. J. Swelling pressures of proteoglycans at the concentrations found in cartilaginous tissues. *Biorheology*, 16:447–464, 1979.

[101] E. J. W. Verwey and J. Th. G. Overbeek. *Theory of the Stability of Lyophobic Colloids.* Elsevier, Amsterdam, 1948.

[102] F. von Goeler and M. Muthukumar. Stretch-collapse transition of polyelectrolyte brushes in a poor solvent. *Journal of Chemical Physics*, 105(24):11335–11346, 1996.

[103] J. L. Wilbur, A. Kumar, E. Kim, and G. M. Whitesides. Microfabrication by microcontact printint of self-assembled monolayers. *Adv. Mater.*, 6(7-8):600–604, 1994.

[104] A. Williamson, A. Chen, and R. Sah. Compressive properties and function-composition relationships of developing bovine articular cartilage. *J. Orthop. Res*, 19:1113–1121., 2001.

[105] S. Yamamoto, M. Ejaz, Y. Tsujii, M. Matsumoto, and T. Fukuda. Surface interaction forces of well-defined, high-density polymer brushes studied by atomic force microscopy. 1. effect of chain length. *Macromolecules*, 33(15):5602–5607, 2000.

[106] S. Zauscher and D. J. Klingenberg. Normal forces between cellulose surfaces measured with colloidal probe microscopy. *Journal of Colloid Interface Science*, 229(2):497–510, 2000.